2019

# Directional light emitters and image sensors based on plasmonic metasurfaces

BOSTON UNIVERSITY

COLLEGE OF ENGINEERING

Dissertation

# DIRECTIONAL LIGHT EMITTERS AND IMAGE SENSORS BASED ON PLASMONIC METASURFACES

by

**LEONARD KOGOS**

B.S., Harvard University, 2012
M.S., Boston University, 2016

Submitted in partial fulfillment of the

requirements for the degree of

Doctor of Philosophy

2019

Approved by

First Reader

Roberto Paiella, Ph.D.
Professor of Electrical and Computer Engineering
Professor of Materials Science and Engineering

Second Reader

Anna K. Swan, Ph.D.
Associate Professor of Electrical and Computer Engineering
Associate Professor of Materials Science and Engineering
Associate Professor of Physics

Third Reader

Michelle Y. Sander, Ph.D.
Assistant Professor of Electrical and Computer Engineering
Assistant Professor of Materials Science and Engineering

Fourth Reader

Lei Tian, Ph.D.
Assistant Professor of Electrical and Computer Engineering

*For we are God's handiwork,*
*created in Christ Jesus to do good works,*
*which He prepared in advance for us to do.*
Ephesians 2:10 (NIV)

# Acknowledgments

It takes a village to raise a child and so it goes without saying that I am indebted to many people who have invested in my life and supported me in this journey.

To my late Dad, Joseph Kogos, thank you. I miss you and I draw comfort from knowing you are proud of me. I'm pretty sure you'd have insisted on reading through every single line of this thesis, never mind that this is not your expertise and made edits that somehow would have still made it better. My amazing mum Emily Kogos. You are an inspiration; always the calming influence that helps me put things in perspective. Thank you for your dedication, love support and guidance.

My wonderful wife Anna. You're the best thing that ever happened to me. Thank you for your kindness, patience, love, support and strong friendship. Thank you for always believing in me. Thank you for sacrificing to commute 2 hours by train to work every day for two years so I could have a 5 min commute walk to my research lab. You are the best.

To my wonderful son. Ethan. May you ever grow in wisdom, stature and love. Thank you for your never ending smiles and coos that never fail to bring joy to my heart.

I would also like to express my deep appreciation and gratitude to Prof. Roberto Paiella for his guidance throughout my PhD. His observations, suggestions and inspiration were key to unlocking some of the difficult experimental and theoretical problems during my research. I am also deeply indebted to current and former fellow lab mates in the Prof. Paiella research Lab. They have been my fellow valiant explorers throughout this journey. Khwanchai and Habibe thank you for training me in the various fabrication and imaging

processes. Jeff and John thank you for always being just a phone call away. I also am really grateful for the rest of my esteemed graduate committee; Prof. Min-Chang Lee, Prof. Anna Swan, Prof. Michelle Sander, and Prof. Lei Tian for graciously taking their time to read through my thesis and also guiding me at various points during my PhD.

A very special shout out goes to research staff at the BU Photonics Center. With special mention to Paul Mak and Anlee Krupp.

Finally but not in any way the least, I am grateful for the rest of my family especially siblings (Levi,Angella,Lawrence,Eizabeth,Louis) and friends who have walked with me every step of the way. Thank you for being a never-ending source of support, comfort and a wonderful influence around me.

This work was supported by the Department of Energy, the Samsung Global Research Outreach Program and the National Science Foundation. The FDTD simulations were performed using the Shared Computing Cluster facility at Boston University. 3D image models of the device geometries and experimental setups shown in this work were made in the student version of CATIA V5 software, offered graciously for free by Data Assault Systems, under a student license.

Sincerely,

Leonard Kogos

# DIRECTIONAL LIGHT EMITTERS AND IMAGE SENSORS BASED ON PLASMONIC METASURFACES

**LEONARD KOGOS**

Boston University, College of Engineering, 2019

Major Professor: Roberto Paiella, Ph.D.
Professor of Electrical and Computer Engineering
Professor of Materials Science and Engineering

ABSTRACT

Advances in optical device fabrication techniques and continued research have enabled many exciting new scientific possibilities in the manipulation of light radiation. With the great strides made in nanofabrication technologies and the huge body of work done on nano-related research, we now have a better understand- ing of light-matter interactions at the nanoscale and have the ability to make structures functioning at this scale with unprecedented design flexibility. This has led to an explosion of knowledge in nanooptics and opened great possibilities in light manipulation. In this work we explore the use of nanophotonic structures for the directional control of light emission and photodetection. Typical optoelectoronic devices such as LEDs and light detectors are intrinsically isotropic, and directionality is usually enforced by external optical elements like lenses, pinholes and reflectors. Similarly, standard off-the-shelf light sensors are typically non-directional with a Lambertian angular response profile. Here, we investigate the unique properties of plasmonic metasurfaces that can be harnessed to enforce directionality at the device level, without the

need for bulky and often complex external light control techniques, greatly favoring miniaturization which often allows for faster, more efficient, and cheaper devices. Optimized designs are presented with proof-of-concept simulation results and experimental testing. With these designs, we also explore an exciting new application in imaging, the development of a lens-less ultra-thin flat camera based on the compound-eye vision modality, where each individual imaging unit is a single directional detector.

# Contents

# List of Tables

# List of Figures

# List of Abbreviations

| | | |
|---|---|---|
| CMOS | ..... | Complementary Metal Oxide Semiconductor |
| DI | ..... | De-Ionized |
| EOT | ..... | Extraordinary Optical Transmission |
| FDTD | ..... | Finite Domain Time Difference |
| FOV | ..... | Field Of View |
| GMS | ..... | Gradient Metasurface |
| GSP | ..... | Gap Surface Plasmon |
| HCM | ..... | Homogeneous Continuous Model |
| HSQ | ..... | Hydrogen Silsesquioxane |
| IPA | ..... | Isopropanol |
| IQE | ..... | Internal Quantum Efficiency |
| MIBK | ..... | Methyl isobutyl ketone |
| MSM | ..... | Metal-Semiconductor-Metal |
| NP | ..... | Nanoparticle |
| PMMA | ..... | Polymethyl methacrylate |
| QD | ..... | Quantum Dot |
| SPP | ..... | Surface Plasmon Polariton |

# Chapter 1

# Introduction

## 1.1 Dissertation Objectives

The work presented in this dissertation focuses on the development of directional light sensors and directional light emitters based on specially designed arrays of nanoantennas. We show theoretical work on nanoantenna designs that produce collimated singly beamed emission along arbitrarily tunable directions with high directivity and enhanced radiation efficiency from isotropic light emitters. We also present device designs including experimental data that show enforced highly directional receiving patterns from typically isotropic light detectors. Additionally we present a novel imaging application based on the compound eye vision modality that applies the aforementioned directional light detectors to realize an ultra-thin, flat lens-less camera.

## 1.2 Main Results

In this section we highlight the main results presented in this dissertation. They are referenced to the corresponding relevant publication list at the end of this section.

### 1.2.1 Light Emission Near a Gradient Metasurface - Section 3.1

The optical Gradient-Meta Surface (GMS) is briefly introduced and its influence on light emission properties through near-field interaction is investigated numerically. This is accomplished by applying the Homogenized Continuous Model (HCM) (a generic model valid for investigating properties of any GMS irrespective of its underlying physical implementation). General theoretical arguments supported by rigorous numerical simulations are presented. We show the unique ways in which appropriately designed GMSs can enable near-field directional light control through enabling distinctive coupling of radiation into specific evanescent and propagating modes as determined by their phase gradients. We also briefly touch on possible advanced beam-shaping functionalities that can be enabled by GMS phase profiles of increased complexity. [1]

### 1.2.2 Directional Light Emitter - Section 3.2

A specific implementation of a GMS designed to enable directional radiation beaming from a collection of randomly positioned and randomly phased isotropic light emitters is explored theoretically and verified both numerically and experimentally for which preliminary measured data is presented. [2]

### 1.2.3 Directional Light Detector - Section 4.2

We demonstrate hybrid plasmonic grating-GMS designs that enable highly directional light detection from off-the shelf typically isotropic planar light sensors. This includes both theoretical simulations and experimental results showing directional light detection. With our designs, we show polarized peak transmission of 35% - 45% with a wide tuning range of up to ±75° and high angular selectivity of less than 10° at full width half max. In addition, we also demonstrate that these GMS designs can be readily scaled for different target wavelengths and fabricated with standard CMOS processes, making them applicable to practical devices.[3]

### 1.2.4 Lens-Less Compound Eye Camera Design - Section 4.3.4

Using the directional light detectors mentioned above, we also explore the design of a lens-less camera based on the compound eye vision modality. In this framework, each pixel of the sensor is a directional imaging cell collecting light from a single point on the object as dictated by its response function. Through computational imaging, we can reconstruct super-pixel-resolved images from the combined
directional information obtained from a specific pixel arrangement. We show theoretical simulations demonstrating proof of concept designs and successful image recovery. [3-5]

**Main Results Publication List:**

1. LC Kogos, R Paiella, (2016) **Light Emission Near a Gradient Metasurface**, ACS Photonics 3 (2), 243-248

2. X Wang, LC Kogos, R Toufanian, A Dennis, R Paiella, (2018) **Beamed Light Emission near a Gradient Metasurface**, CLEO: QELS_Fundamental Science, FF1H.2

3. LC Kogos, L Tian, R Paiella, (2018) **Directional Plasmonic Image Sensors for Lens-Free Compound-Eye Vision**, CLEO: Science and Innovations, SF1J. 5

4. LC Kogos,Y Li, J Liu, Y Li, L Tian, R Paiella, (2019) **Metasurface Photodetectors for Directional Image Sensing**, META19 conference

5. LC Kogos,Y Li, J Liu, Y Li, L Tian, R Paiella, **Plasmonic Ommatidia for Lensless Compound-Eye Vision**, (Paper in preparation)

# Chapter 2

# Fundamental Concepts

## 2.1 Surface Plasmon Polaritons and Localized Surface Plasmons

Plasmonics, which is the study of the interaction between electromagnetic radiation (in a dielectric medium) and plasma waves(in metallic materials), is especially fascinating since it allows for the indirect control of light radiation by modifying properties of the metallic medium.

There are two main types of plasmonic oscillations that are essential to the work described in this thesis: Localized Surface Plasmon Resonances (LSPRs) and Surface Plasmon Polaritons (SPPs). SPPs are a special type of hybrid coupled mode consisting of plasma waves at the surface of a metal and electromagnetic waves in the adjacent dielectric medium. SPPs travel along and are evanescently confined to the metal-dielectric interface. In this work we will only consider SPPs on a single metal-dielectric interface. LSPRs on the other hand are geometrically bound charge oscillations that are excited by incident radiation in sub-wavelength metallic nanoparticles (NPs). This collective movement of electrons in the NP can also re-radiate light (as a consequence of accelerating charged particles) effectively making the resonant NPs quasi-dipoles capable of emitting both radiative and non-radiative field components. It is important to note that LSPRs and SPPs being distinct plasmonic oscillations have different properties and behave differently in different contexts. For example, LSPR excitation to a large extent does not depend on the incident angle for light impinging on a plasmonic nanostructure whereas

for an appropriately designed plasmonic grating you can only couple into SPP modes when incident from a specific angle. It is therefore important to take great caution if you are working in a regime where both oscillation modes are allowed in order to distinguish between effects emanating from the two.

Physical properties of SPPs and LSPRs are best investigated from their dispersion relations and resonant frequencies respectively. These can be derived from Maxwell's equations while taking into account appropriate boundary conditions at the interface between the metallic and dielectric materials. A complete derivation of SPPs and LSPRs can be found in many elementary electromagnetic textbook (e.g. (Maier, 2010) that covers the topic of plasmonics. Here we briefly go over the main steps of this derivation, to develop some intuition.

### 2.1.1 SPP Dispersion

We will begin with Maxwell's equations in the form below:

$$\nabla \cdot \mathbf{D} = \rho_{ext} \tag{2.1a}$$

$$\nabla \cdot \mathbf{B} = 0 \tag{2.1b}$$

$$\nabla \times \mathbf{E} = -\frac{\partial \mathbf{B}}{\partial t} \tag{2.1c}$$

$$\nabla \times \mathbf{H} = \mathbf{J_{ext}} + \frac{\partial \mathbf{D}}{\partial t} \tag{2.1d}$$

In these equations, $\mathbf{D}$ is the electric displacement flux, $\mathbf{E}$ is the electric field of the incident radiation, $\mathbf{H}$ is its magnetic field, and $\mathbf{B}$ is the resulting magnetic induction. $\rho_{\mathbf{ext}}$ and $\mathbf{J_{ext}}$ are the external charge and current densities, respectively. Limiting ourselves to linear, isotropic, nondispersive, uniform and nonmagnetic

media we have the following constitutive relations:

$$\mathbf{D} = \varepsilon_0 \varepsilon \mathbf{E} \tag{2.2a}$$

$$\mathbf{B} = \mu_0 \mathbf{H} \tag{2.2b}$$

By combining the curl equations 2.1a,2.1b we get the general wave equation:

$$\nabla^2 \mathbf{E} - \frac{\varepsilon}{c^2} \frac{\partial^2 \mathbf{E}}{\partial t^2} = 0 \tag{2.3}$$

Assuming harmonic time dependence for the fields involved this can be further simplified into the Helmholtz equation:

$$\nabla^2 \mathbf{E} + k_0^2 \varepsilon \mathbf{E} = 0 \tag{2.4}$$

Where $k_0 = \frac{\omega}{c_0} = \frac{2\pi}{\lambda_0}$ is the free-space wavenumber.

From this point a typical way to proceed is solving this wave equation separately on both sides of the interface and matching the resulting solutions with application of appropriate boundary conditions at the interface. However, another way to approach this is to use the intuition about what kind of fields we are expecting for the SPPs, write an appropriate mathematical description and apply the boundary conditions at the interface. We will take the latter approach.

For simplicity, we only consider SPPs at a single interface (dielectric-metal) since in this work we will be coupling free space beams into such a surface. However this analysis can be easily extended to hybrid structures with multiple interfaces. Let us take a planar geometry as shown in Fig. 2·1 with our axis defined as indicated, with assumed infinite extents in the metal and dielectric away from the interface.

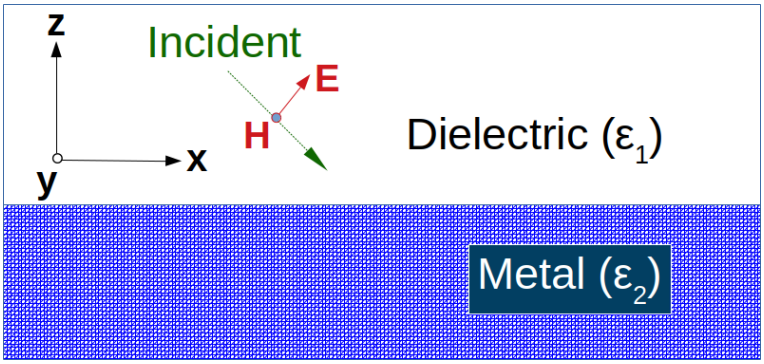


**Figure 2·1:** Planar geometry used to derive the SPP dispersion relation. The green arrow is the p-polarized incident light showing the electric field (E) orientation (red arrow) which is in the x-z plane and the magnetic field (H) which is in the x-y plane).

Solutions to the Helmholtz equation can generally be classified into s-polarized and p-polarized electromagnetic modes. P-polarization (*parallel*)also known as the transverse-magnetic (TM) mode, refers to the orientation where the electric field (**E** ) is parallel to the plane of incidence and the magnetic field (**H** ) perpendicular to it. S-polarization (from *senkrecht*, German) also known as the transverse-electric (TE) mode, refers to the orientation where the magnetic field (**H** ) is parallel to the plane of incidence and the electric field (**E** ) is perpendicular to it. For fields propagating along and evanescently confined to an interface, it can be shown that s-polarized modes are not supported. This leaves us with the p-polarized modes. Choosing $x$ as our propagation direction, we can write:

$$\mathbf{E}_j = \begin{pmatrix} \mathbf{E}_{x_j} \\ 0 \\ \mathbf{E}_{z_j} \end{pmatrix} e^{ik_{zj}z} e^{i(k_x x - \omega t)} \qquad j = 1, 2 \tag{2.5}$$

$$\mathbf{H}_j = \begin{pmatrix} 0 \\ \mathbf{E}_{y_j} \\ 0 \end{pmatrix} e^{ik_{zj}z} e^{i(k_x x - \omega t)} \qquad j = 1, 2 \tag{2.6}$$

Where $j = 1, 2$ indicates the dielectric and metal medium ,respectively.

Using the Helmholtz equation applying our boundary conditions, from this set of equations we get the following:

$$k_x^2 + k_{z_j}^2 = \varepsilon_j k_0^2 \qquad j = 1, 2 \tag{2.7a}$$

$$\mathbf{k}_x \mathbf{E}_{x_j} + \mathbf{k}_{z_j} \mathbf{E}_{z_j} = 0 \qquad j = 1, 2 \tag{2.7b}$$

$$\mathbf{E}_{x_1} - \mathbf{E}_{x_2} = 0 \qquad \left(\text{tangential } \mathbf{E} \text{ continuous}\right) \tag{2.7c}$$

$$\varepsilon_1 \mathbf{E}_{z_1} - \varepsilon_2 \mathbf{E}_{z_2} = 0 \qquad \left(\text{ normal } \mathbf{D} \text{ continuous}\right) \tag{2.7d}$$

The non-trivial solution to these coupled equations gives us the SPP dispersion relation:

**SPP Dispersion**

$$k_x^2 = \frac{\varepsilon_1 \varepsilon_2}{\varepsilon_1 + \varepsilon_2} k_0^2 \tag{2.8}$$

$$k_{zj}^2 = \frac{\varepsilon_j^2}{\varepsilon_1 + \varepsilon_2} k_0^2 \qquad j = 1, 2 \tag{2.9}$$

On further inspection we also see that for us to have bound surface waves (i.e. $k_{zj}$ imaginary), the following has to hold:

$$\varepsilon_1\left(\omega\right)\varepsilon_2\left(\omega\right) < 0 \tag{2.10a}$$

$$\varepsilon_1\left(\omega\right) + \varepsilon_2\left(\omega\right) < 0 \tag{2.10b}$$

For most metals in the optical regime, their dielectric functions can be approximated by the Drude model (Maier, 2010). This model equates metals to a sea of de-localized electrons randomly moving within the metal colliding with the relatively immobile positive ions that make up the metal lattice. From the Drude model we have the following dielectric function:

$$\varepsilon(\omega) = 1 - \frac{\omega_p^2}{\omega^2} \tag{2.11}$$

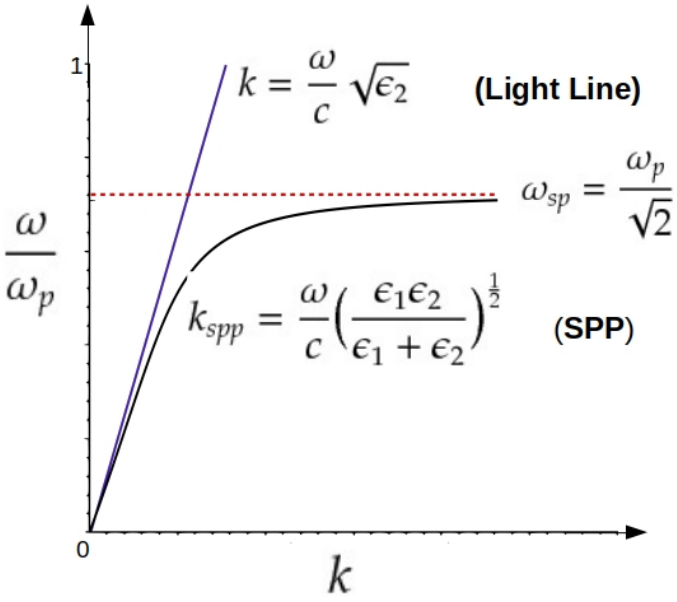


**Figure 2·2:** SPP Dispersion Curve

From the resulting dispersion curve shown in Fig. 2·2, the SPP dispersion line always lies to the right of the light line. The main consequence of this is that there is always a momentum mismatch between SPPs and free space radiation at the same frequency. Therefore, in order to excite SPPs with free-space radiation we need a coupling mechanism that can impart extra momentum in the SPP propagation direction, enabling momentum matching. There are several techniques that can be applied to achieve this. They include grating coupling, prism coupling, near-field coupling among others. In this work we will be heavily relying on the grating coupling mechanism as we utilize SPP modes for near-field directional filtering of allowed coupling modes of incident light or beamed radiation.

### 2.1.2 LSPR Wavelengths

For the derivation of LSPR frequencies, you would have to follow a similar procedure, except that in this case the boundary conditions are more complicated since they are determined by the NP geometry. A complete treatment of this topic is beyond the scope of this thesis. However you can find an example of one such derivation for a spherical shaped NP in (Willets and Van Duyne, 2007) or many advanced electro-magnetics textbooks that cover this topic.

## 2.2 Plasmonic Grating Coupling

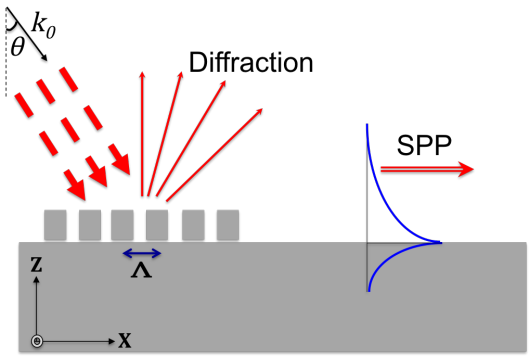


**Figure 2·3:** Plasmonic grating coupling

SPP grating couplers are specially designed planar periodic arrangements of metallic NPs that diffract incident radiation in such a way so as to impart additional in-plane momentum, allowing for coupling to SPP modes. Important parameters that govern this interaction are the grating periodicity ($\Lambda$), incident radiation wavelength ($\lambda_0$) and shapes/dimensions of the constituent diffractive elements. These parameters altogether affect the coupling efficiency, determine the allowed incident angles, and also influence the light reflection or transmission phase properties. Let's consider the example of a 1-Dimensional grating with periodicity $\Lambda$ as shown in Fig 2·3. This grating will impart in-plane momentum to incident radiation equal to its grating momentum $g = \pm m\frac{2\pi}{\Lambda}$ upon diffraction. Here, $m$ is a positive integer indicating the diffraction order. As a result, for radiation incident at an angle $\theta$ relative to the surface normal, its momentum vector component along the surface $\beta$ upon diffraction will be equal to the incident light horizontal momentum component plus the additional momentum due to diffraction as shown here:

$$\beta = k_0 \sin\theta \pm m\frac{2\pi}{\Lambda} \tag{2.12}$$

SPP coupling can occur whenever the following condition is fulfilled:

$$k_0 \sin\theta \pm m\frac{2\pi}{\Lambda} = \pm k_0 n_{SPP} \tag{2.13}$$

where $n_{SPP}$ is the SPP effective refractive index (i.e. $k_0 n_{SPP}$ is the corresponding SPP wavenumber at the incident light frequency.)
This analysis/description can be extended to higher dimensions allowing for more complex coupling designs.

By reciprocity, any SPPs travelling along the grating may also be diffracted into specific angled beams as dictated by the diffraction condition. Consequently, if a dipole or any emitter with evanescent fields is placed close enough to a plasmonic grating, it could couple directly to SPPs which may be consequently diffracted, leading to beamed emission in the far-field. This is the basic principle we rely on for beamed emission in our designs.

## 2.3 Gradient Metasurfaces

Linearly graded optical Metasurfaces have emerged in recent years from extensive research in nanooptics (Yu et al., 2011),(Ni et al., 2012),(Sun et al., 2012a),(Sun et al., 2012b),(Aieta et al., 2012),(Genevet et al., 2012),(Xu et al., 2013),(Yin et al., 2013),(Karimi et al., 2014),(Pors et al., 2014),(Lin et al., 2014) and have great potential for nanoscale control of radiation properties. They are effectively plasmonic gratings with specially designed repeat units that create a linear relative phase shift along the surface in light reflected or transmitted through them. This linear phase shift breaks the symmetry that is normally found in typical diffraction gratings suppressing all diffraction orders except for the +1 order. The grating momentum of a gradient metasurface (GMS) is determined by the transmission or reflection phase gradients in addition to the periodicity of constituent nanostructures. Optical Metasurfaces are able to abruptly change the phase of incident radiation over distances much shorter than the wavelength. This greatly favors miniaturization compared to refractive elements whose functionality relies on gradual phase change accumulation over several wavelengths. In our work here, we apply specially designed GMSs for directional light coupling and emission.

Phased array functionality in general can be understood from the perspective of the classical Huygens' construction. In this framework, each point on a wavefront of radiation is described as a point source, emitting a secondary spherical wavelet spreading out in the forward direction. At any one time, the total wave front is the envelope that encloses all of these wavelets from a previous wavefront and is defined by their surface tangents as seen in Fig. 2·4. On an optical metasurface, we are able to create abrupt phase changes over sub-wavelength distances such that we can alter these individual wavelets in a way

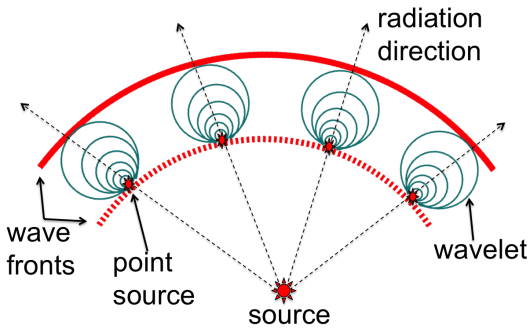


**Figure 2·4:** Figure showing Huygens' construction description of propagating radiation. The wavelets shown in green create a wave front with their combined surface tangents as they spread in the forward direction of propagation.

that allows us to create any arbitrary wavefront. With this picture in mind, when designing optical phased-array metasurfaces, our main goal is to control the local reflection/transmission phase by placing appropriately designed NPs in specific pre-defined locations on a surface. Each of these NPs has a different pre-determined phase response typically dictated by its material properties and geometry. In addition to modifying the phase relation of the secondary wavelets thus altering the wave fronts of the incident radiation, these NPs could also have polarization dependent responses, allowing us to engineer for polarization.

From the Lorentz model (which is the most general material response model to electromagnetic energy), electrons in a material exposed to electromagnetic fields react as a damped harmonic oscillator described by the equation:

$$m\frac{\partial^2 x}{\partial t^2} + d\frac{\partial x}{\partial t} + Kx = eE_{loc} \tag{2.14}$$

Where: $m$ is the electron mass, $d$ is a damping term, $K$ is the restoring force, $e$ is the magnitude of the electronic charge and $E_{loc}$ is the local driving field acting on the electron. Assuming harmonic incident radiation, we get a general solution

whose oscillatory part has the form:

$$x_{amp} = \frac{(e \setminus m)E_{amp}}{\omega_0^2 - \omega^2 - i\gamma\omega} \tag{2.15}$$

where: $\omega_0^2 = K \setminus m$ and $\gamma = d \setminus m$. $x_{amp}$ and $E_{amp}$ refer to the x-displacement and local electrical field amplitudes respectively. This can be re-written as:

**Lorentz Oscillator Response**

$$x_{amp} = Ae^{i\Theta}\left(eE_{amp}/m\right) \tag{2.16}$$

$$A = \frac{1}{\left[\left(\omega_0^2 - \omega\right)^2 + \gamma^2\omega^2\right]^{1/2}} \tag{2.17}$$

$$\Theta = tan^{-1}\left(\frac{\gamma\omega}{\omega_0^2 - \omega^2}\right) \tag{2.18}$$

If we plot this response as a function of frequency, we get the classic Lorentz oscillator response shown in Fig. 2·5.

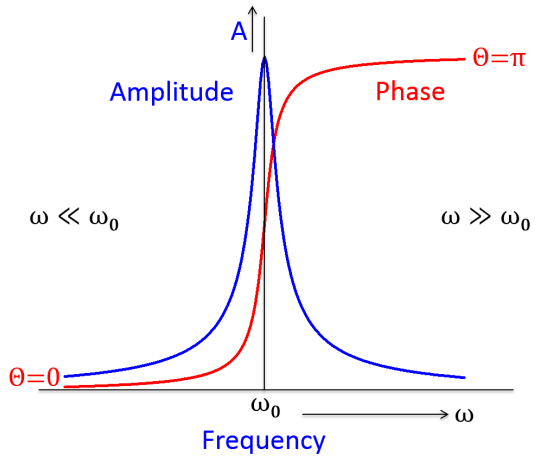


**Figure 2·5:** Lorentz oscillator response.

From Fig. 2·5 we can see that as the driving frequency $\omega$ is swept across the resonance (when $\omega$ is equal to the resonance frequency $\omega_0$), there is a sharp phase shift of $\pi$ in the oscillator's response. At the same time, at resonance the oscillator

amplitude peaks at its highest possible value. In a physical material, the various parameters in the Lorentz oscillator equation are specific material properties. In metallic materials when applying this model, you do not have a single oscillator but rather a sea of de-localized electrons within a relatively rigid lattice. This can be modeled as a collection of Lorentz oscillators. Consequently, NPs under radiative illumination undergo a phase delay of up to $\pi$ in their response, as we sweep across their resonance frequency as predicted by the Lorentz oscillator model. The NP absorbs incident radiation which sets up charge oscillations within it. The de-localized electrons in the NP collectively move in response to the electric field resulting in charge oscillations. These collective oscillations can result in re-radiation of energy effectively making the NP a dipolar nanoemitter with an intrinsic phase delay predicted by Lorentz oscillator model, relative to the incident radiation. Consequently, the re-radiated light has an extra phase delay of up to $\pi$ depending on how close the incident radiation frequency is to the NP's resonance frequency dictated by its geometry and material properties. By appropriately selecting the NP geometry we can engineer its phase response. Placing specially designed NPs at specific locations on a surface, one can effectively engineer its local phase response to incident light.

With a single Lorentz-like oscillator we only have relative phase control over a 0 to $\pi$ range (Pors et al., 2011), (Zhao and Alù, 2011), (Roberts and Lin, 2012), (Lin et al., 2010). To make useful phased arrays, we typically need to cover the full $2\pi$ range. One way this problem is solved is by use of a metal film placed in close proximity to the NPs, separated by an optically thin dielectric spacer similar to the design of reflect array antennas(Pozar et al., 1997). The presence of a metallic film in close proximity sets up image dipoles that can couple to the aforementioned NP dipole resonators increasing the phase response by another $\pi$ range. The metal

film typically supports SPP modes and thus these structures are known as Gap Surface Plasmon(GSP) metasurfaces(Pors et al., 2014). With this system of NPs backed by and thinly separated from a metal film we have relative phase control over the whole $2\pi$ range as desired. This gives us tremendous design flexibility. In GSP metasurfaces, the phase response is influenced by not only the NP geometry and material properties but also by the separation distance between the resonators and the backing metal film.

## 2.4 Extra-Ordinary Optical Transmission

Extraordinary Optical Transmission (EOT) is a phenomenon of resonant enhanced light transmission through an array of sub-wavelength apertures in an opaque metallic surface (van Beijnum et al., 2012) which ordinarily owing to the sub-wavelength nature of the perforations is expected to greatly suppress or block direct light transmission. This effect was first discovered by (Ebbesen et al., 1998) in 1998. It is understood to occur due to two main processes (Porto et al., 1999):

1. Excitation of coupled SPP resonances on both sides of the surface allowing transfer of energy from one side to the other through the apertures.

2. Coupling of incident light to waveguide resonances located in the apertures which can radiate on the other side of the surface.

In this work, we use this phenomenon to couple SPPs on the top layer of our directional light sensor gratings to radiative modes in the device active layer for photo-detection.

## 2.5 Computational Imaging

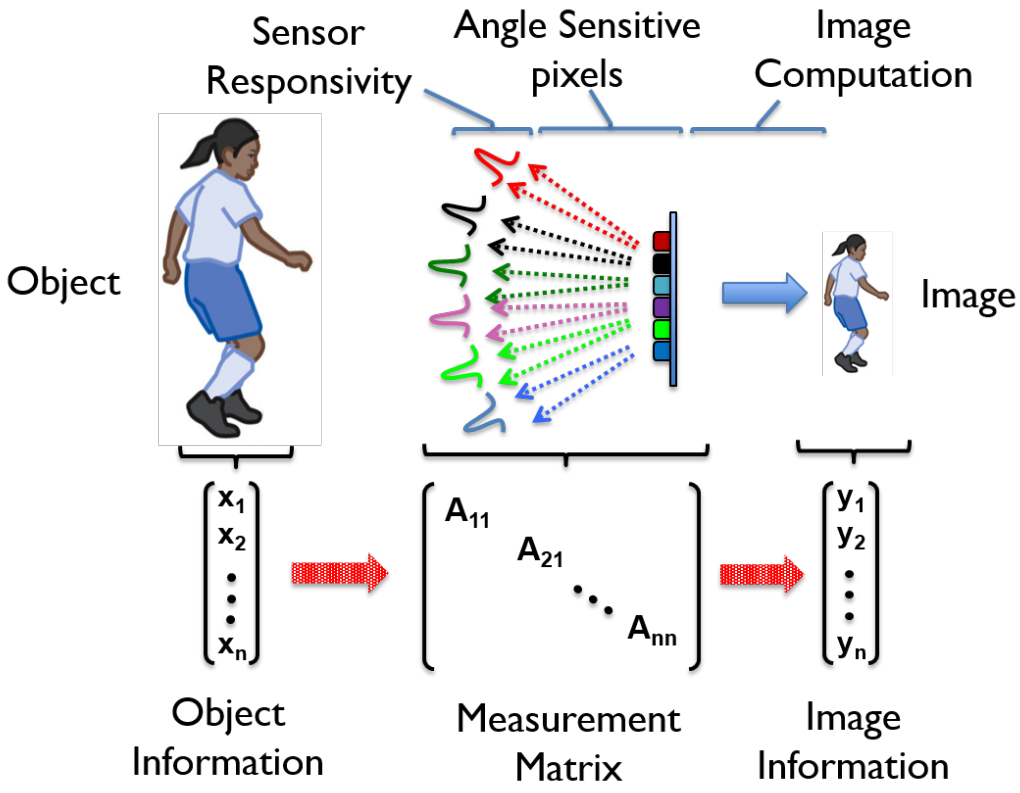


**Figure 2·6:** Schematic showing the computational imaging process.

Computational imaging is an emerging field at the interface between optics and signal processing (Neifeld and Shankar, 2003), (Nayar, 2006), (Healy and Brady, 2008), (Raskar, 2009). It involves collecting light from an object in radically different ways from typical cameras and computationally extracting useful visual information from it. In the work covered in this thesis, in collaboration with Prof. Lei Tian's group at Boston University, we develop and apply a specific computational imaging method reconstruct an image from the directional intensity information obtained from a specially designed array of sensors in a lens-less compound eye camera design. This algorithm can be summarized in two steps

shown schematically in Fig. 2·6.

These steps are:

1. The image formation process is modeled as a linear system defined by a measurement matrix (Matrix **A** in Fig. 2·6) that relates the acquired intensity information (Matrix **y** in Fig. 2·6) to the object (Matrix **x** in Fig. 2·6). This measurement matrix is typically an n by n matrix where n is the number of directional pixels. It contains the directional responsivity of the individual constituent sensors including any overlap in their sensing portions of the object.

2. Computation reconstruction involves appropriately inverting the measurement matrix and applying it to the acquired intensity information in matrix **y** to reconstruct a pixel super-resolved image of the object.

# Chapter 3

# Directional Light Emitters

## 3.1 Light Emission near a Gradient Metasurface

It is well established that spontaneous emission of light is not an intrinsic process with its properties solely determined by the emitters. On the contrary, radiative properties like the decay rate are also influenced by the density of available photonic modes, which in turn is determined by the emitter's dielectric environment. By altering this environment we can alter the density of available photonic modes and consequently influence the properties of the emitted radiation. The study of this phenomenon dates back to Purcell's pioneering work (Purcell, 1946) with radio waves in 1946. In photonics, the control of spontaneous emission by altering the local density of modes was first demonstrated in the context of fluorescence near a planar surface (Drexhage, 1974), (Ford and Weber, 1984), (Barnes, 1998). Subsequently, this technique has also been explored with optical emitters embedded within three-dimensional artificial structures of varying complexity including micro-cavities (Gérard et al., 1998), photonic crystals (Yablonovitch, 1987), (Noda et al., 2007) and hyperbolic meta-materials (Krishnamoorthy et al., 2012) or coupled to individual metallic NPs (Novotny and Van Hulst, 2011). However, decay rates are not the only property of light emitters that can be controlled by altering the emitter's local dielectric environment. In plasmonics, planar nanostructured metal films have been used through near-field excitation of SPPs not only to enhance the decay rate of adjacent light emitters

(Amos and Barnes, 1997), (Gontijo et al., 1999), (Shimizu et al., 2002), (Okamoto et al., 2004), (Paiella, 2005), (Song et al., 2005), (Mertens et al., 2006), (Sun et al., 2007) but also to control directionality of their emitted light,(DiMaria et al., 2013), (Boroditsky et al., 1999), (Erchak et al., 2001), (Greffet et al., 2002), (Rattier et al., 2003), (Cesario et al., 2007), (Wierer Jr et al., 2009), (Kurosaka et al., 2010). However, in all these prior works the radiation pattern typically consists of either a single beam normal to the device surface or two or more directional beams at equal and opposite angles. One great advantage of GMSs is that they can provide single directional beaming even off axis which is attractive for applications requiring beamed emission. Another application of GMSs not yet explored is directional light coupling. Just like a GMS is able to diffract coupled SPPs into a single beaming direction, by reciprocity, unless we are dealing with non reciprocal media (Potton, 2004) then we can expect it to effectively couple collimated light from a single incidence direction into SPPs. If we can detect the presence of these resultant SPPs then we effectively have a directional light detector. This is the design approach pursued in this work.

Examples of application areas that would benefit from directional light emission include solid-state smart lighting, (where directional light emitting diodes can be used for novel functionalities like optical wireless communication besides providing illumination), highly multiplexed fluorescence sensing (with the directionality of the emitted light used to discriminate between different regions of a sample), and structured illumination for 3D displays. Directional photo-detection is also attractive for optical wireless communication where it can be used to discriminate between different sources of signals. Furthermore, it can also be harnessed to enable novel ultra-thin imaging systems based on non-conventional modalities, such as the compound eye lens-less camera described in subsequent

chapters.

In order to understand the influence of a GMS on light emitters, we start with its most general description, the homogenized continuum model (HCM) (Sun et al., 2012a) shown in Fig. 3·1(a), which can be applied to any (reflective) GMS, regardless of the detailed implementation of the nanoantenna array. The light source here is a simple electric dipole, as appropriate to the description of spontaneous emission in typical luminescent media. Our results show that the dipole radiation output is dramatically affected by the nearby GMS, in several important and unusual ways. First, the spontaneous decay rate can be strongly enhanced through near-field interactions, by an amount that depends on the dipole lateral position in an oscillatory fashion. Second, highly asymmetric directional radiation patterns can be produced with broad geometrical tunability of the angle of peak emission. Furthermore, the total output radiation power can be increased in the case of low-efficiency emitters or quenched in favor of asymmetric surface-wave excitation depending on the GMS phase gradient. These results shed new light on the distinctive properties of GMSs and underscore their potential to enable novel applications involving, for example, extremely miniaturized and high-speed light-emitting devices, photonic integrated circuits, or highly multiplexed fluorescence sensors.

### 3.1.1 Theoretical Description

Our HCM consists of a perfect electric conductor (PEC) coated with a metamaterial slab of highly sub-wavelength thickness $\delta$, and position-dependent permittivity $\varepsilon$ and permeability $\mu$. In this geometry, illustrated schematically in Fig. 3·1(a), the phase shift upon reflection for a normally incident harmonic plane wave is $\Phi = 2Re\{\sqrt{\varepsilon\mu}\}k_0\delta$, where $k_0 = \frac{2\pi}{\lambda_0}$ is the free-space wavenumber. A linear phase gradient $\xi$ along any specific in-plane direction (e.g., the $x$ direction) is then

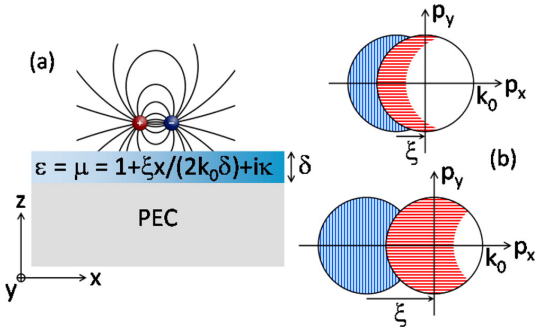


**Figure 3·1:** (a) Schematic cross-section of the GMS model used in this work. (b) Distribution of the non-radiative plane-wave components of the dipole field $\mathbf{E}_{dip}$ (blue) scattered by the GMS into radiation (red), for a GMS of $\frac{\xi}{k_0} = 0.6$ (upper plot) and $\frac{\xi}{k_0} = 1.4$ (lower plot). Here **p** denotes the in-plane wave vector.

obtained with $\varepsilon = \mu = 1 + \frac{\xi x}{2k_0\delta} + i\kappa$ (Sun et al., 2012a) which gives $\Phi = 2k_0\delta + \xi x$. The imaginary term $\kappa$ in this expression accounts for the GMS absorption losses and therefore determines the normal-incidence power reflection coefficient $R = exp\Big( -4Im\{\sqrt{\varepsilon\mu}\}k_0\delta\Big)$. Because of the phase gradient $\xi\mathbf{x}$, light incident with in-plane wave vector **p** is diffractively scattered into a reflected wave of wave vector components parallel and perpendicular to the GMS given by $k_{\|,r} = \mathbf{p} + \xi\mathbf{x}$ and $k_{\perp,r} = \sqrt{k_0^2 - k_{\|,r}^2}$, respectively. At the same time, all other diffraction orders including specular reflection are completely suppressed. If $k_{\|,r} < k_0$, $k_{\perp,r}$ is real and the reflected wave propagates away from the surface with a non-specular angle of reflection: $\theta_r = atan\Big(\frac{k_{\|,r}}{k_{\perp,r}}\Big)$ (anomalous reflection). Otherwise, $k_{\perp,r}$ is imaginary and a surface wave bound to the GMS is produced.

In practice, the behavior just described can be obtained with a planar array of ultra thin antennas (e.g., H or rectangular-shaped (Sun et al., 2012a),(Sun et al., 2012b),(Pors et al., 2014)) of varying size, separated from a metal-film "ground plane" by a thin dielectric layer. Compared to designs without a metallic substrate, such reflective GMSs can provide substantially improved scattering

efficiency. For instance, in (Sun et al., 2012b) a relatively large power reflection coefficient R of 80% was measured at visible wavelengths (850 nm). Due to the discrete nature of the individual nanoantennas, the phase gradient of these arrays is essentially discretized into a staircase of roughly equal phase steps. While the model system of Fig. 3·1(a) does not account for this granularity, it has already been used effectively to describe prior experimental work involving the reflection of externally incident light from GMSs. (Sun et al., 2012a),(Xu et al., 2013) Its applicability to the study of GMS-enhanced light emission is discussed in section 3.1.3 below, together with additional simulation results obtained with a specific design from the literature consisting of a discrete arrangement of patch nanoantennas.(Sun et al., 2012b) The key conclusions presented here based on the homogenized continuum model of Fig. 3·1(a) are confirmed by these additional simulations.

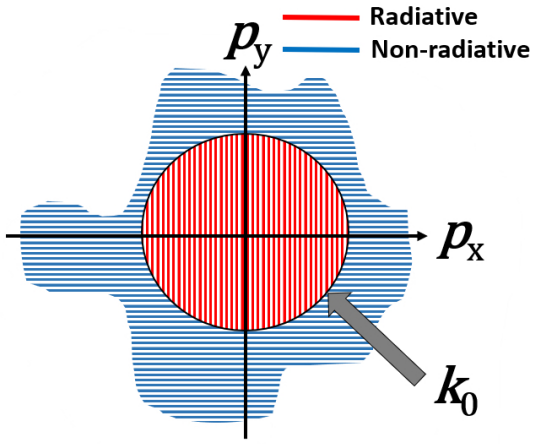


**Figure 3·2:** Schematic showing dipole field components on the $p_x$, $p_y$ momentum plane.The light cone (where: $k_0 = \sqrt{p_x^2 + p_y^2}$) is represented by the black circle enclosing the radiative dipole field components shown as red dashed lines while the non-radiative components are blue dashed lines outside the circle.

The radiative properties of a dipole near a surface such as the GMSs under

study can be described using a semi-classical model of luminescence, where the spontaneous emission rate $\Gamma_{sp}$ is computed from the work per unit time done by the dipole on the electromagnetic field, divided by the photon energy.(Ford and Weber, 1984),(Barnes, 1998) In this approach, $\Gamma_{sp} = \frac{-1}{2\hbar}\,\mathrm{Im}\{\mu * .\mathbf{E}_{tot}\}$, where $\mu$ is the dipole moment and $\mathbf{E}_{tot}$ is the total (emitted plus reflected) electric field at the dipole location. In this picture, the electric field directly emitted by the dipole $\mathbf{E}_{dip}$ can be expanded in a superposition of plane waves of complex amplitudes $\mathbf{E}_{dip}\left(\mathbf{p}\right)$ for all values of the in-plane wave vector $\mathbf{p}$ (including evanescent terms with $\mathbf{p} > k_0$). Here the radiative components lie within the light cone defined by $k_0 = \sqrt{p_x^2 + p_y^2}$ while the evanescent components lie outside the light cone. Fig. 3·2 shows this representation of the dipole field in the $p_x$, $p_y$ momentum plane. Here the light cone is the black circle enclosing the radiative dipole field components shown as red dashed lines, while the non-radiative components outside the light cone are shown as blue dashed lines. At the GMS, each such field component produces a reflected wave(also possibly evanescent) of in-plane wave vector $\mathbf{p}+\xi\mathbf{x}$ and complex amplitude $\mathbf{E}_r\left(\mathbf{p}+\xi\mathbf{x}\right) \propto \mathbf{E}_{dip}$. The spontaneous emission rate can then be written as:

$$\Gamma_{sp} = -\frac{1}{2\hbar}\int \mathbf{dp}\ \mathrm{Im}\{\mu * .[\mathbf{E}_{dip}\left(\mathbf{p}\right) + \mathbf{E}_r\left(\mathbf{p}+\xi\mathbf{x}\right)]\} \tag{3.1}$$

with $\mathbf{E}_r\left(\mathbf{p}+\xi\mathbf{x}\right)$ and $\mathbf{E}_{dip}\left(\mathbf{p}\right)$ computed at the dipole location. Each term in the integral of Eq. 3.1 measures the probability per unit time that the dipole emits light with in-plane wave vector $\mathbf{p}$. This probability can be strongly enhanced by the GMS if the reflected field is large at the dipole location and has the proper phase relationship with the dipole so as to reinforce its oscillations. With this framework, we can present the following picture of light emission near a GMS.

The propagating waves $\mathbf{E}_{dip}\left(\mathbf{p}\right)$ (with $\mathbf{p} < k_0$) emitted by the dipole toward

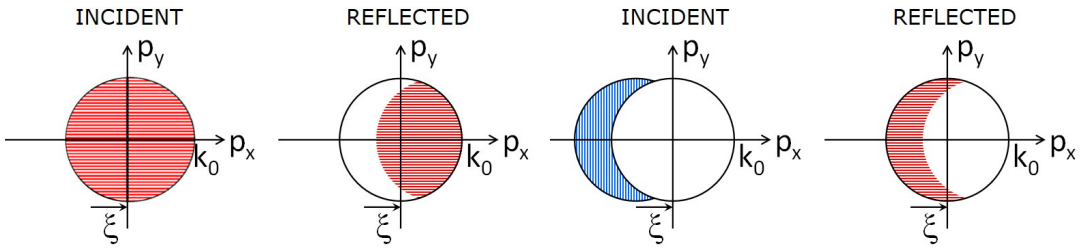


**(a)** Radiative components of a dipole field near a GMS.

**(b)** Evanescent components of a dipole field near a GMS

**Figure 3·3:** Radiative and non-radiative components of a dipole in the $p_x$ $p_y$ plane shown before an after reflection by an example GMS with phase gradient $\xi$.

the GMS are scattered into either anomalously reflected waves or surface waves depending on the value of **p**. The resulting surface waves are bound to the GMS and cannot radiate. At the same time, if the dipole distance $d$ from the GMS is much smaller than the wavelength $\lambda_0$, they can produce a large contribution to Eq. 3.1, by virtue of the strong field confinement of evanescent waves near the surface. As a result, the dipole decay rate $\Gamma_{sp}$ is enhanced. In addition, for $d << \lambda_0$ some of the evanescent components of $\mathbf{E}_{dip}$ can be diffracted by the GMS into propagating waves and therefore contribute to both the decay-rate enhancement and the radiation output. This process is illustrated schematically in Fig. 3·1(b) for two values of the normalized phase gradient $\frac{\xi}{k_0}$ (0.6 and 1.4). In these plots, the center circle of radius $k_0$ is the boundary of the light cone at the dipole radiation frequency. The vertically dashed region is the set of all evanescent components of $\mathbf{E}_{dip}$ that can be diffractively scattered into radiation, and the resulting propagating waves are contained in the horizontally dashed region. In Fig. 3·3, we show the expected effect a generic GMS of phase gradient $\xi$ has on the light radiated from a nearby dipole, as it increases the in-plane momentum of the incident radiation by $\xi$ upon reflection. Since this radiation mechanism is

mediated by near-field interactions involving highly confined evanescent fields, it can be expected to occur with high probability and thus dominate the dipole emission. Under these conditions, the far-field radiation pattern will consist of plane-wave components mostly from within the horizontally dashed region of Fig. 3·1(b), resulting in directional emission. Finally we note that, in the geometry under study, the local phase difference between any incident plane wave and its reflection varies periodically as a function of $x$ with period $\frac{2\pi}{\xi}$(i.e., the distance over which the GMS reflection phase $\Theta$ changes by $2\pi$). Since the dipole decay rate of Eq. 3.1 depends strongly on this phase relationship, it can be expected to undergo similarly periodic variations with the dipole position along the $x$ direction.

### 3.1.2 FDTD Simulation Results

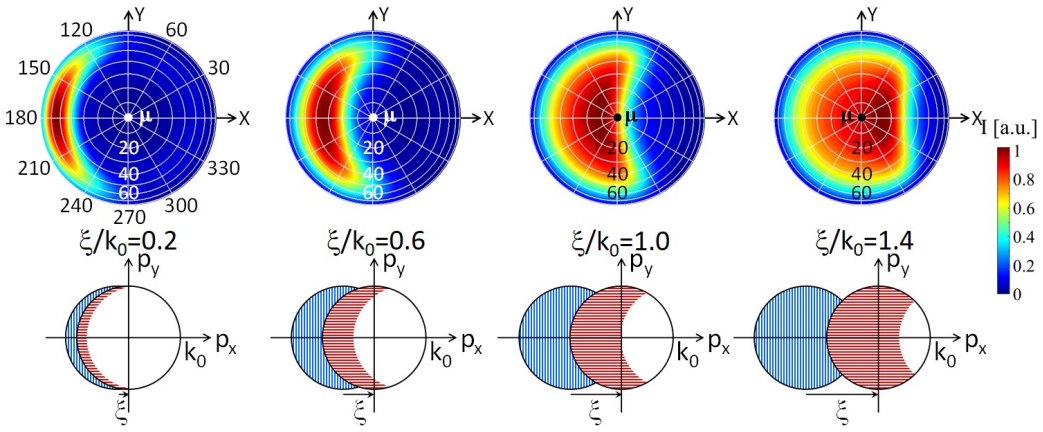


**Figure 3·4:** Simulation results showing directional far-field radiation for a z oriented dipole with GMSs of different normalized phase gradients $\frac{\xi}{k_0}$. Below each far-field radiation pattern is the corresponding reciprocal space plot predicted, as in Fig. 3·1(b).

In order to verify and quantify these expectations, rigorous simulations based on the finite difference time domain (FDTD) method were carried out. In these

simulations, the GMS is described with the HCM presented earlier, and the light source is an oscillating dipole oriented along the x,y,or z direction (as defined in Fig. 3·1(a)). All results presented below are computed at a representative visible wavelength $\lambda_0$ of 800 nm, but can be readily scaled to other wavelengths. The thickness $\delta$ of the metamaterial layer above the PEC is set to $\frac{\lambda_0}{20}$, and the imaginary permittivity and permeability $\kappa$ is taken to be 0.18. With this choice of parameters, the power reflection coefficient $R = exp\left(-4\kappa k_0 \delta\right)$ is equal to the aforementioned value of 80% measured in ref (Sun et al., 2012b) with a reflective GMS at similar visible wavelengths. Therefore,the model used in this work contains a realistic description of the GMS absorption losses. In the present context, such losses can limit the dipole radiative efficiency and cause a broadening of the radiation patterns if absorption by the GMS is stronger than diffractive scattering. The numerical simulation results presented below indicate that for $\kappa = 0.18$ these effects do not provide any significant limitation.The color maps of Fig. 3·4 show the calculated far-field radiation patterns of a dipole oriented along the z direction (i.e., perpendicular to the GMS) for different values of $\frac{\xi}{k_0}$.The dipole is located at a distance $d = \frac{\lambda_0}{100}$ from the surface and has lateral position $x = x_c$(the center of the FDTD simulation region, where the reflection phase $\Theta$ happens to be $2k_0\delta$). Highly asymmetric directional emission is clearly observed, with the angle of peak intensity rotating from the negative toward the positive $x$ direction as $\frac{\xi}{k_0}$ increases. At the same time, the angular width of the radiation pattern also increases with the phase gradient. These results are in excellent agreement with the qualitative picture presented in the previous section. The light emission appears to be dominated by the evanescent components of the dipole field that can be diffractively scattered into radiation by the GMS. As a result, the intensity distribution in the far-field pattern is mostly concentrated within the horizontally

dashed region of Fig. 3·1(b), whose width along the $p_x$ direction increases with increasing $\frac{\xi}{k_0}$. Importantly, these results could not be explained simply in terms of anomalous reflection of externally incident dipole radiation (in fact, very different patterns would be obtained in that case), which highlights the key role played by near-field interactions in the radiation process under study.

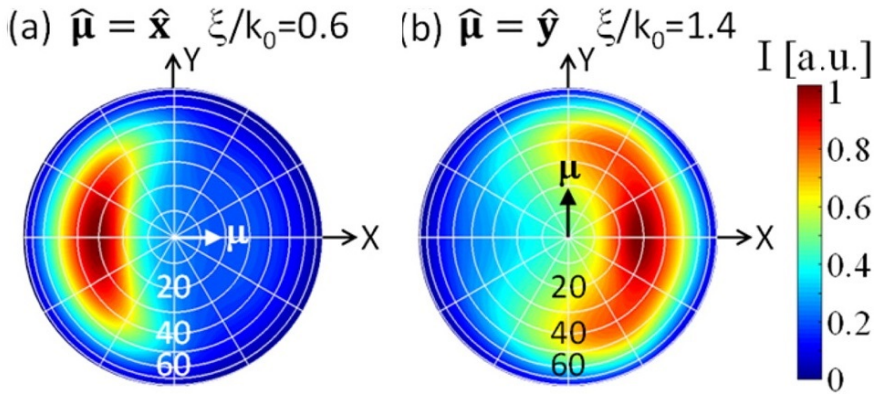


**Figure 3·5:** Simulation results showing directional far-field radiation for x and y oriented dipoles with GMSs of different normalized phase gradients $\frac{\xi}{k_0}$. Dipole orientation is denoted by $\mu$.

Similar results are obtained with a dipole at the same location oriented along the x-direction (i.e., parallel to the GMS and to the phase gradient), as illustrated in Fig. 3·5(a) for $\frac{\xi}{k_0} = 0.6$. In contrast, a y-oriented dipole at this particular location is found to produce nearly opposite radiation patterns, i.e., with stronger emission within the non-dashed region of the light circle of Fig. 3·1(b). One example is shown in Fig. 3·5(b), for $\frac{\xi}{k_0} = 1.4$ This behavior is attributed to the phase relationship between the scattered waves in the horizontally dashed region of Fig. 3·1(b) and the dipole oscillations, which in the present case appears to be inadequate to produce a large increase in emission rate. As a result, these scattered waves give a weaker contribution to the light output relative to the propagating components of $\mathbf{E}_{dip}$ and their anomalous reflection.

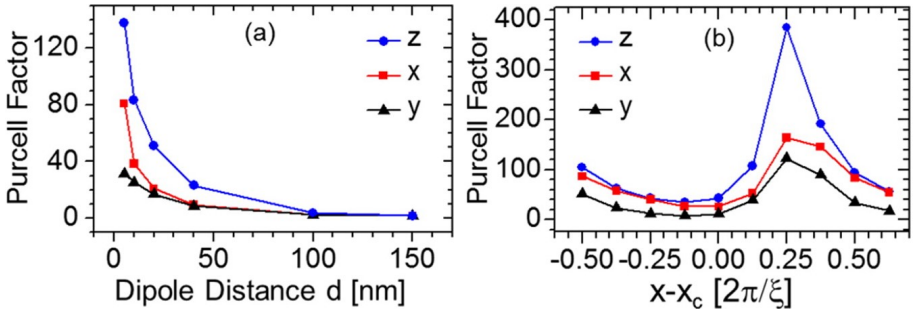


**Figure 3·6:** Purcell enhancement factor FP for all three dipole orientations versus (a) dipole distance from the GMS and (b) dipole lateral position. The GMS normalized phase gradient $\frac{\xi}{k_0}$ is 1.4 in (a) and 0.6 in (b).

Further insight is obtained by computing the equivalent Purcell enhancement factor of the GMS, defined as $FP \equiv \frac{\Gamma_{sp}}{\Gamma_{sp_0}}$, where $\Gamma_{sp}$ and $\Gamma_{sp_0}$ are the dipole emission rates near the GMS and in free space, respectively. In the FDTD simulations, FP is calculated as the ratio between the total power emitted by the dipole (into both radiative and surface waves) with and without the GMS. With this procedure, large Purcell factors of up to several 100 are obtained, indicative of strong coupling between the GMS and the emitter. For fixed GMS geometry,FP is found to depend on the dipole position in two important ways. First, it decays rapidly with increasing distanced from the GMS on a length scale well below the free-space emission wavelength $\lambda_0$, as shown in Fig. 3·6(a) for all three dipole orientations, $\frac{\xi}{k_0} = 1.4$, and $x = x_c$. This behavior is consistent with the key role played by evanescent waves in the observed spontaneous-emission rate enhancement. Second, the Purcell factor is found to vary periodically with the dipole lateral position x with period $\frac{2\pi}{\xi}$, as expected due to the aforementioned periodic x dependence of the phase difference between $\mathbf{E}_{dip}$ and $\mathbf{E}_r$. To illustrate, in Fig. 3·6(b) FP is plotted as a function of $x - x_c$ for $\frac{\xi}{k_0} = 0.6$ and $d = \frac{\lambda_0}{100}$. Similar results are predicted for GMSs of different phase gradients $\xi$, with the

lateral position of maximum Purcell enhancement depending on the specific value of $\xi$.The directional and position-dependent radiation properties just described are unique in the context of metasurface-enhanced light emission and may be exploited to enable useful new functionalities. In practice, in the case of a continuous distribution of (isotropic) dipoles near a GMS, the light output will be dominated by the regions (and dipole orientations) of highest emission rate. Under these conditions, the radiation patterns described by the basic picture of Fig. 3·1(b) are therefore obtained. On the other hand, if highly localized sources (such as single molecules or quantum dots) are employed, the GMS also allows controlling the decay rate and directionality of each emitter separately based on its location.

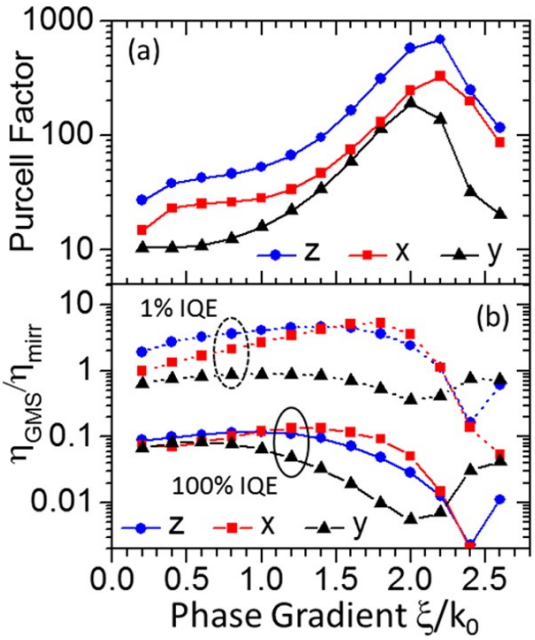


**Figure 3·7:** Purcell enhancement factor FP for $d = \frac{\lambda_0}{100}$, $x = x_c$, and all three dipole orientations, versus GMS phase gradient $\frac{\xi}{k_0}$. (b) Radiative efficiency ratio $\frac{\eta_{GMS}}{\eta_{mirr}}$ versus $\frac{\xi}{k_0}$ for a dipole with IQE of 100% (solid traces) and 1% (dashed traces).

The Purcell factor also depends on the GMS phase gradient $\frac{\xi}{k_0}$, as shown in Fig.

3·7(a) for a dipole at $d = \frac{\lambda_0}{100}$ and $x = x_c$. A pronounced peak in FP is observed near $\frac{\xi}{k_0} \approx 2$ for all three dipole orientations, which is again consistent with the qualitative picture described above. In this picture, the decay rate enhancement is largely caused by radiative scattering of the evanescent components within the vertically dashed region of Fig. 3·1(b). Therefore, FP increases with the area of this region, which in turn increases with $\frac{\xi}{k_0}$ for $\frac{\xi}{k_0} \leq 2$ (as illustrated by the two panels of Fig. 3·1(b). When $\frac{\xi}{k_0}$ is increased beyond 2,the vertically dashed region reaches its maximum possible area(equal to that of the light circle), but moves to larger and larger values of p. The resulting decrease in FP is then attributed to a progressively diminishing contribution to the probability rate of Eq. 3.1 from the evanescent components of $\mathbf{E}_{dip}$ with increasing p. A similar argument can be made regarding the $\frac{\xi}{k_0}$ dependence of the number of propagating components of $\mathbf{E}_{dip}$ scattered into surface waves, which also contribute to FP.

Next, we consider the dipole radiative efficiency $\eta = \frac{\Gamma_{rad}}{\Gamma_{sp}+\Gamma_{nr}}$, where $\Gamma_{sp}$ is the aforementioned total spontaneous emission rate (into both radiative and surface waves), $\Gamma_{rad}$ is the decay rate due to the emission of output radiative modes only, and $\Gamma_{nr}$ accounts for non radiative decay processes intrinsic to the emitter material. From the FDTD simulations we can determine $\Gamma_{sp}$ and $\Gamma_{rad}$ (normalized to $\Gamma_{sp_0}$ ), by computing the power through, respectively, a closed surface containing only the dipole and a planar surface located immediately above its nearfield. The non radiative term $\frac{\Gamma_{nr}}{\Gamma_{sp_0}}$ does not enter the FDTD calculations, but can be included in the subsequent analysis as an input parameter, related to the dipole internal quantum efficiency $IQE = \frac{\Gamma_{sp_0}}{\Gamma_{sp_0}+\Gamma_{nr}}$. With this procedure, described in more detail in section A.1, we have computed the radiative efficiency near the reflective GMSs under study ($\eta_{GMS}$) and, for comparison, that of an identical dipole above a perfect mirror ($\eta_{mirr}$). In Fig.3·7(b), the ratio$\frac{\eta_{GMS}}{\eta_{mirr}}$ is plotted versus $\frac{\xi}{k_0}$ for $d = \frac{\lambda_0}{100}$ and

$x = x_c$. The solid and dashed traces correspond to a dipole source with IQE = 100% and 1%, respectively. As illustrated by these data, the GMS can either enhance or decrease the radiative efficiency, as a result of two competing effects. First, some of the dipole emission is always captured by the GMS via scattering into surface waves. Therefore, if the dipole has a large IQE to begin with, its radiative efficiency is necessarily decreased near the GMS. Second, by virtue of the large Purcell factors just described, the probability rate of spontaneous emission can be significantly enhanced by the GMS relative to that of non radiative decay processes. As a result, in low-IQE sources the latter processes can become less of a limiting factor, leading to increased emission. As shown in Fig. 3·7(b), for IQE = 1% such Purcell enhancement effects can already overcome the optical losses in GMSs with $\frac{\xi}{k_0} \leq 2$.Thus, a sizable increase in radiative efficiency (up to over 5x) is obtained, particularly for the x- and z-oriented dipoles in this case. For the y-dipoles, $\eta_{GMS}$ is limited by the weaker contribution to $\Gamma_{sp}$ from their evanescent components at $x = x_c$, as discussed previously, but larger values can be obtained at nearby positions. Furthermore, in practice significantly larger enhancements in the collected output power can be expected for all dipole orientations,by virtue of the increased directionality produced by the GMS. Finally, for $\frac{\xi}{k_0} > 2$ all downward propagating components of the dipole field are diffracted into surface modes, and the GMS-mediated light emission involves only radiative scattering of high-p evanescent components (with progressively diminishing Purcell factor). In this regime, the radiative efficiency is therefore mostly quenched even for low-IQE dipoles, in favor of efficient excitation of surface waves at the GMS. Importantly,the latter process is also directional, with all the excited surface waves having a positive x-component of their wave vector, as a result of the asymmetric nature of diffraction by the GMS.

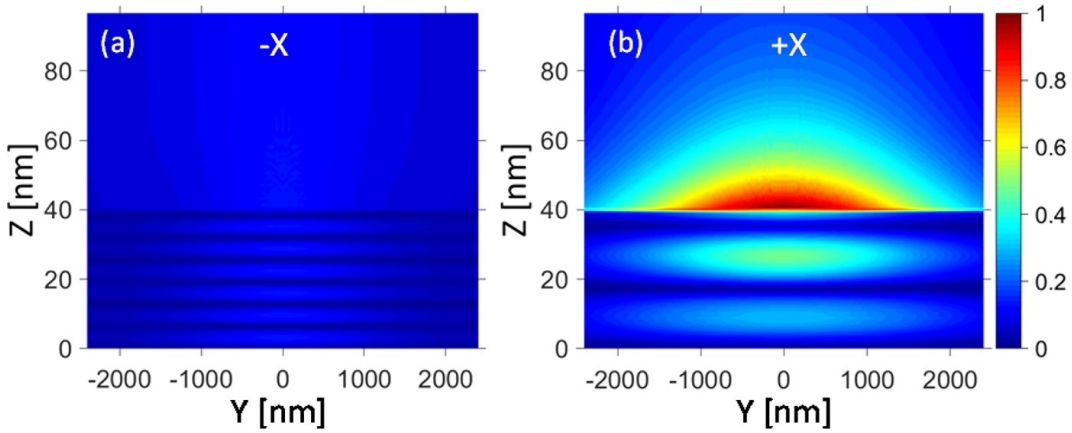


**Figure 3·8:** Optical power distribution on a monitor plane perpendicular to the x-axis near the left (a) and right (b) boundary of the FDTD simulation region, computed with a z-oriented dipole near a GMS with $\frac{\xi}{k_0} = 2.6$. The color bar is the same for both plots. The GMS–air interface is at z = 40 nm.

To illustrate, in Fig. 3·8 we show the calculated power distribution on two planes perpendicular to the GMS, located at the same distance ($\approx 3\mu m$)) from the dipole along the negative and positive x direction. In both plots, the phase gradient is $\frac{\xi}{k_0} = 2.6$, and the dipole is oriented along the z direction and positioned at $d = \frac{\lambda_0}{100}$ and $x = x_c$. A highly localized surface wave is clearly observed propagating away from the dipole along the positive x direction (Fig. 3·8(b)), while significantly less power is computed on the other side (Fig. 3·8(a)). It should be noted that such asymmetric excitation of surface waves from a nearby source is attractive for applications in nanoscale photonic integrated circuits.

### 3.1.3 Validity of the Homogenized Continuous Model

In this section we discuss the applicability of the HCM of Fig. 3·1(a) to the study of GMS-enhanced light emission. Prior experimental work (Sun et al., 2012a),(Xu et al., 2013) has shown that this model can provide an accurate description of the reflection of incident plane waves from a GMS, including the

conversion of propagating waves into evanescent waves. In the present work, however, we consider a rather different situation, where the GMS is illuminated by a dipole source located in its immediate vicinity and near-field interactions play a prominent role. To justify the use of the homogenized continuum model in this context as well, we refer to the semi-classical picture of surface-enhanced light emission embodied in Eq. 3.1 which is also supported by extensive experimental work (Barnes, 1998). In this description, the field emitted by the dipole is first decomposed in a superposition of plane waves with all possible wave vectors (including evanescent components). For each such plane wave, the light that is correspondingly reflected by the nearby surface is then calculated. The sum of all these incident and reflected waves evaluated at the dipole location determines the dipole spontaneous emission rate according to Eq. 3.1, including the effect of near-field interactions with the surface. The same sum evaluated in the far field gives the radiation pattern. Therefore, any model that can accurately describe the reflection of arbitrary plane waves by a GMS [such as the HCM of Fig. 3·1(a)] can be expected to be generally suitable to the study of light emission in the near-field vicinity of the same GMS. In practice, typical GMSs consist of planar periodic arrays of period $\frac{2\pi}{\xi}$ along the direction of the phase gradient. Each unit cell contains a finite number N of nanoantennas of different size, shape, and/or orientation, each designed to produce a different scattering phase shift across the full range between 0 and $2\pi$. The GMS phase gradient $\Theta = \Theta_0 + \xi x$ is therefore effectively discretized into a staircase with each phase step on the order of $\frac{2\pi}{N}$. Any deviation from the GMS ideal behavior that may be caused by this discretization cannot be captured by the HCM. For example, in the context of anomalous reflection this discretization can lead to the appearance of spurious orders of diffraction, which however can be rather small as shown in prior experimental

reports (e.g., down to a few % of the main reflection in the GMS of ref(Sun et al., 2012b)). In the present context, similar deviations could in principle be produced in the Purcell enhancement factors and far-field radiation patterns.

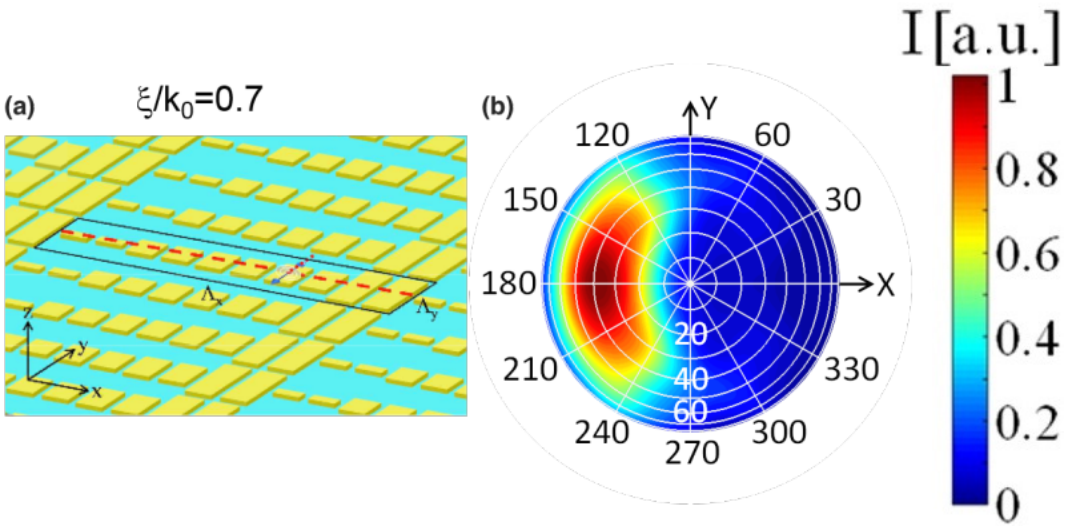


**Figure 3·9:** (a) Schematic top view of the GMS geometry under study, taken directly from the Lumerical graphical user interface. The yellow and blue regions correspond to Au and $MgF_2$,respectively. The black solid lines in (a) indicate the boundaries of a single unit cell, having dimensions $\Lambda_x$ = 1200 nm and $\Lambda_y$ = 300 nm along the x and y directions, respectively. (b) Far-field radiation pattern of the dipole shown by the double-arrow symbol in (a). The polar and azimuthal angles are indicated by the radial distance from the origin and the direction on the circle, respectively.The simulation results shown in Fig. 3·10 were computed for different dipole positions along the red dashed and dotted lines, which run across a full period along the x-direction and half a period along the y-direction, respectively, at a distance of 5 nm above the top of the nanoantennas.

To estimate the possible impact of such deviations (and in the process confirm the validity of our predictions based on the HCM), the simulation methods of the previous section have also been applied to a specific GMS design from the literature (Sun et al., 2012b). As shown in Fig. 3·9, each repeat unit of this metasurface consists of a linear array of patch nanoantennas (i.e., rectangular Au

NPs) fabricated on a sub-wavelength dielectric layer deposited over a metallic ground plane. A detailed description of the antennas size, shape, and spatial distribution can be found in ref(Sun et al., 2012b). The whole structure is designed to produce a discretized linear phase gradient across the entire $2\pi$ range (with average slope $\frac{\xi}{k_0} = 0.7$ at 850 nm wavelength), but only for y-polarized incident light. Therefore in these simulations we only consider the case of a y-oriented light emitting dipole, located at different positions on a plane at a representative sub-wavelength distance of 5 nm over the top surface of the nanoantennas. We emphasize that this structure is by no means optimized for the application under study, and was selected simply as a typical reflective GMS that has already been demonstrated experimentally. In any case, all the key predictions derived with the HCM are reproduced with this representative design. Fig. 3·9(b) shows the calculated far-field radiation pattern for the dipole position indicated by the double-arrow symbol in Fig. 3·9(a), where a substantial Purcell enhancement factor FP = 16 is also computed. As discussed in a previous section, for any dipole position (and orientation) of large Purcell factor, light emission mostly originates from scattering of the evanescent components within the vertically dashed region of Fig. 3·1(b), and as a result the far-field radiation pattern is mostly concentrated within the horizontally dashed region of the same figure. This behavior is clearly observed in Fig. 3·9(b), in full agreement with the qualitative picture of GMS-enhanced light emission presented above and with predictions based on the HCM.

In Fig. 3·10(a), the Purcell factor FP is plotted as a function of lateral position along the dashed line of Fig. 3·9(a), which runs across a full period $\Lambda_x = \frac{2\pi}{\xi}$ of the array along the x-direction. An overall peak is observed in these data, which is also consistent with the results presented above [see Fig. 3·7]. At the

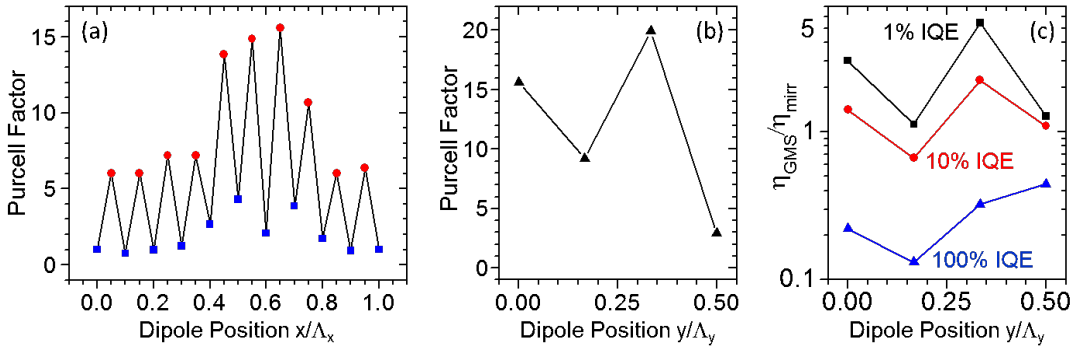


**Figure 3·10:** Purcell enhancement factor plotted as function of dipole position along the dashed (a) and dotted (b) lines of Fig. 3·9(a). (c) Radiative efficiency ratio $\frac{\eta_{GMS}}{\eta_{mirr}}$ plotted as a function of lateral y-position along the dotted line, for different values of the dipole IQE.

same time, however, Fig. 3·10(a) shows additional "higher-frequency" variations in FP versus x, with the positions above the center of each nanoantenna (red circles) consistently featuring higher Purcell factors than neighboring positions in between consecutive nanoantennas (blue squares). This behavior can be regarded as a direct consequence of the staircase phase profile of the GMS under study. The Purcell factor is also found to vary with position along the y-direction, as shown in Fig. 3·10(b) for the case of the dotted line of Fig. 3·9(a) (only half of the full period $\Lambda_y$ is considered here, given the reflection symmetry of the unit cell along the y-direction). The non-monotonic behavior observed in this plot confirms that the Purcell enhancement here does not simply originate from a near-field coupling between the dipole and its nearest nanoantenna, but rather is related to the aforementioned diffractive scattering of evanescent components by the GMS. Finally we note that, while significant Purcell enhancements are shown in Figs. 3·10(a) and 3·10(b), their values tend to be smaller than in Fig. 3·7. In addition to the discretized phase profile, this difference can be ascribed to specific

limitations of the GMS design under study. In particular, each repeat unit in this design produces a linear phase gradient across the entire $2\pi$ range only for y-polarized light. However, even with a y-oriented dipole, only a fraction of the emitted light is y-polarized, and for the remaining components the GMS under study can only produce a more limited phase gradient (and therefore a weaker enhancement). Furthermore, under ideal conditions the GMS enhancement for y-polarized light tends to be smaller compared to the x and z components, as shown in Fig. 3·7(a). Therefore, larger Purcell factors can be expected with a more focused design optimization of the GMS. Incidentally, the somewhat narrower shape of the far-field pattern of Fig. 3·9(b) along the y-direction [compared to the horizontally dashed region of Fig. 3·1(b)] can be ascribed to the same property of the specific GMS under study. In any case, even with the present structure the Purcell enhancement can be large enough to enable increasing the output power of low-efficiency emitters. This property is illustrated in Fig. 3·10(c), where we plot the efficiency ratio $\frac{\eta_{GMS}}{\eta_{mirr}}$ as a function of position along the dotted line of Fig. 3·9(a), for three different values of the dipole IQE. A maximum increase in radiative efficiency by more than 5x is obtained for the lowest IQE considered (1%).

## 3.2 Initial Experimental Demonstration of Light Beaming with a GMS

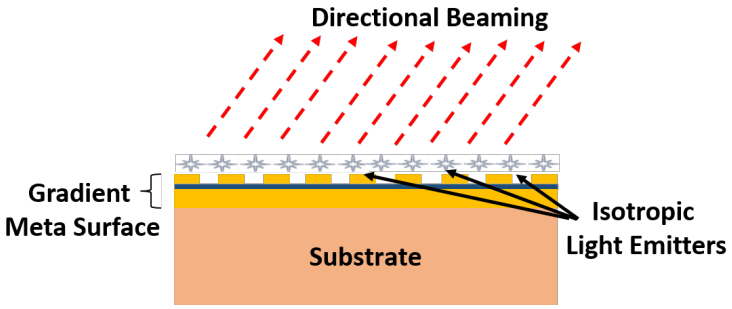


**Figure 3·11:** Figure showing the basic geometry for directional beaming. The isotropic emitters couple preferentially to SPPs supported by GMS nearby which scatters them into directional radiation.

In this section, I will describe the design and fabrication of a specific GMS implementation that can be integrated with standard isotropic light emitters to enable directional beaming. The basic geometry of this design is summarized in Fig. 3·11 where isotroic light emitters are applied directly on the GMS.

The specific GMS developed in this work consists of a periodic array of y-oriented rectangular Au (NPs [Fig. 3·12(a)] supported by an optically thick Au film with a subwavelength $SiO_2$ spacer. As shown by the FDTD simulation results of Fig. 3·12(b), the NP reflection phase (for x-polarized incident light at $\lambda_0 = 800$ nm) can be tuned over a large fraction of the entire $2\pi$ phase space by varying its width $L_x$, while at the same time maintaining a relatively high reflection amplitude > 83 %. The triangles and circles in Fig. 3·12(b) indicate, respectively, a set of three and four NP widths that produce equally spaced reflection-phase values across the full $2\pi$ range. The desired linear phase profile with gradient $\xi = \frac{2\pi}{\Lambda}$ is then implemented with the periodic repetition of two alternating unit cells of length $\Lambda$, where each cell contains the (three or four) NPs from either set placed at equal

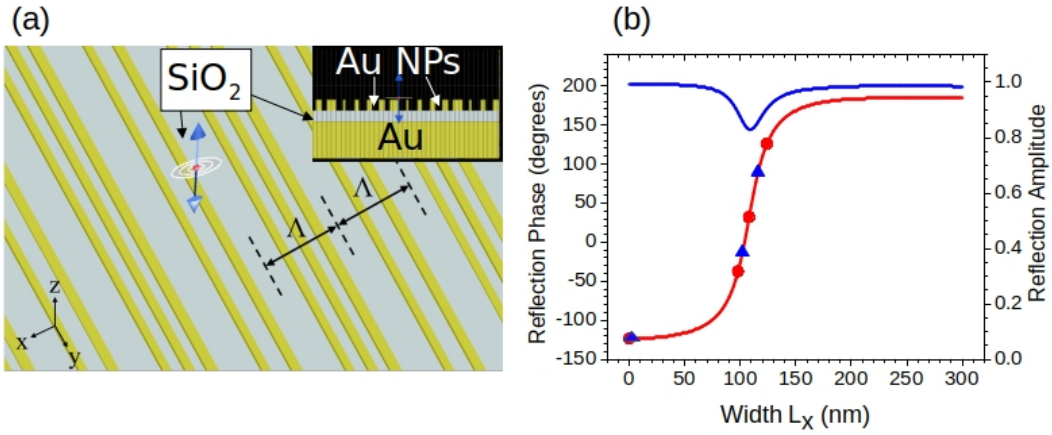


**Figure 3·12:** (a) Reflective GMS design for directional light emission. Periodic "Super Cells" made of two unit cells of period $\Lambda_{supercell}$ of 3 and 4 NPs. The inset is an x-z cross-section showing the thick Au film seperated from the NPs by a thin $SiO_2$ dielectric spacer. The NPs are effectively infinitely long in the y dimension and have a fixed height. The reflection phase is determined by the NP width. (b) Calculated reflection phase (red trace) and amplitude (blue trace) of the non-diffractive periodic array of rectangular Au NPs shown in the inset, computed as a function of NP width $L_x$ .

distance ($\frac{\Lambda}{3}$ or $\frac{\Lambda}{4}$ ) from one another [Fig. 3·12(a)]. Incidentally, both sets here include a NP of zero width (i.e., a missing NP), which is quite convenient from a fabrication standpoint. The combined use of two different unit cells increases the number of forbidden diffraction orders for the resulting GMS, as can be argued based on general sampling considerations (in the present design, all orders from q = -10 to q = +11 are suppressed except for the desired q = +1 order).

The fabrication and experimental testing was carried out by Xiaowei Wang, a Ph.D. student at the Paiella Lab at Boston University. The NP widths (w) and grating periodicity ($\Lambda$) were selected according to the general procedure described by Andlers Pors in his 2014 publication (Pors et al., 2014), briefly summarized as follows:

1. The plasmonic Bragg condition in equation 2.13 is used to calculate the grating period ($\Lambda$) for the target wavelength ($\lambda_0$).

2. The NP reflection phase vs width is calculated at a fixed height above an infinite array of identical NPs. This assumes that the mutual coupling between array elements is very small so the effect of neighboring NPs is negligible and therefore the reflection phase only depends on the NP widths and is not affected by their periodicity.

3. NPs with selected desired reflection phases are assembled into "unit cells" of a linear desired phase profile, approximated by staircase steps.

4. These "unit Cells" are then arranged with their spacing equal to the grating period ($\Lambda$).

Experimental samples based on this GMS design were fabricated on a Si substrate using electron-beam lithography [Fig. 3·13(a)], and then planarized with

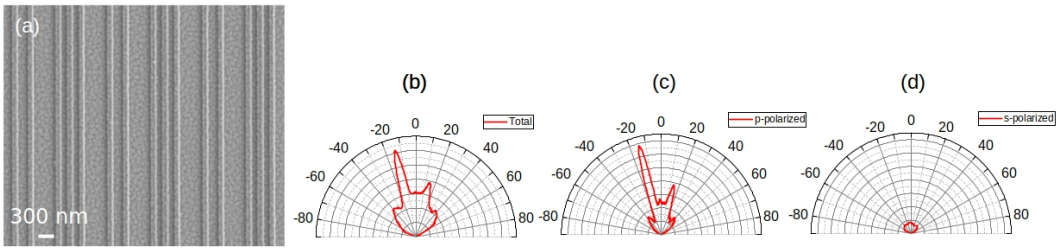


**Figure 3·13:** (a) SEM image of a GMS based on the design of Fig. 3·12 (b)-(d) Unpolarized (b), x-polarized (c), and y-polarized (d) far-field radiation patterns of a similar GMS coated with CdTe/ZnS quantum dots (QDs). In each panel, the plot shows a line cut of the radiation pattern along the x-axis. The PL signals are measured through a band pass filter centered at 800 nm.

a thin layer of spin-coated PMMA. CdTe/ZnS QDs suspended in a toluene/PLMA solution were then deposited by spin-casting, leading to a homogeneous distribution of randomly-oriented light emitters at a fixed distance of about 10 nm over the NPs. Figs. 3·13(b)-(d) illustrate the unpolarized, x-polarized, and y-polarized far-field radiation patterns measured with these samples using a Fourier microscopy setup. The key predictions described above are observed in these plots, including:

1. Highly directional emission peaked about the target angles $\theta\ max = 15°$.
2. Predominantly x-polarized radiation output (by 90% in the direction of peak emission).

A large directivity D = 14 is obtained from the x-polarized (unpolarized) pattern, with a very small divergence angle of 9° FWHM for the main beam in the line cut along the x direction [bottom plots of Figs. 2(b)-(c)]. The residual emission peak observed near $\theta = 15°$ is mostly due to deviations of the experimental NP widths from their target values which would make the GMS less efficient at suppressing unallowed beaming directions. The angle of peak emission can be tuned by simply

varying the array period $\Lambda$, and more complex radiation patterns (e.g., focused emission) could be produced with GMSs featuring more complex, nonlinear phase profiles.

# Chapter 4

# Directional Photodetection

## 4.1 Background

### 4.1.1 Motivation

In this chapter, I will describe the development of plasmonic metasurfaces that can be integrated with standard photodetectors to enable directional image sensing for artificial compound eye vision. Traditional cameras used for common imaging applications consist of a single lens projecting an image of the object of interest onto an array of photodetectors. This configuration (similar to the human eye architecture) can provide excellent spatial resolution, but suffer from a fundamental trade-off between small size and wide field of view, originating from aberration effects at large angles of incidence. In nature, the solution devised by evolution to address this issue is the compound eye [(Land and Nilsson, 2002)], which in fact is universally found among the smallest animal species such as insects and crustaceans [Fig. 4·1(a)]. While different types of compound eyes exist, their basic architecture consist of an array of many imaging elements called ommatidia pointing along different directions [Fig. 4·1(b)], each collecting a single point of information about the scene being imaged.

Typical ommatidia found in the apposition compound eye include a facet lens, a crystalline cone, a waveguiding fiber (rhabdom), and photoreceptor cells. These elements can be packed in extremely compact volumes providing full

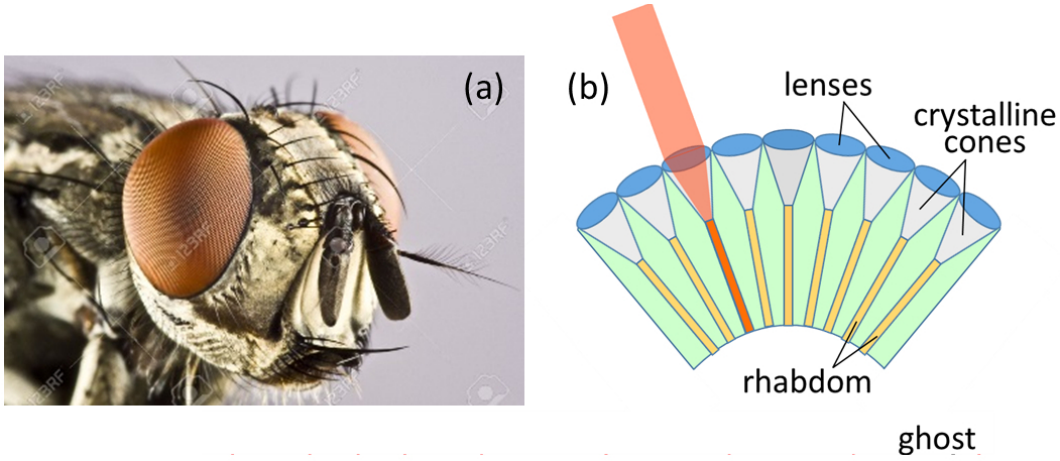


**Figure 4·1:** Compound eyes. (a) Micrograph of the compound eyes of a horse fly (from www.123rf.com). (b) Schematic illustration of the apposition compound-eye architecture.

hemispherical vision with no aberration. With this arrangement, all objects in the field of view are also automatically in focus at all times (i.e., the depth of field is essentially infinite), regardless of their distance from the camera and without the need for any focal-plane readjustment, leading to exceptional acuity to motion. As a result of these unique attributes, optoelectronic compound-eye cameras are ideally suited to address a wide range of emerging imaging applications where extreme size miniaturization, wide-angle fields of view, and high temporal resolution are of particularly importance. Specific examples include chip-on-the-tip endoscopy, concealed surveillance, wearable cameras, and machine vision for obstacle avoidance and autonomous navigation.

### 4.1.2 Prior Art

These considerations have motivated significant research efforts in the past several years on the development of novel cameras directly inspired by the compound-eye vision modality some of which are shown in Fig. 4·2. Most prior implementations have been based on planar (Tanida et al., 2001; Duparré et al., 2005) or curved

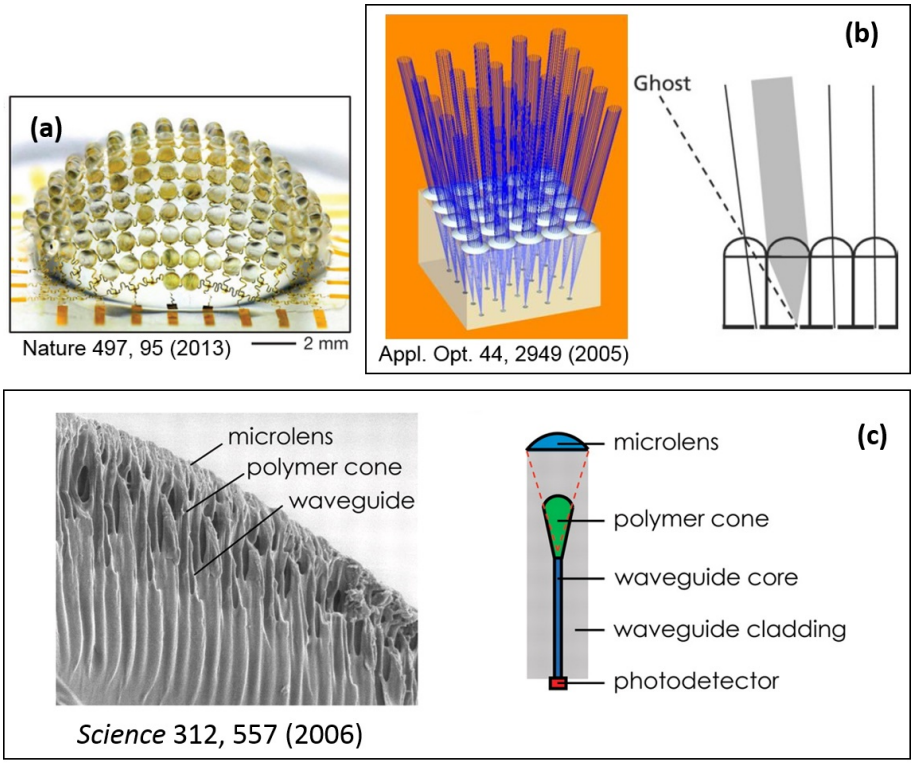


**Figure 4·2:** Prior artificial implementations of the compound eye vision modality. (a) Micro-lensed image sensors on a deformable polymer. (b) Planar array of sensors aligned to pinholes and lenses (c) Refractive polymer microlenses coupled to waveguides on a hemispherical polymer dome.

(Jeong et al., 2006; Floreano et al., 2013; Song et al., 2013; Deng et al., 2016; Shi et al., 2017; Zhang et al., 2017; Keum et al., 2018) arrays of microlenses combined with carefully aligned image-sensor arrays. The curved geometry directly mimics the compound-eye architecture of common arthropods, but is complicated by limited compatibility with standard microelectronic circuits (which are traditionally based on planar substrates). As a result, it requires either the introduction of bulky optical relay systems (Jeong et al., 2006; Deng et al., 2016; Shi et al., 2017; Keum et al., 2018), or the development of complex fabrication and packaging processes to produce photodetector arrays and readout

electronics on a curved surface (Floreano et al., 2013; Song et al., 2013; Zhang et al., 2017). A possible implementation of a flat compound-eye camera is shown in Fig. 4·2(b), where the photodetector/microlens pair in each pixel detects light incident along a different direction determined by the position of the photodetector within the focal plane of the microlens (Duparré et al., 2005). However, the field of view in this geometry is severely limited by optical crosstalk between neighboring pixels at large angles of incidence [as illustrated by the dashed line in Fig. 4·2(b)], which can lead to the formation of ghost images unless interpixel blocking layers are employed. Either way, for the smallest practical f-number of the microlenses (about 1) the maximum achievable field of view is less than ±30°. In a somewhat related technology, each photodetector is stacked with two diffraction gratings on top of one another to produce a sinusoidal dependence of detected signal on angle of incidence (Gill et al., 2011). However, the maximum reported field of view of this geometry (less than ±50°) is once again limited by fabrication constraints. Furthermore, its global architecture, where each pixel is illuminated from several different directions, is undesirable in the presence of scenes with high dynamic range in brightness. More recently, angle-sensitive photodetection has also been demonstrated with an optical phased array (Fatemi et al., 2018), which allows for dynamic tuning of the angle of peak detection but requires a local laser oscillator for heterodyne mixing.

The directional image sensors presented in this chapter are based on a fundamentally different approach [Fig. 4·3], based on the integration of a standard photodetector with a specially designed plasmonic metasurface that only allows for the detection of light incident along a small, geometrically tunable distribution of angles, whereas light incident along all other directions is reflected. With this approach, ultrathin planar lens-free cameras can be developed, featuring

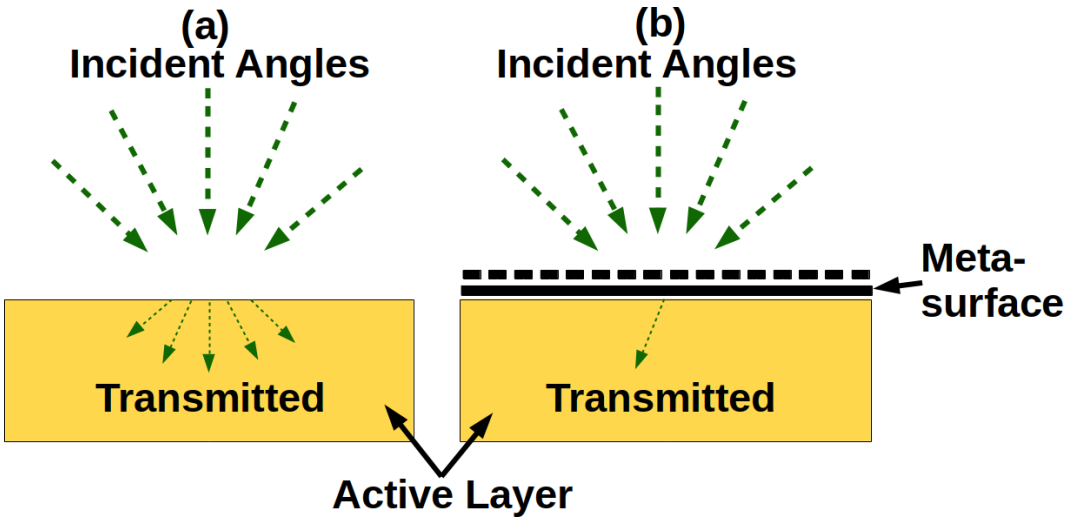


**Figure 4·3:** Principle of operation of the directional light detectors developed in this work. The plasmonic metasurface acts as a directional light filter that only allows light from a specific pre-determined angle to reach the active layer (b). In contrast a bare photodetector (a) would detect light from all directions.

all the aforementioned desirable attributes of compound eyes and providing further miniaturization compared to previous implementations. In particular, the lack of a microlens array reduces both the camera thickness and the required spacing between neighboring pixels, allowing for higher density and consequently higher resolution. The metasurfaces can be fabricated directly on existing CMOS/CCD image sensor arrays through standard lithographic techniques, with straightforward alignment and full suppression of interpixel crosstalk.

## 4.2 Metasurface Design

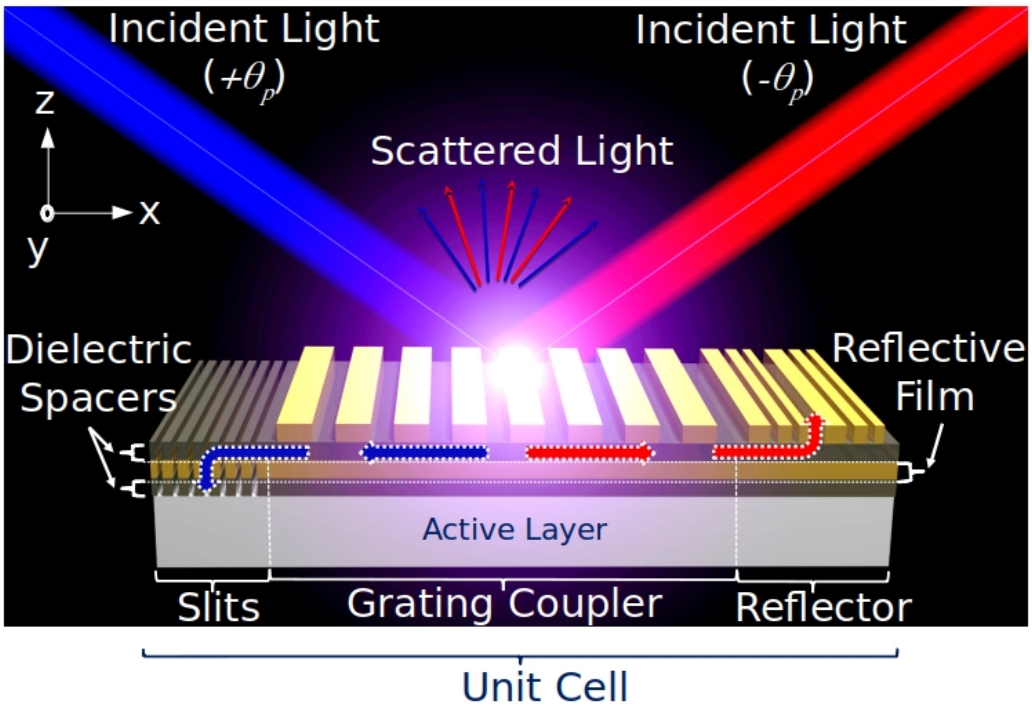


**Figure 4·4:** Schematic illustration of the angle-sensitive metasurface geometry. Light incident at the desired angle $+\theta_p$(blue beam) is diffracted by the NP array into SPPs propagating towards the slits, where they are preferentially scattered into the absorbing substrate. Light incident at the opposite angle $-\theta_p$(red beam) is diffracted by the NP array into SPPs propagating towards the grating reflector, where they are diffracted back into radiation.

The principle of operation of the angle-sensitive devices developed in this work is illustrated in Fig. 4·4. The photodetector active material (a Ge photoconductor) is coated with a metasurface consisting of a metal film stacked with a periodic array of rectangular metallic NPs. Gold is used as the choice material for all metallic features, due to its favorable plasmonic properties in the infrared spectral region (Maier, 2010). Two dielectric layers ($SiO_2$) are also introduced immediately below and above the Au film, to provide electrical insulation from the active

layer and to control the film-NP coupling, respectively. Because the metal film is optically thick (100 nm), photodetection can only take place through an indirect process where light incident at the desired angle is first diffracted by the NP array (grating coupler section) into SPPs propagating along the Au top surface. A small number of subwavelength slits in the metal film are then used to scatter these SPPs into radiation propagating predominantly into the absorbing active layer. As a result, a photocurrent signal is produced between two biased electrodes across the metasurface.

The incident angle of peak detection is determined by the NP array period $\Lambda$ and the location of the slits. Specifically, SPPs propagating along the $\pm x$ direction of Fig. 4·4(shown by red and blue arrows) can be excited via first-order diffraction of light incident (on the x-z plane) at the equal and opposite angles $\pm\theta_p$ determined by the diffraction condition $\frac{2\pi}{\lambda_0} sin(\theta_p) - \frac{2\pi}{\Lambda} = -\frac{2\pi}{\lambda_{SPP}}$, where $\lambda_0$ and $\lambda_{SPP}$ are the wavelengths of the incident light and excited SPPs, respectively. $\Lambda$ is the grating periodicity. This is the grating Bragg condition explained in more detail in section 2.2. Light incident at any other angle is instead completely reflected or diffracted away from the surface (in particular, the excitation of SPPs by all higher orders of diffraction is avoided by keeping the period $\Lambda$ smaller than $\lambda_{SPP}$). The selective detection of only one incident direction (e.g., $+\theta_p$) is then obtained by surrounding the NP array with a set of slits on one side (in the –x direction) and a grating reflector on the other side (in the +x direction). The reflector is another grating of rectangular NPs designed to scatter the incoming SPPs into light radiating away from the sample along the surface normal direction. With this arrangement, the SPPs excited by incident light at $+\theta_p$ propagate towards the slits(blue arrows in Fig. 4·4), where they are preferentially scattered into the substrate and produce a photocurrent. The SPPs excited by incident light at

$-\theta_p$ propagate towards the grating reflector(red arrows in Fig.4·4), where they are diffracted back into free space. As a result, the metasurface-coated photodetectors are functionally equivalent to the ommatidia of the apposition compound eye, enabling directional light detection while maintaining the planar geometry of standard image sensor arrays.

The metasurfaces just described rely on a number of basic ideas from plasmonics and nanophotonics, here applied to a novel device functionality. First, the ability of subwavelength slits to efficiently couple SPPs to radiation is well established in the context of extraordinary optical transmission briefly covered in section 2.4. More specifically in this case, when an SPP propagating on the top metal surface reaches the slit boundaries, a line of in-plane oscillating dipoles is effectively produced across the slit, which will then emit radiation mostly propagating into the higher-index substrate. The same behavior in reverse has also been employed for the efficient excitation of SPPs on the top surface of a perforated metal film, via illumination from the back side (Yin et al., 2004; López-Tejeira et al., 2007; Lin et al., 2013). Second, the design of the grating reflector consists of a GMS, where composite asymmetric unit cells are designed to suppress all orders of diffraction q except for q = –1.

In the geometry described here, the key concern with the grating reflector is that it not only scatters incoming SPPs into outgoing radiation along the surface normal, but also reciprocally it can couple normally incident light into SPPs. The resulting SPPs produced by q = –1 diffraction propagate along the –x direction across the entire NP array, where they can experience substantial attenuation (through absorption and scattering) before reaching the slits on the other side. Therefore, the array can be designed so that these SPPs give negligible contribution to the photocurrent. In contrast, any SPP produced by q = +1 diffraction would

propagate along the +x direction directly into the neighboring pixel in an array. As a result, the use of a linearly graded phase profile in the grating reflector is essential to avoid such interpixel crosstalk leading to spurious signals. As a result, SPP transmission (which is equivalent to zero-order diffraction) is effectively forbidden in this NP array, so that the incident SPPs from the grating coupler [as in Fig. 4·4] can be completely scattered into radiation with the smallest possible number of periods. In a photodetector array, any SPP transmitted across the reflector of one pixel may be scattered and detected into the neighboring pixel. The use of a linear phase gradient is therefore favorable to avoid spurious photocurrent signals produced by light incident at $theta_p$ [see Fig. 4·4]. Similarly, if the q = +1 order were allowed, normally incident light could be partially diffracted by the grating reflector into SPPs also propagating directly into a neighboring pixel, where again they could produce an undesired signal (in contrast, any SPP excited in the grating reflector by q = –1 diffraction will propagate along the –x direction across the entire NP array, where it can experience near complete attenuation before reaching the slits on the other side).

Several devices based on the geometry just described, each providing peak photodetection at a different angle $\theta_p$, were designed using full-wave electromagnetic simulations based on the FDTD method. Key design considerations are summarized in the following two sub-sections. The simulation methods are described in more detail in the Appendix (section A.2).

### 4.2.1 Nanoparticle Array Optimization

The geometrical parameters of the NP arrays were optimized through extensive two-dimensional simulations, where the optical transmission through the entire metasurface is computed as a function of polar angle of incidence on the x-z plane (the plane perpendicular to the long axes of the NPs) for p-polarized light. First,

the array period $\Lambda$ is selected to produce the desired angle of peak detection $\theta_p$ according to the Bragg condition (section 2.2). Next, the NP width (w) and the number of NPs in the grating coupler (N) are optimized iteratively, so as to maximize the peak metasurface transmittance at $\theta_p$ ($T_p$) while keeping the background as small as possible. Representative results produced in the course of these simulations are shown in Fig. 4·5. The optimal number of NPs (i.e., the optimal length of the grating coupler, equal to N$\Lambda$) is determined by the following tradeoff. If N is too small, an exceedingly large fraction of the sample area is occupied by the slits and grating reflector, where light incident at the desired detection angle is not preferentially coupled to SPPs that can then be scattered by the slits into the substrate. If N is too large, a large fraction of the SPPs created by incident light at $\theta_p$ (the ones produced furthest away from the slits) are absorbed in the metal film or scattered back into radiation before reaching the slits. 4·5(a) illustrates the resulting dependence of $T_p$ on N for the metasurface design with $\theta_p = 30°$; the optimal number of NPs in this device is 16.

The NP width w controls the efficiency with which the array can diffract incident light into SPPs. In this respect, the optimal choice can be expected to be around $\frac{\Lambda}{2}$, with the exact value also depending on the SPP absorption losses in the metal film. An additional important consideration is related to the spectral position of the localized surface plasmon resonances (LSPRs) supported by the individual NPs, which also depends on w. For the NP dimensions considered in this work, the fundamental (dipolar) LSPR falls in the near-infrared spectral region, as indicated by additional FDTD simulations (not shown). For our design with NPs of 50nm height, and incident wavelength of 1550nm the fundamental LSPR resonance was at a width of 300nm with higher order LSPR modes starting at widths of about 700nm. This meant that we were limited in selecting NP widths

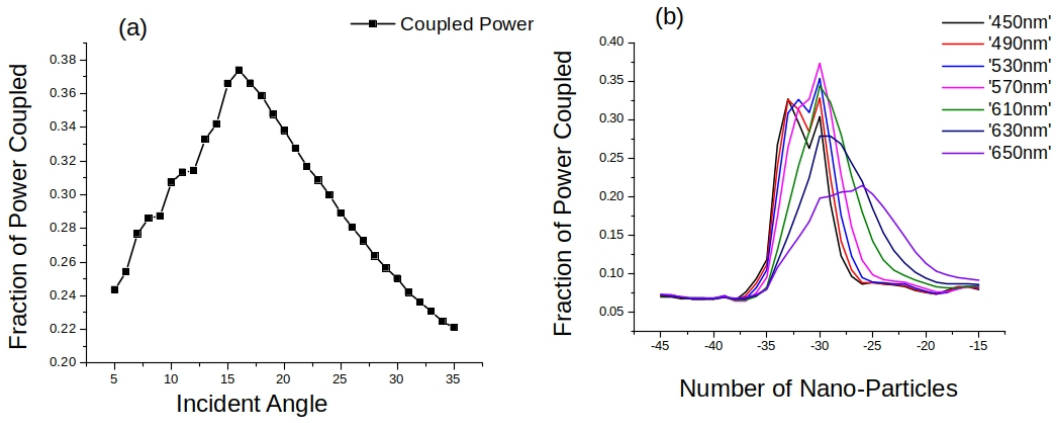


**Figure 4·5:** Design simulation results for the device providing peak detection at $\theta_p = 30°$. (a) Metasurface transmission coefficient for 1550-nm p-polarized light incident at 30° as a function of number of NPs in the same array. In both panels, all other design parameters are set equal to their optimal values presented below. (b) Angle-dependent transmission coefficient for different values of the NP width.

to widths away from these dimensions. If LSPR resonances overlap with the design wavelength $\lambda_0 = 1550nm$, the device angular response at $\lambda_0$ is affected in two ways. First, some of the incident light can be absorbed through the excitation and subsequent decay of LSPRs, causing a reduction in peak transmission $T_p$. Second, the SPP-LSPR coupling can significantly modify the SPP dispersion curve (Chu and Crozier, 2009; Ghoshal et al., 2009), leading to a change in the SPP wavelength at $\lambda_0$, and therefore a change in the angle of peak detection $\theta_p$ determined by the diffraction condition. As an additional complication, for p-polarized light incident at sufficiently large angles, the in-plane and out-of-plane components of the electric field couple to spectrally distinct SPP-LSPR mixed resonances, leading to two different values of$\theta_p$ and therefore two peaks in the device angular response (a similar behavior has been observed in reflection measurements in ref. (Ghoshal et al., 2009)). All the effects just described are illustrated in Fig. 4·5(b), where we plot the angular response of the $\theta_p = 30°$ device computed for different values of

w. The optimal NP width (in this case 570 nm for a period $\Lambda$ = 992 nm) is selected so as to maximize $T_p$ while at the same time avoiding the appearance of a second peak. By selecting optical NP widths that minimize this overlap, we were able to mostly mitigate these effects in the final optimized devices whose transmission is shown in Fig. 4·9(a). However, we can still some asymmetry resulting from this influence of LSPR resonance in the $\theta_p = 30°$ and $\theta_p = 45°$ transmission profiles, with the $\theta_p = 30°$ peak transmission $T_p$ particularly affected. It looks smaller than that of both the $\theta_p = 15°$ and $\theta_p = 45°$ devices at full optimization. For the devices whose widths do not support LSPRs ($\theta_p = 60°$ and $\theta_p = 75° devices$) their respective peaks are symmetric. We also do not see these effects in the $\lambda_0 = 800nm$ devices (Fig. 4·11) because the Au NP dimensions did not support LSPRs at this wavelength.

### 4.2.2 Grating Reflector Design

As illustrated in Fig. 4·4, the grating reflector is a periodic array of rectangular NPs designed to scatter the incoming SPPs (propagating along the +x direction) into light radiating away from the sample along the surface normal, via negative-first-order (q = –1) diffraction. Therefore, the array period $\Lambda_{gr}$ = 1524 nm is selected to match its SPP wavelength at $\lambda_0$. Additionally, as described above, its unit cells are designed so that all other orders of diffraction (including q = 0 and q = +1) are suppressed, in order to avoid interpixel crosstalk and spurious signals caused by SPPs propagating towards a neighboring pixel in a photodetector array. This goal can be achieved using a GMS geometry where the reflection phase varies linearly with position along the x direction with negative slope $\frac{-2\pi}{\Lambda_{gr}}$ (functionally equivalent to a blazed diffraction grating of period $\Lambda_{gr}$).

Specifically, we follow the approach of ref. (Pors et al., 2014), where a GMS consisting of rectangular NPs on a metal ground plane was developed to

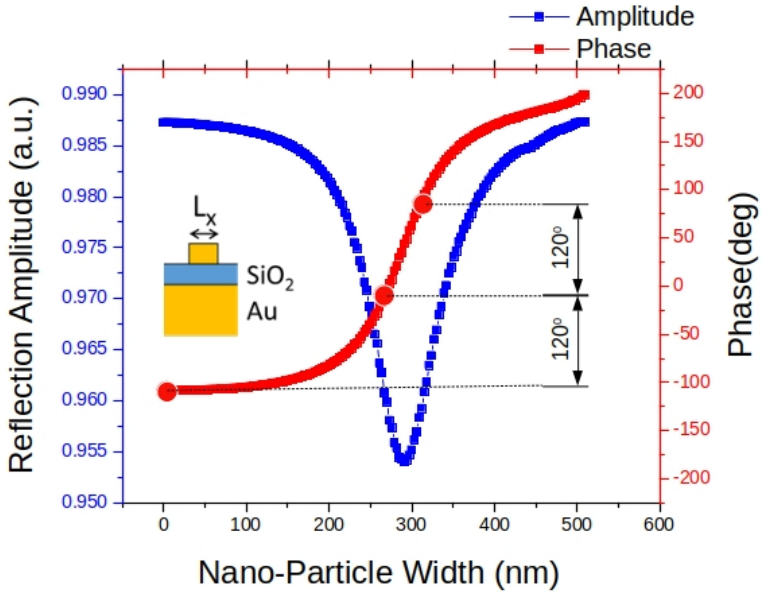


**Figure 4·6:** Reflection phase (red trace) and amplitude (blue trace) of the GMS building block shown in the inset, plotted as a function of NP width Lx for normally incident x-polarized light at $\lambda_0 = 1550nm$. Both traces were computed via FDTD simulations for a periodic (non-diffracting) array of identical NPs with 550-nm period. All layer thicknesses are the same as in the optimized structures described below. The red circles indicate three NP widths providing equally spaced reflection-phase values differing by $\frac{2\pi}{3}$.

demonstrate unidirectional excitation of SPPs by normally incident light. In this approach, a discretized version of the desired linear phase gradient is obtained by building each unit cell with a small number of different NPs, equally spaced along the x direction and providing equally spaced reflection-phase values across the full $2\pi$ range. In the geometry under study, the reflection phase of each NP can be tuned across a large fraction of the entire $2\pi$ phase space (while at the same time maintaining a high reflection amplitude > 95%) by varying its width $L_x$, as shown by the FDTD simulation results of Fig. 4·6. The dots in the same figure indicate a suitable set of 3 NP widths with equally spaced reflection-phase values differing by $\frac{2\pi}{3}$ (so as to collectively sample the full $2\pi$ range). It should

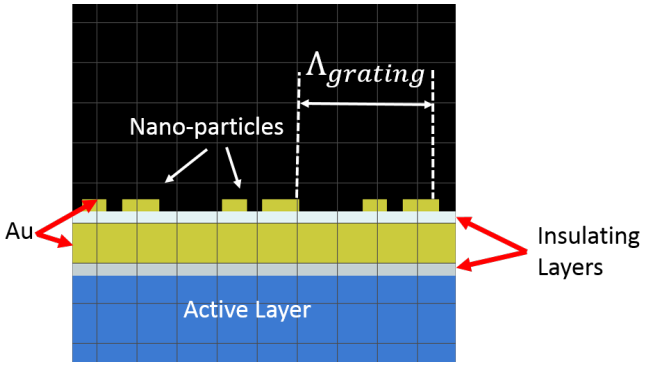


**Figure 4·7:** Schematic GMS geometry.

be noted that the narrowest NP in this set has zero width (equivalent to a missing NP), which is a particularly convenient choice from a fabrication standpoint. The desired linear phase profile with negative slope $\frac{-2\pi}{\Lambda_{gr}}$ can then be implemented with the periodic repetition of these 3 NPs, equally spaced at a distance of $\frac{\Lambda_{gr}}{3}$ and with progressively decreasing width (i.e., decreasing reflection phase) along the +x direction. A schematic of the resulting geometry is shown in Fig. 4·7.

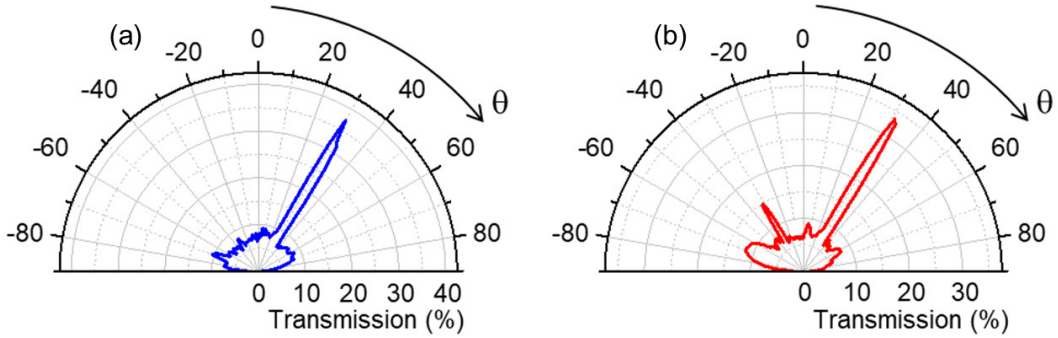


**Figure 4·8:** Calculated p-polarized transmission coefficient at $\lambda_0$ = 1550nm as a function of angle of incidence $\theta$ on the x-z plane, for two otherwise identical metasurfaces with different grating reflectors, consisting of a GMS (a) and a symmetric NP array (b).

To illustrate the effectiveness of the GMS design for our grating reflector, in Fig. 4·8 we compare two otherwise identical device structures providing peak detection at $\theta_p = 30°$ with different grating reflectors having the same periodicity

and number of reflective units. The structure of panel (a) is based on the GMS design just described. In the structure of panel (b), the GMS is replaced by a symmetric NP array having the same periodicity (1524 nm) and the same number of repeat units (5), but only one NP in each unit (with 570-nm width). The traces plotted in the figure are the p-polarized power transmission coefficients of both devices versus polar angle of incidence $\theta$ on the x-z plane. In panel (b), in addition to the large peak at the target detection angle $\theta_p$ = 30°, a smaller peak at the opposite angle -30° is also observed, caused by SPPs excited in the grating coupler and transmitted across the reflector [here, as in all 2D simulations presented in this work, we use periodic boundary conditions on the lateral boundaries of the simulation window to model multiple repetitions of the entire metasurface structure, as in the actual experimental samples; therefore, each grating reflector is immediately followed by the slits of the next repetition]. In panel (a), this additional undesired peak is almost completely suppressed through the use of a GMS reflector. This comparison clearly illustrates the improved ability of the GMS to efficiently scatter incoming SPPs into radiation, related to the suppression of zero-order diffraction (i.e., straight transmission) by its linear phase gradient.

### 4.2.3 Optimized Structures

Here we describe the geometrical parameters of the optimized device structures used in all numerical simulations presented below for devices operating at an incident wavelength $\lambda_0 = 1550nm$. Several parameters are common to all structures, selected based on initial FDTD simulations as well as practical considerations related to the available fabrication processes. In all devices both $SiO_2$ layers have a thickness of 60 nm, the metal film consists of 5 nm of Ti and 100 nm of Au, and each NP consists of 5 nm of Ti and 50 nm of Au. Each slit section contains 4 slits with 200-nm width and 400-nm center-to-center spacing.

Each grating reflector consists of 5 repeat units of 3 equally spaced NPs of different widths (340, 313, and 0 nm) with a period of 1524 nm. It should be noted here that the 313-nm width of the middle NP is somewhat larger than the value suggested by the simulation results of Fig. 4·6. It was found that this deviation produces a smaller background in the angular response, particularly for large negative angles of incidence (which could not be diffracted away from the grating reflector if all orders of diffraction except for q = –1 are strictly suppressed). Additionally, in all devices the overall length along the x direction occupied by a slit section, grating coupler, and grating reflector is an integral multiple of the array period $\Lambda$ (the smallest integer that allows accommodating all the desired building blocks). The positions of the slits and grating-reflector NPs within their respective allocated spaces was also optimized to maximize the metasurface peak transmittance $T_p$. The remaining key geometrical parameters that determine the angular response of individual devices are the array period $\Lambda$, the NP width w, and the number of NPs N. Their values were determined with the optimization procedure described above, and are listed in Table 4.1. Finally, in the device designed for peak detection at $\theta_p - 0°$ the grating reflector is absent and replaced by a slit section, since the desired angular response is symmetric.

### 4.2.4 Simulation Results

Fig. 4·9(a) shows the calculated p-polarized power transmission coefficient for the optimized metasurfaces of table 4.1 at $\lambda_0$ = 1550 nm, as a function of the polar angle of incidence $\theta$ on the x-z plane. When the metasurfaces are fabricated on a photodetector active material, the detected signal is proportional to their transmission coefficients. The devices of Fig. 4·9(a) can therefore provide tunable directional photodetection, with a wide tuning range for the angle of peak detection $\theta_p$ of ±75° and relatively narrow angular resolution, ranging from 3° to

| $\theta_p(^\circ)$ | $\Lambda$**(nm)** | **w (nm)** | **# NPs N** | **Peak Transmission ($T_p$)** |
|---|---|---|---|---|
| 0 | 1485 | 250 | 15 | 0.46 |
| 15 | 1185 | 570 | 18 | 0.40 |
| 30 | 992 | 570 | 16 | 0.37 |
| 45 | 879 | 570 | 20 | 0.38 |
| 60 | 781 | 270 | 29 | 0.38 |
| 75 | 745 | 270 | 29 | 0.36 |

**Table 4.1:** Optimized geometrical parameters for 6 designs used in numerical simulations presented in this work alongside corresponding peak transmission ratios.

14° full-width-at-half-maximum (FWHM) as $\theta_p$ is increased. The small shoulder observed in some of the peaks of 4·9(a) are related to coupling between SPPs and LSPRs supported by the NPs, as discussed above. The peak transmission coefficient $T_p$ is in the range of 35-45% for all designs considered. For s-polarized light, the transmission through the same metasurfaces is isotropic and significant smaller, less than 0.2% at all angles as seen in Fig. 4·9(b) and discussed below.

The full angular response patterns of the same devices are shown in the color maps of Fig. 4·10, where the metasurface transmission coefficients (computed with a reciprocity-based method described in section A.2.2 and summed over both polarizations) are plotted as a function of both polar $\theta$ and azimuthal $\phi$ illumination angles. In each map, the directions of high transmission form a C-shaped region within the full hemisphere, which is indicative of first-order diffraction of the incident light into SPPs of different wavevectors kSPP.

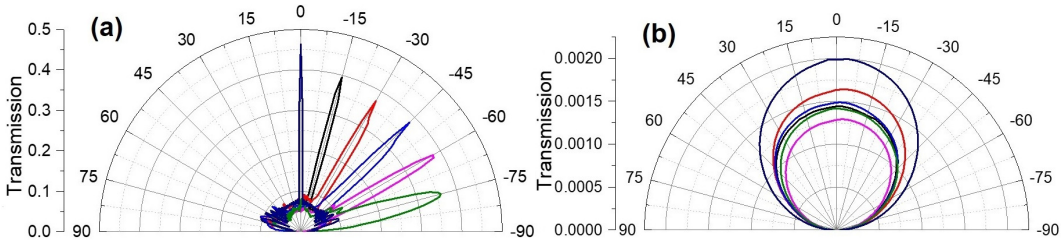


**Figure 4·9:** Power transmission coefficient at $\lambda = 1550$ nm as a function of the angle of incidence $\theta$ relative to the device normal for p-(a) and s-(b) polarized input light.

Specifically, the C-shape is determined by the reciprocal-space distribution of available SPP modes at $\lambda$ [black dotted circle in Fig. 4·10], translated by the lattice vector $\hat{x}\frac{2\pi}{\Lambda}$ of the NP array (as shown by the horizontal yellow dotted arrows in the same figure).

The observed polarization dependence of the designed metasurfaces originates from the polarization properties of SPPs. In general, SPPs possess an in-plane component of the electric field, which is parallel to their direction of propagation (Maier, 2010). Therefore, in the geometry under study, xz-polarized incident light (i.e., with electric field on the x-z plane) is most effective at exciting SPPs propagating at a small angle with respect to the x axis, and vice versa. In the same geometry, where the slits are linear and oriented along the y direction, only SPPs with a large x (i.e., perpendicular) component of the electric field can be efficiently coupled into radiation through the aforementioned excitation of oscillating dipoles across the slits (Lin et al., 2013). It follows from these considerations that the SPP modes that are more strongly scattered by the slits into the absorbing substrate are also more effectively excited by xz-polarized (as compared to yz-polarized) incident light. The same considerations also explain why the metasurface transmission within the C-shaped regions of Figs. 4·10(a)-(f) decreases with increasing azimuthal angle $\phi$ of the incident light: the larger

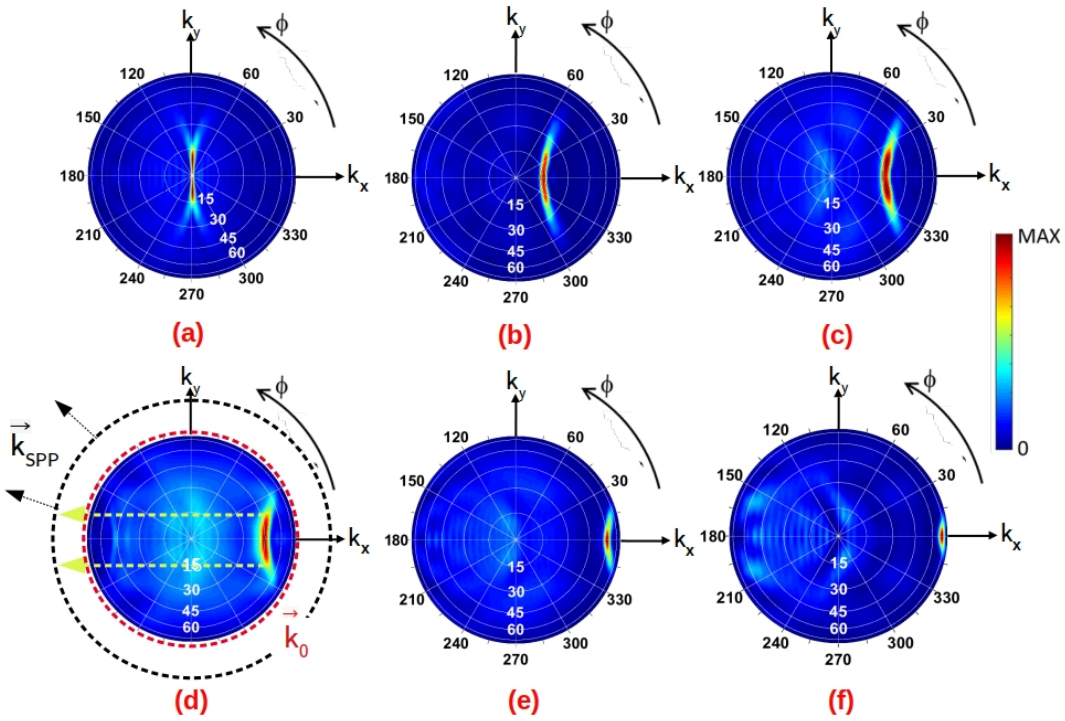


**Figure 4·10:** (a-f) Full angular response patterns of the devices shown in 4·9. These are calculated via reciprocity a method outined in appendix section A.2.2, each normalized to its peak intensity. (f) The black dotted circle indicates available SPP modes at the emission wavelength. The yellow dotted horizontal arrows indicate diffractive scattering of the incident light into SPPs (propagating along the directions of the black dotted arrows).

$\phi$, the smaller the x-components of the wavevector $k_{SPP}$ and electric field of the correspondingly excited SPPs [see black dotted arrows in Fig. 4·10]. Even though the reciprocity-based method used to calculate the device full angular response gives an accurate description of the responsivity peak, it is still an approximation which can be clearly seen in the response background. For example, in the $\theta_p = 75°$ device, we see a negligible background away from $\theta_p$ in the $\phi = 0$ plot of Fig. 4·9(a), calculated using a direct method outlined in appendix section A.2.1. However, for the simulation in Fig. 4·10(f) we can see the horizontal line-cut ($\phi = 0$) slice has much larger background. This behavior is due to the

approximations involved, as explained in detail in the appendix section A.2.2.

To demonstrate the versatility of this design with regards to the detection wavelength, we have carried out similar simulations to design structures optimized for operation at 800 nm. As shown in Fig. 4·11 we can still obtain tunable directional photodetection within a field of view of $\theta_{max} = 75°$. The peaks at 800 nm are broader than the corresponding ones at 1550 nm possibly due to increased plasmonic losses at shorter wavelengths.

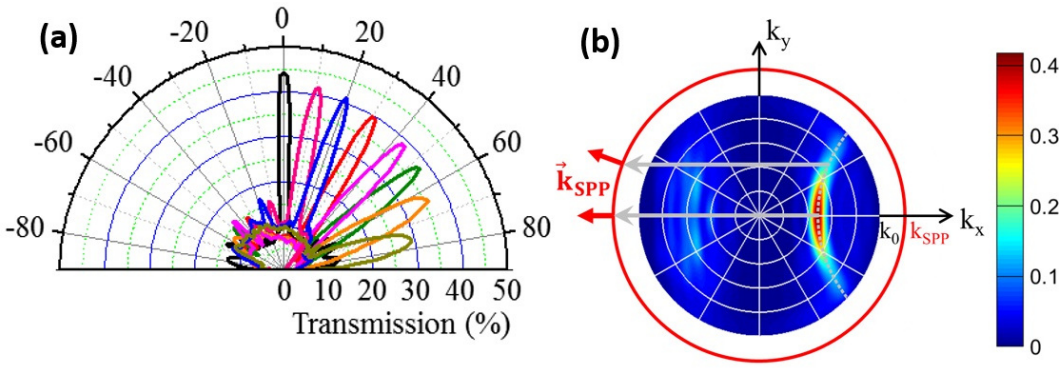


**Figure 4·11:** (a) P-polarized power transmission coefficient at $\lambda$ = 800nm versus angle of incidence $\theta$ relative to the device normal, for several different devices of varying periods of the NP array (ranging from 760 nm to 350 nm). (b) Far-field radiation pattern produced by a dipole source in the active layer of one of these devices. By reciprocity, this pattern provides an accurate description of the 3D angle-resolved transmission of the same device. The red circle indicates the available SPP modes at the emission wavelength. The grey arrows indicate diffractive scattering of the incident light into SPPs (propagating along the directions of the red arrows).

## 4.3 Experimental Demonstration

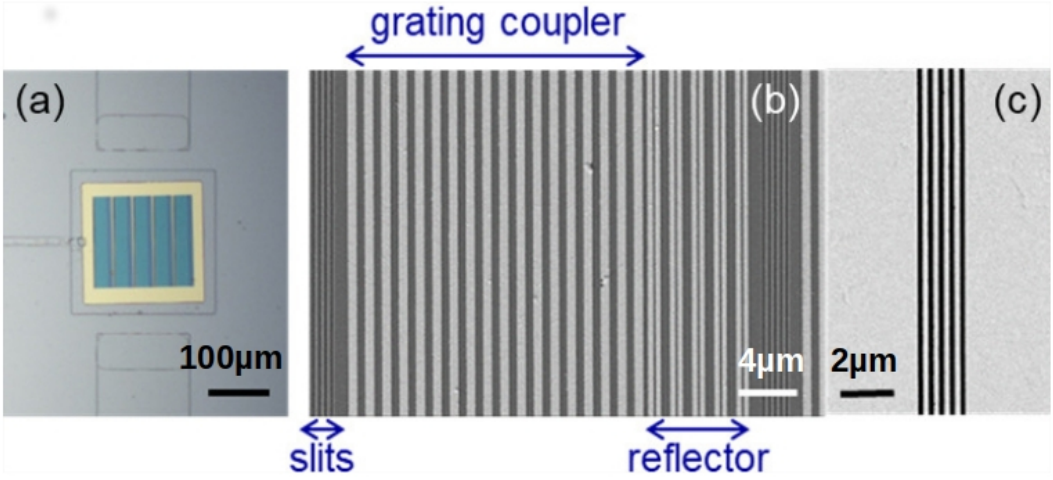


**Figure 4·12:** Optical (a) and SEM (b, c) images of representative experimental samples. The scale bar is 100 $\mu m$ in (a), 4 $\mu m$ in (b), and 2 $\mu m$ in (c). The image of (c) was taken before fabrication of the NP array.

The metasurfaces design described thus far can be applied to any planar photodetector technology regardless of its operation principles. Here we use Metal-Semiconductor-Metal (MSM) Ge photoconductors, where a photocurrent signal is collected across two biased electrodes deposited on the top surface of a Ge substrate. The angle-sensitive metasurface is patterned on the active region between the two metal contacts. While photodiodes generally offer higher performance, MSM photodetectors are particularly simple to fabricate and therefore provide a very convenient platform to investigate the metasurface development. To simplify the angle-resolved photocurrent measurements, we also use relatively large active areas: in each device, the separation between the two electrodes is $d = 200\mu m$, and the metasurface consists of a few (5-6) identical repetitions of a same structure based on the design of Fig. 4·4, with the grating reflector of one section immediately adjacent to the slits of the next section. The

Au and $SiO_2$ films are deposited by electron-beam evaporation and rf sputtering, respectively, and both slits and NPs are fabricated by electron-beam lithography with the process described below. In addition, a metallic (Ti) window is also patterned on top of each device, with an opening over the metasurface, to avoid any spurious photocurrent signal caused by light absorbed near the electrodes outside the Au film/NP-array stack. Representative optical and scanning electron microscopy (SEM) images are presented in Fig. 4·12, showing a complete device [Fig. 4·12(a)], a full metasurface section [Fig. 4·12(b)], and a set of slits [Fig. 4·12(c)].

### 4.3.1 Device Fabrication

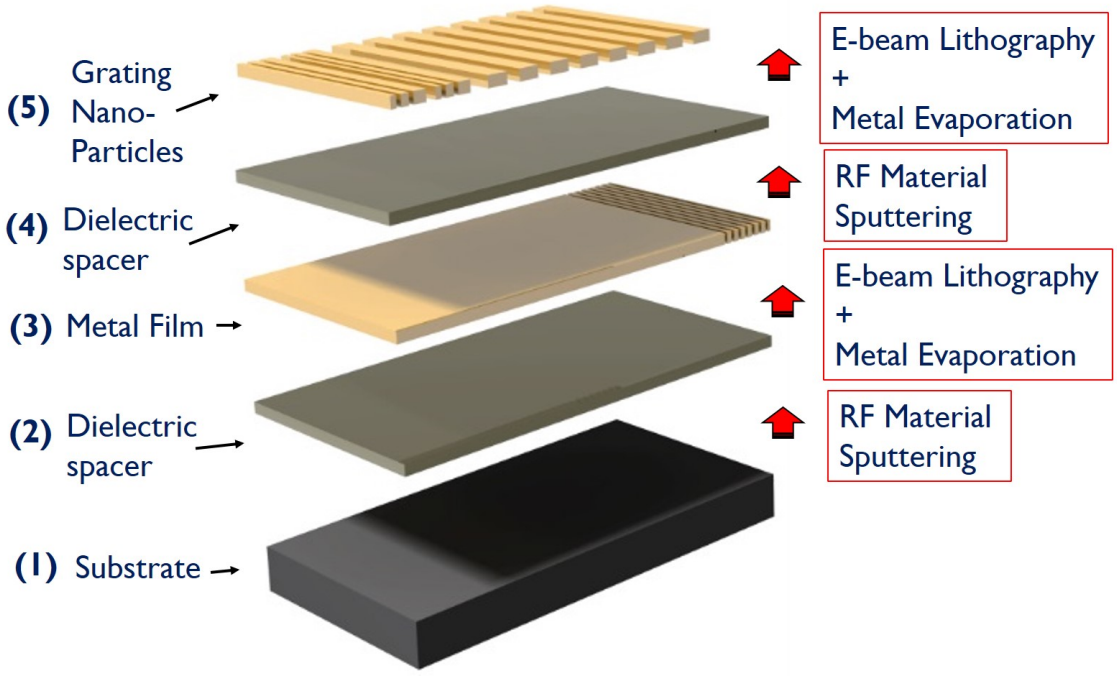


**Figure 4·13:** Figure showing the basic fabrication steps followed to make the directional detector grating numbered in sequential layers. Additional photo-lithography steps used to define E-beam alignment markers and Gold contacts for testing are not shown. Wire bonding and final packaging of the device are also not shown.

The directional photodetectors were fabricated according to the following steps summarized in Fig. 4·13.

1. Our substrate and active material is a Ge wafer with the following specifications acquired from MTI corporation:
   (a) Growth Method: CZ
   (b) Orientation: (100) +/-0.5 Deg.
   (c) Wafer Size: 4" dia x 500 microns
   (d) Surface Polishing: One side epi polished
   (e) Surface roughness: < 8 A (measured by AFM)
   (f) Doping: Not intentionally doped
   (g) Conductor type: N-type
   (h) Resistivity: >50 Ohms/cm
   (i) Package: under 1000 class clean room
2. The wafer is diced with a Disco Dad 3220 model dicing saw into 8mm x 8mm square dies, each used to fabricate one complete device.
3. Solvent cleaning according to the procedure described in appendix D.1 is performed on each square piece of the substrate.
4. Photo-lithography and corresponding metal evaporation and lift off are performed to define 10 nm thick Titanium adhesion pads providing a scaffolding for wire bonding below the Au contacts.
5. 60 nm of SiO2 are sputtered on each die to form a dielectric insulating layer according to the procedure described in appendix D.3.1.

6. Photo-lithography is performed to open windows in the $SiO_2$ layer according to the procedure described in appendix D.2.2 followed by etching in a Buffered oxide solution, opening windows to allow for the subsequently deposited gold contacts to touch the Ge substrate.

7. A 5 nm thick Ti and 100 nm thick Au backing film is evaporated, with the slits defined according to the procedure described in appendix D.2.3.

8. Photo-lithography is performed according to the procedure described in appendix D.2.2 to open an outline through which the Gold layer is etched in a Gold Etchant TFA solution from Transene, to define the grating film, light blocking pads and electrical contacts. A titanium TFTN etching solution from Transene is used to etch the 5 nm thick adhesion layer under the Gold film.

9. A 60 nm thick $SiO_2$ dielectric spacer layer is sputtered according to the procedure described in appendix D.3.1.

10. Au NPs are defined by a standard E-beam lithography/metal evaporation/acetone lift-off procedure as described in appendix D.2.3.

11. Photo-lithography is performed to open windows in the top $SiO_2$ layer according to the procedure described in appendix D.2.2, followed by etching in a Buffered oxide solution, to allow for wire bonding of the Gold contacts to electrical pads.

### 4.3.2 Experimental Setup

The directional photocurrent measurements were performed with the custom built optical goniometer setup shown in Fig. 4·14.

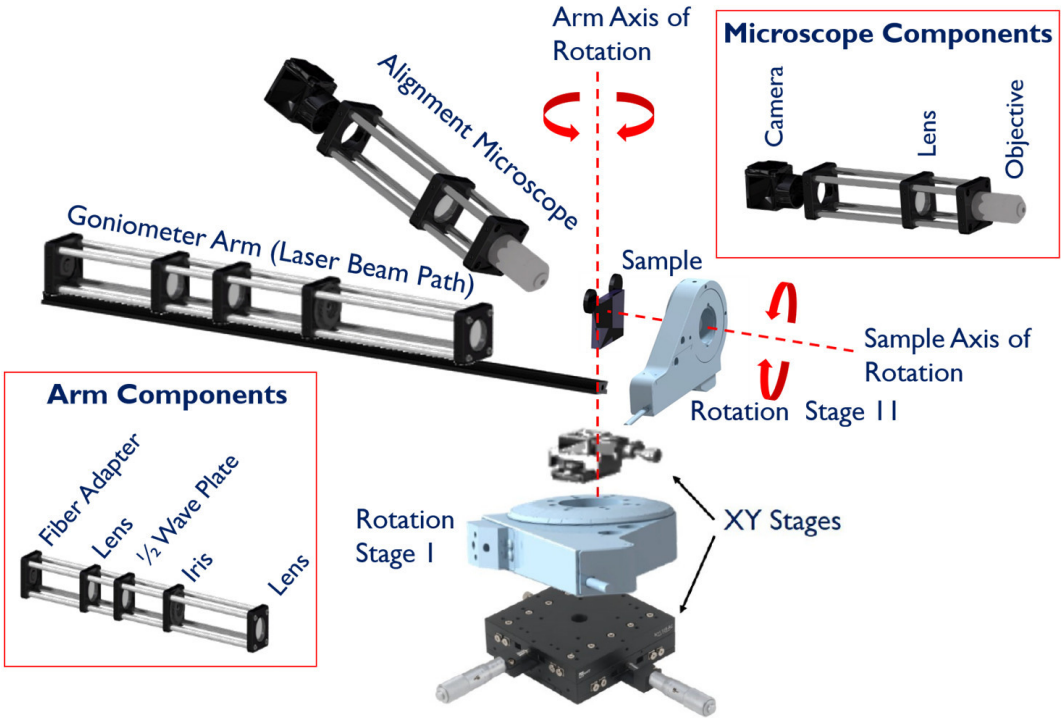


**Figure 4·14:** Schematic of the experimental setup showing major optical components. The insets show details about the composition of the goniometer arm and custom alignment microscope.

The goniometer arm consists of a Thorlabs' 30-mm cage system on which a two-lens 2x beam expander (made of two lenses with 10mm and 5mm focal-lengths and 1" diameter) was mounted. On one end of the arm, a polarization maintaining optical fiber from an Agilent 8164A polarized diode laser system (with output power on the order of 1mW) is connected through a fiber adapter. The beam is expanded and weakly focused on the sample at the other end. In addition to the beam expanding lenses, the arm also contains a half-wave plate for beam polarization control and an adjustable iris to control the focused spot size. The goniometer arm is located on an xyz translation stage mounted on a piezo-controlled rotational stage on another xyz translation stage. The center of rotation of the rotation stage is placed close to the focal point of the beam expander and the double translation stages are used to align the beam, placing the focus point right on the rotation axis so that movement of the beam across $\pm 85^0$ still maintains this arrangement. An angled custom microscope setup connected to a USB camera with an objective and lens mounted on a similar cage system is used to help align the laser beam on the sample. The sample connected to electrical leads was then mounted on another xyz translation stage as well as a second rotation stage used to vary the azimuthal illumination angle.

The leads from the sample were connected to an SR860 lock-in-amplifier through a custom built bias-T.During photocurrent measurements, the device under study is biased with a DC voltage while the incident light intensity is modulated at 1kHz. The bias-T and lock-in amplifier then enable extraction of the photocurrent, separate it from the dark current. The rotation stage and lock-in-amplifier are both controlled by custom LABView software for data acquisition.

**Alignment**

Since our beam at a wavelength of 1550 nm is invisible to the naked eye, we applied a three step process for aligning it to our sample. First we align the beam axis to a point on an IR card centered in the cross hair of the alignment microscope. Next, we move the IR card to the beam of rotation of the goniometer arm, and adjust the beam focal point, moving it to the new IR card position. Finally, we replace the IR viewing card with the actual sample and move the grating to the center of the cross hair of the alignment microscope without altering any of the already aligned parts. In this way we effectively place the grating in the beam focus point and center of rotation.

**Step 1: Aligning the beam axis to the goniometer rotation axis**

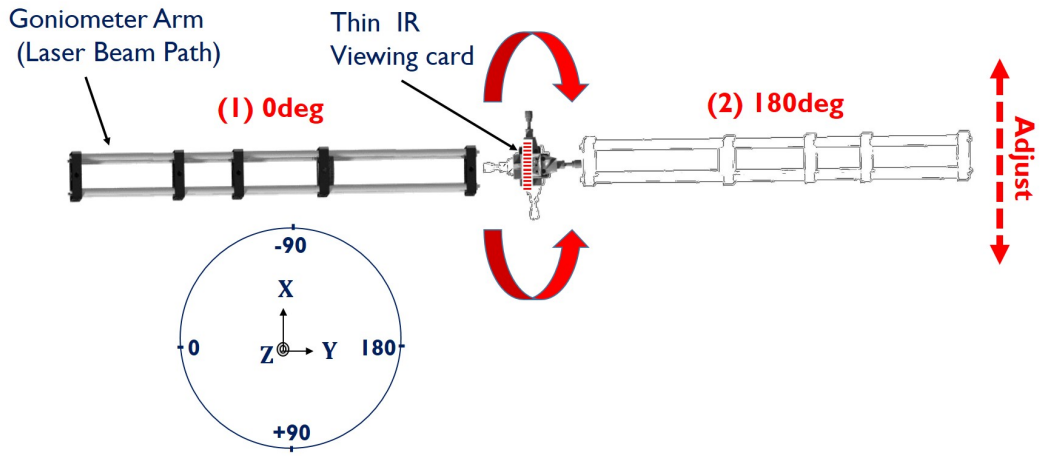


**Figure 4·15:** Iterative process for aligning the laser beam axis to the goniometer rotation axis.

1. A thin IR viewing card is placed perpendicularly in the beam path right at the focal point, while the goniometer arm is at the $0^0$ position.
2. The microscope is focused on the beam spot on the IR card and this is

centered in the corresponding camera image cross-hair.

3. The goniometer arm is rotated by $180^0$ and the x-axis on the stage is adjusted to center the beam spot again in the cross-hair as the beam hits the IR card from the back. It is important that the microscope position is not altered in any way so as to act as a reference.
4. Steps (b) and (c) are repeated iteratively as shown schematically in Fig. 4·15 until the beam is centered in the microscope cross-hair at both $0^0$ and $180^0$.

**Step 2: Locating the goniometer center of rotation and shifting the beam focus to this point.**

1. The goniometer arm is rotated iteratively through $\pm 88^0$ as the IR card is moved along the y-axis until the beam spot lateral position within the microscope cross hair does not change with the arm angular position.
2. The goniometer is then moved in the radial direction relative to the rotation stage until the beam is once again focused to the IR card at its new position. Similar to before, the microscope position is not altered in any way so as to act as a reference.
3. Steps (a) and (b) are repeated iteratively as shown schematically in Fig. 4·16 until the beam is centered and focused in the microscope cross-hair at both $\pm 88^0$ .

**Step 3: Placing the sample at the beam center of rotation and focus**

The IR card is then replaced with the sample, positioned to ensure that the grating is focused and centered in the microscope cross-hair. This is done by

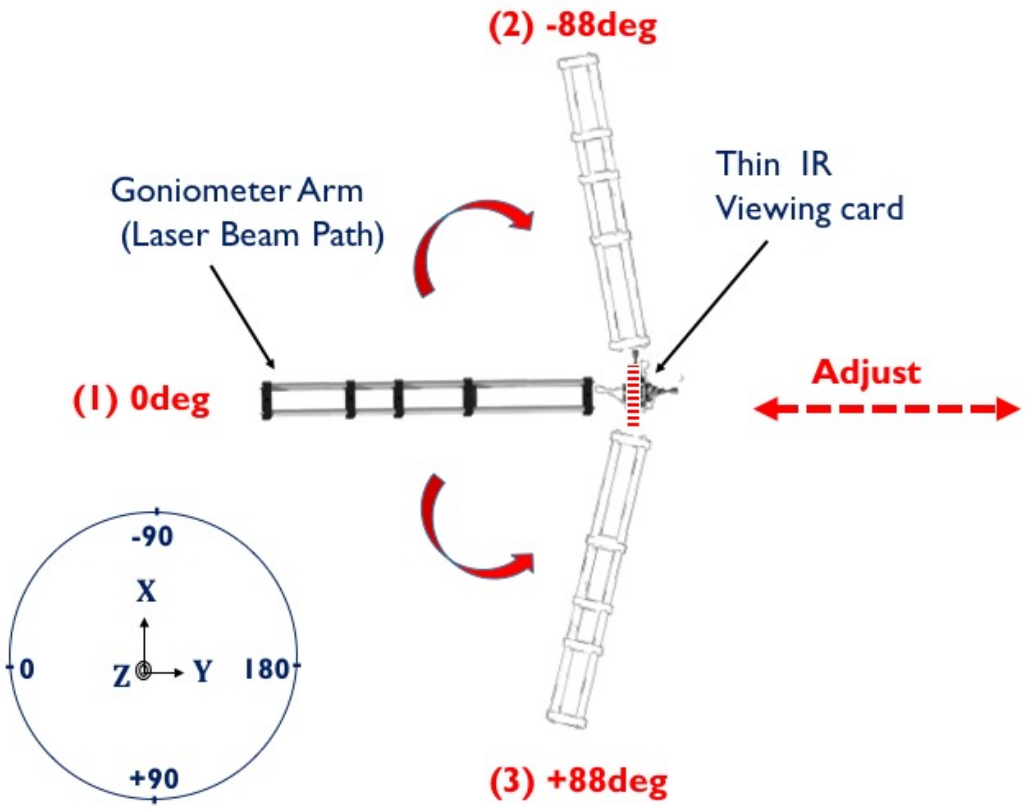


**Figure 4·16:** Iterative process for locating the goniometer center of rotation and moving the beam focus to this point.

only moving the sample and not altering the goniometer arm and microscope positions or alignments in any way.

**Data Acquisition**

With the beam aligned and the sample placed in its focal point and also at the center of rotation, the goniometer is then rotated through $\pm 85^0$ with the corresponding photo-current recorded at each angle. This is done using custom made LABView software that iteratively moves the rotation stage through all required angles and records the measured current from the Lock-in-Amplifier. For each device this procedure is repeated for two orthogonal input polarizations, perpendicular(xz) and parralel(yz) to the grating lines, for different azimuthal illumination angles.

### 4.3.3 Measurement Results

The angle-resolved photocurrent measurement results show highly directional response in good agreement with simulations. A complete set of experimental results for a device providing peak photodetection near $\theta_p = 30°$ is presented in Fig. 4·17. Specifically, panels (a) and (b) in this figure show the measured xz- and yz-polarized responsivity maps, respectively, plotted with the same color scale. Their sum is displayed in panel (c). These maps were obtained by varying the polar illumination angle $\theta$ in steps of 1° between ±85°, whereas the measured azimuthal angles $\phi$ range from 0° to 90° in steps of 5°. The remaining two quadrants of the angle-dependent responsivity maps are then filled up based on the mirror symmetry of the device geometry under study with respect to the x-z plane. To produce smoother plots, a linear interpolation procedure is then used to include additional data points between the measured values in steps of

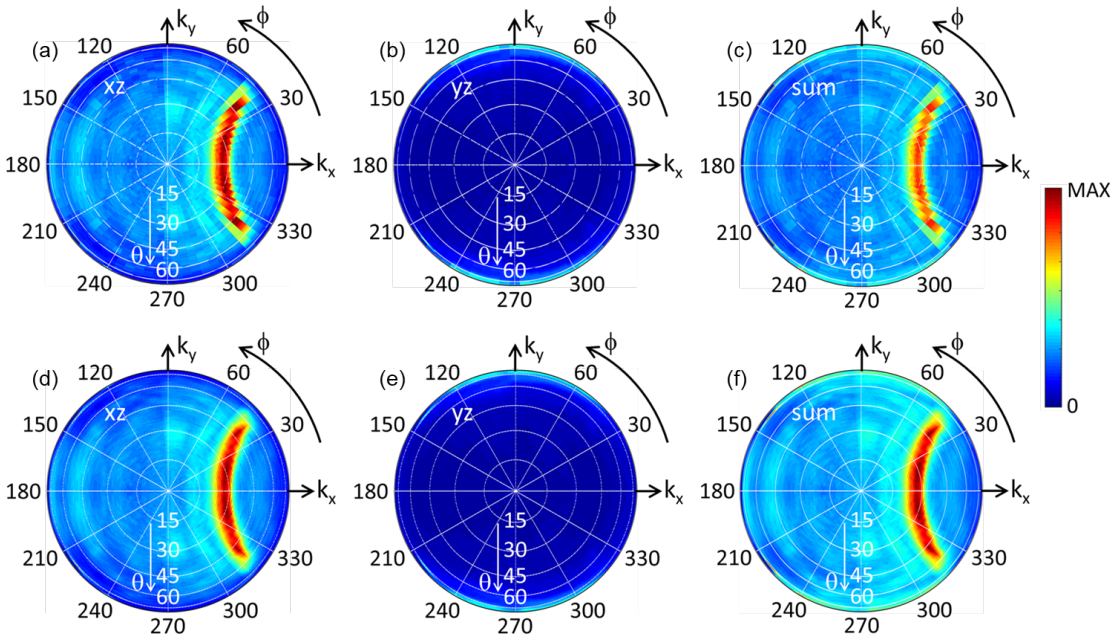


**Figure 4·17:** Complete set of experimental results for a device providing peak response near $\theta_p = 30°$. (a), (b), (c) Measured xz- and yz-polarized maps, and their sum. (d), (e), (f) Same as (a), (b), (c), respectively, including the interpolated values. The measured values of the grating-coupler period and NP width in this device are $\Lambda = 1030$ nm and w = 526 nm, respectively.

1° in $\phi$. Panels (d)-(f) of Fig. 3.31 show the same maps of panels (a)-(c) plotted including these interpolated values. Consistent with the discussion above, the strongest photocurrent signal is obtained when the incident light is xz-polarized, whereas the yz-polarized contribution is essentially negligible. The expected C-shaped region of high responsivity is also clearly observed in this figure, centered near the design polar angle of maximum metasurface transmission $\theta_p = 30°$.

Similar results are obtained with several other devices designed for peak detection at different angles. A collection of measured responsivity maps, summed over both polarizations and including the interpolated values, is presented in Figs. 4·18(a)-(e). Panels (f)-(j) of the same figure show the horizontal line cut of each map (i.e., the measurement results for $\phi = 0$). The overall performance of these devices is in good agreement with simulation predictions. We notice however that the directional sensitivity C-shape in the measurement data is longer (i.e. extends to larger $\phi$ angles in the polar plot) than those predicted by the dipole reciprocity simulations shown in Fig. 4·10. This is possibly due to the fact that the dipole field radiation pattern has less intensity in radiation traveling at high angles relative to the normal compared to radiation at smaller angles thus artificially penalizing high $\phi$ components of its the far field projection. However, we are still able to get an accurate general shape. Tunable directional photodetection is demonstrated, with polar-angle selectivity (FWHM) along the horizontal line cut on the order of 10° or less. The peak-to-average-background ratio varies between 2 and 3, which is somewhat smaller than the theoretical values [about 4 – see Fig. 4·18(a)]. This difference is mostly attributed to the presence of some roughness in the metal films of the experimental samples, which can scatter some of the incident light into SPPs regardless of its direction of propagation. In any case, as discussed below, these measured device characteristics are already adequate for high-quality image

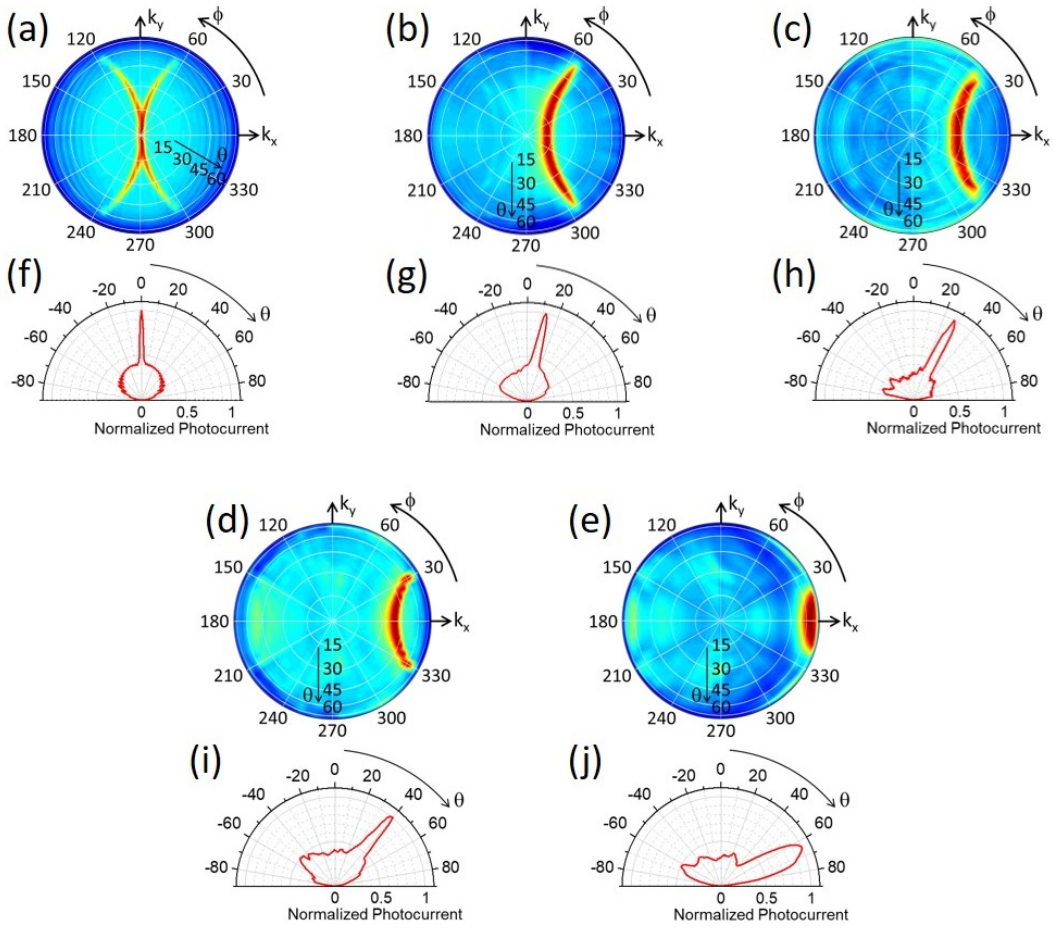


**Figure 4·18:** (a)–(e) Measured angular dependence of the photocurrent of five devices providing peak response near $\theta = 0°$ (a), 15° (b), 30° (c), 40° (d), and 65° (e). SEM images reveal some deviations in the array periods and NP widths from their target design values. The measured values are $\Lambda$ = 1441, 1141, 1030, 901, and 733 nm and w = 240, 581, 526, 507, and 318 nm for the devices of panels (a), (b), (c), (d), and (e), respectively. The map of (c) is the same as Fig. 4·17(f). (f)–(j) Line scans along the $\phi = 0$ direction from the maps of (a)–(e), respectively.

reconstruction.

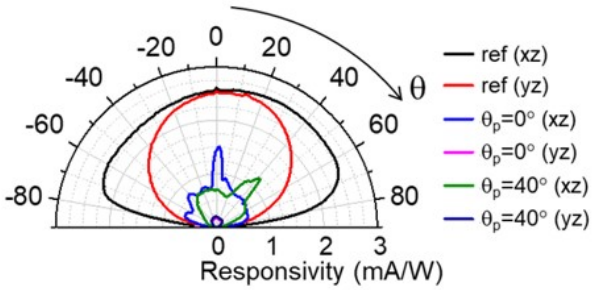


**Figure 4·19:** p- (i.e., xz-) and s- (i.e., yz-) polarized responsivity versus polar angle of incidence on the x-z plane, measured with three different samples: a reference device without any metal film and NP array, and two metasurface-coated devices providing peak detection at $\theta_p = 0°$ and $\theta_p = 40°$, respectively.

Finally in order to evaluate the peak transmission of the metasurfaces at their target detection angles, otherwise identical "bare" samples without any metal film and NP array between the two electrodes were also fabricated and tested. These reference devices exhibit a rather low normal-incidence responsivity of a few mA/W, limited by the low bias voltage V (on the order of 1V) used in the measurements and the large inter-electrode separation d=100 $\mu$m (since the photoconductive gain is proportional to $\frac{V}{d^2}$ (Chuang, 2009)). The peak responsivity of the metasurface devices was generally found to be smaller but of comparable order of magnitude. Unfortunately, a detailed quantitative comparison among all experimental devices was prevented by large variations in dark resistance observed among samples based on the same design (even among bare samples), with the peak responsivity consistently increasing with dark resistance, possibly due to fabrication-induced defects affecting the carrier density. Fig. 4·19 shows angle-resolved data measured with three samples (bare, $\theta_p = 0°$ and $\theta_p = 40°$) featuring the same dark resistance ($2k\Omega$). At their respective angles of peak detection of 0° and 40°, the p-polarized responsivities of the two metasurface

devices in this plot are reduced by a factor of 1.7 and 2.1, respectively, compared to the bare sample, in reasonable agreement with the simulation results of Fig. 4·9(a).

### 4.3.4 Simulated Image Reconstruction

In the following section, we present the design of a compound eye camera based on the infrared devices just described. The basic imaging unit (ommatidium) of this camera simply consists of one such directional photodetector without any lens or any other optical element. We also present a specific computational imaging algorithm that we apply to reconstruct images captured with this architecture. The key conclusion is that with this approach high-quality images of relatively complex objects can be reconstructed, even with a reasonably small number of pixels (1800 or less).

Our proposed cameras consist of a pixel array (shown in Fig. 4·20(a)), with each device providing directional photodetection peaked at a different combination of polar and azimuthal angles ($\theta_p$ and $\phi_p$, respectively). The value of $\theta_p$ is controlled by varying the grating coupler periodicity according to the Bragg condition(equation 2.13). For a fixed design, $\phi_p$ is varied by simply rotating the entire metasurface about its surface normal on the corresponding photodetector. Using this pixel arrangement, we have conducted a series of numerical simulations based on the computational imaging technique introduced in section 2.5. We consider objects far away from the pixel array within a total field of view of ±75°, so that each angle corresponds uniquely to a different spatial point on the object [Fig. 4·20(b)]. Each pixel integrates the total intensity detected according to its angular response. The image-formation process can then be described by a linear equation, which relates the object intensity distribution (x) to the captured data (y) by a measurement matrix (A) [Fig. 4·20(c)]. The angular response of each pixel

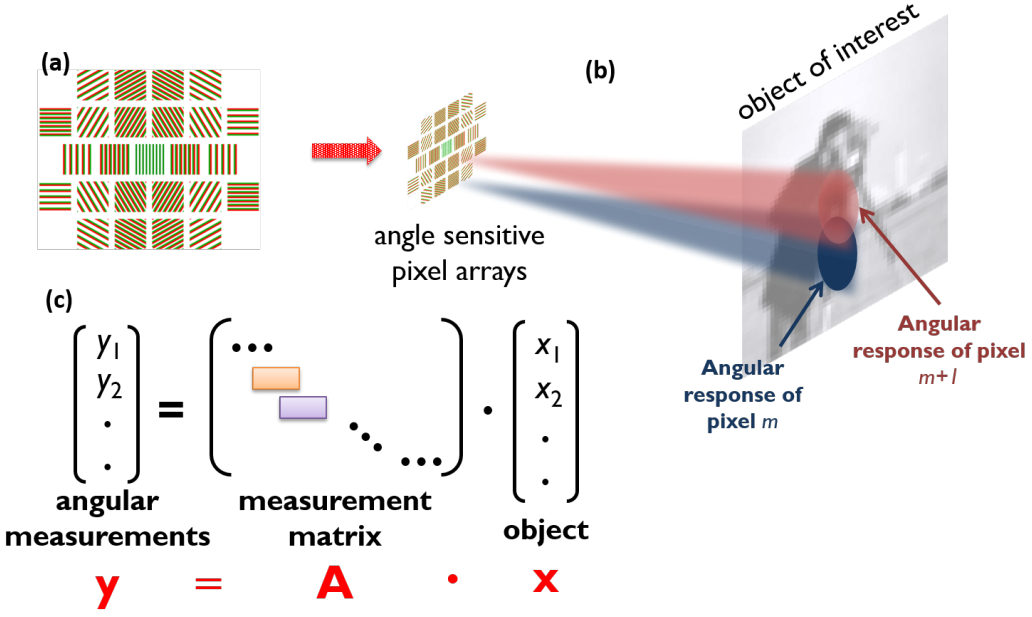


**Figure 4·20:** Schematic of image acquisition and reconstruction process. (a) Pixel arrangement: Each radial line of pixels covers the full $+\theta$ range and is rotated over the full $\phi$ range. (b) Schematic of image acquisition: Each pixel integrates the incident light intensity from a range of directions corresponding to different parts of the object as determined by its angular response. (c) Computational imaging algorithm where the measurement matrix containing all the pixel information connects the measured pixel readings (angular measurements) to the object.

forms a different row vector of A, which quantifies the intensity contributions to the pixel from different points on the objects.

With this approach, we have validated the ability of our directional photodetectors to enable complex image reconstruction. To that purpose, the individual pixels in the array are described by the calculated angular response maps [as in Fig. 4·10], together with their interpolations for additional metasurface designs providing peaked transmission at different polar angles. These simulations were carried out by Prof. Lei Tian at Boston University and his Ph.D. student Yunzhe Li. Figure 4·21(a) and 4·21(b),(c) show, respectively,

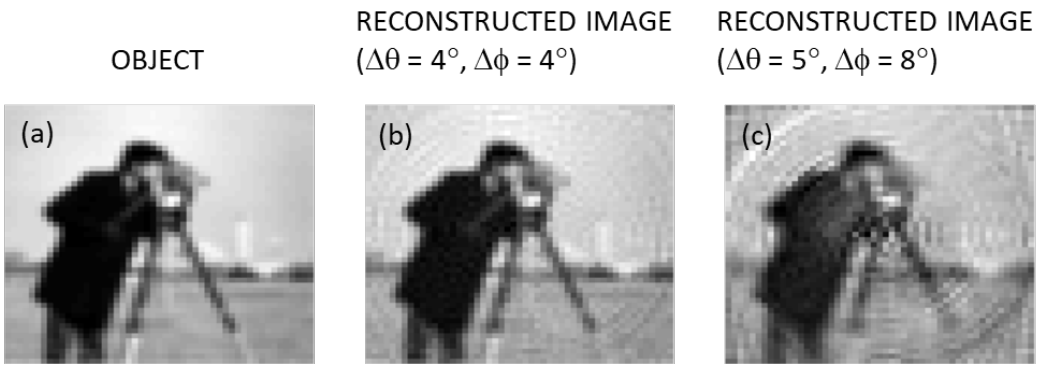


**Figure 4·21:** (a) Object used in the image reconstruction simulations. (b), (c) Reconstructed images for an array of pixels covering a wide field of view of ±75° with 1800 (b) and 720 (c) pixels, under monochromatic illumination. The measurement matrix A used in these simulations is based on the calculated response functions of the devices of Fig. 4·11, designed for operation at 800 nm.

the original object used in the calculations and examples of reconstructed images under monochromatic illumination at the design wavelength. The angular spacings between neighboring pixels in the array are $\Delta\theta_p = \Delta\phi_p = 4°$in panel (b) and $\Delta\theta_p = 5° and \Delta\phi_p = 8°$ in panel (c), corresponding to a total of 1800 and 720 pixels. Well recognizable images are obtained in both cases, with the reconstruction quality increasing with decreasing angular spacing as expected. These results clearly support the promise of our devices for the development of a novel camera technology featuring the unique attributes of the compound eye (including small size, wide field of view, and high temporal bandwidth resulting from infinite depth of field). Additional simulations by Yunzhe Li are ongoing to evaluate image reconstruction with the same camera architecture under different illumination conditions (including broadband incident light), as well as based on the experimentally measured response maps.

# Chapter 5

# Conclusion

## 5.1 Future Outlook

### 5.1.1 All Optical Image Recognition

As we have seen with the directional light detectors, it is possible to design a metasurface to selectively couple light of a specific phase profile to SPPs which can then be detected. A symmetric plasmonic grating combined with slits enables detection of two symmetric incident angles of plane waves. Replacing the symmetric grating with a GMS and/or adding a reflector region, we can obtain single-peak detection as demonstrated in our directional-detector work. We envision that with increased complexity, we could design metasurfaces for the detection of not just an incident plane wave at a specific angle but also more complex phase profiles, such as resulting from light reflected off a specific object or transmitted through an aperture. This can be achieved by designing a GMS grating whose transmission or reflection phase profile is inverse to that of the target incident light at the position of the detector, so as to allow phase matching to SPPs upon diffraction. This incident light could have a complex phase profile, for example related to a distant scattering object, for which the GMS could be appropriately designed. By detecting the resulting SPPs, we can then detect the presence of our target object. This arrangement would be very desirable since there would be no computation involved during detection. This would enable a novel fast and low

energy consuming image/object recognition system. Example applications would be counting and identifying manufactured items in a factory and bar code reading among others.

### 5.1.2 Tunable Directional Beaming from Isotropic Light Emitters

In this work, we have demonstrated single directional beaming from an isotropic emitter by application of an appropriately designed GMS( section 3.2). However the beaming abilities of the structures described thus far are fixed once fabrication is complete. We can envision an alternative approach where these structures are redesigned with tunability included. Given that the basic functionality of these devices is based on plasmonic resonances, changing the isotropic emitter surrounding environment can alter the beaming properties. One parameter we can therefore alter, is the refractive index of the surrounding medium. If we can predictably change the refractive index of the dielectric spacer, for example, we are able to change the grating effective optical periodicity, altering its beaming properties. It is important to note that this would also need taking into consideration the phase profile, ensuring it is still intact with the refractive index change. Replacing the dielectric spacer with materials that have an electrically tunable refractive index or integrating micro-heaters that would locally heat this layer up (similarly altering its refractive index) are possible directions to explore in achieving this tunability.

## 5.2 Summary of the Thesis

In this thesis, we have shown a thorough investigation of the design of plasmonic metasurfaces for directional light emission and directional photodetection. This includes theoretical descriptions and verification both experimentally and through extensive numerical simulations. Furthermore, we also explore an application of directional photodetectors in imaging, by designing a lens-less camera based on the compound eye vision modality.

We begin with a brief introduction in chapter 2 of the fundamental theoretical concepts applied in this work. These include the topics of plasmonics, plasmonic grating coupling, extraordinary optical transmission and computational imaging. Even though we do not present an in depth treatment of these topics, we believe that the level at which they are discussed is sufficient for understanding the rationale behind all design choices made in this work and also the basic functionality behind the devices presented. However, readers are still encouraged to consult relevant publications, some of which are found in the reference section, for a more thorough understanding of these topics. In chapter 3, we cover dipole radiation enhancement by near-field coupling to a GMS. Specifically we look at Purcell factor enhancement which can be interesting for overcoming optical losses in low-IQE light sources and also look at the control of radiation directionality both afforded by appropriate design of a GMS. Along with this we also demonstrate a specific implementation of a GMS, operating at a wavelength of $\lambda_0$ = 800 nm, designed to provide tunable directional radiation beaming from isotropic light emitters (CdTe/ZnS QDs in this case). Next, in chapter 4 we move on to designing GMSs that can be integrated with standard off-the-shelf photodetectors enabling directional light detection. We then apply these directional photodetectors towards the realization of artificial compound eye

vision, through computational imaging.

Additional relevant material is included in the appendix, including more detailed explanations of some design rationale followed, a listing of device fabrication recipes used for this work and more detailed discussions on the numerical simulation methods applied, including descriptions of FDTD geometries used and transcripts of relevant MATLAB code. Custom LABView software created over the course of this work for data acquisition and experimental control was not included, but can be accessed by authorized parties on the Paiella Group folder hosted on the Boston University servers.

# Appendix A

# Numerical Simulation Methods

## A.1 HCM FDTD simulations

In this section we describe in more detail the FDTD simulation methods used in the numerical study of the effect of a GMS on light emission via near-field interactions. These calculations were carried out using a commercial FDTD simulation tool (Lumerical), with all the relevant computational parameters carefully optimized through extensive convergence tests. Fig. A·1 shows a schematic cross-sectional view of the simulation geometry, including all monitor surfaces used in the calculations. The computational domain has dimensions along the x, y, and z directions of 6.4$\mu$m, 4.8$\mu$m, and 1.6$\mu$m, respectively. The perfect electric conductor (PEC) of GMS model under study provides the bottom boundary condition, whereas perfectly matched layers (PMLs) are used on all other boundaries. The light source is an oscillating dipole with center emission wavelength $\lambda_0$= 800 nm, oriented along the x, y, or z directions, and located at a variable lateral position x and variable distance d above the GMS. The meta-material slab over the PEC in the GMS model has thickness $\delta = \frac{\lambda_0}{20}$. The specific value of $\delta$ determines the GMS optical losses (in conjunction with the imaginary permittivity and permeability $\kappa$ = 0.18) and the reflection phase at x = 0, i.e., $\Theta\left(0\right) = 2k_0\delta$. Otherwise, it has no effect on the simulation results, as long as it is kept much smaller than $\lambda_0$ .

Monitor M1 in Fig. A·1 is a closed surface that contains only the dipole

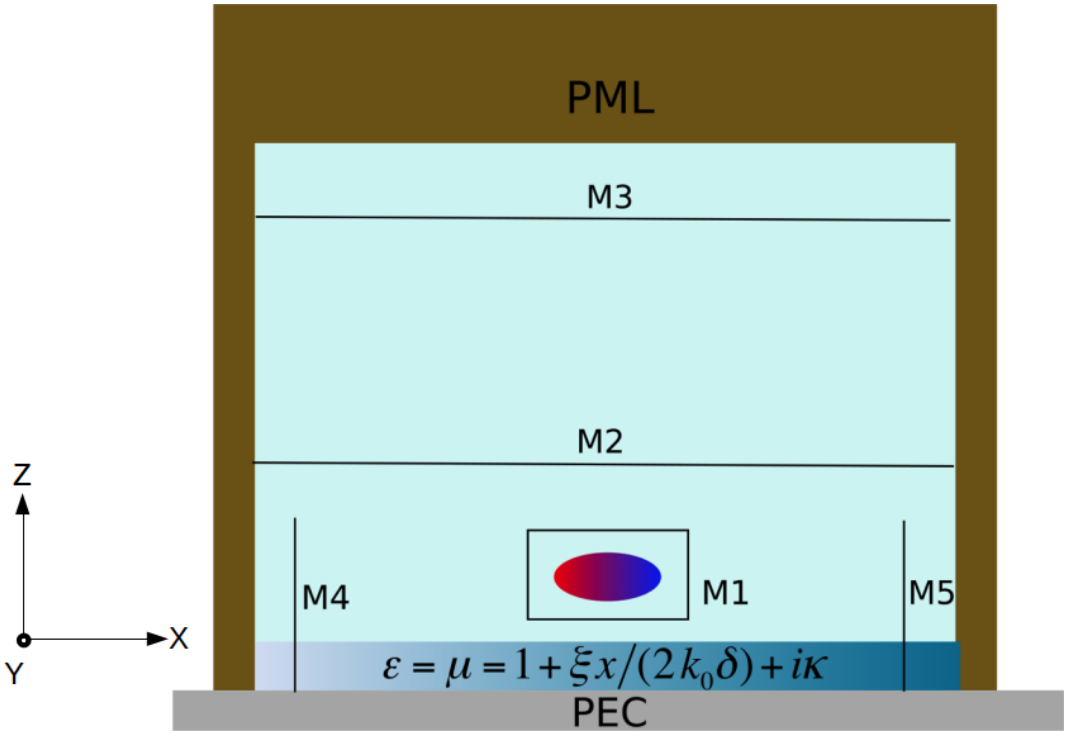


**Figure A·1:** Schematic cross-sectional view of the FDTD simulation geometry used in this work (not drawn to scale).

source. The total optical power $P_{sp}$ crossing this surface in the outward direction is proportional to the probability per unit time $\Gamma_{sp}$ that the dipole decays through the spontaneous excitation of any electromagnetic mode, either radiative or evanescent (with the proportionality constant equal to the emitted photon energy). The Purcell enhancement factor $F_p$ is defined as the ratio $\frac{\Gamma_{sp}}{\Gamma_{sp_0}}$, where $\Gamma_{sp_0}$ is the total spontaneous emission rate of the same dipole in free space. Therefore, $F_p$ can be computed in the FDTD simulations as the ratio $\frac{P_{sp}}{P_{sp_0}}$, where the source power $P_{sp_0}$ is obtained with the same monitor surface M1 surrounding an identical dipole in free space. Monitor M2 is a plane perpendicular to the z direction running across the entire simulation window, located in the near-field zone of the dipole (specifically, at a distance of 260 nm from the GMS). The far-field radiation patterns presented in Fig. 3·4 are obtained by computing the optical field distribution on this monitor

plane, followed by a far-field transformation. Monitor M3 is also a plane parallel to the GMS, and is used (in conjunction with M1) to determine the dipole radiative efficiency

$$\eta = \frac{\Gamma_{rad}}{\Gamma_{sp} + \Gamma_{nr}} = \frac{\Gamma_{rad} \setminus \Gamma_{sp_0}}{\Gamma_{sp} \setminus \Gamma_{sp_0} + \Gamma_{nr} \setminus \Gamma_{sp_0}}. \tag{A.1}$$

In this expression, the radiative decay rate $\Gamma_{rad}$ is the probability per unit time that the dipole decays through the emission of radiative modes propagating away from the GMS, including reflections from the surface (i.e., all the emitted light that can be collected with external optics). The ratio $\frac{\Gamma_{rad}}{\Gamma_{sp_0}}$ is therefore computed as $\frac{P_{out}}{P_{sp_0}}$, where $P_{out}$ is the optical power crossing monitor plane M3. It should be noted that the specific value of this output power $P_{out}$ depends on the distance between M3 and the dipole, which effectively determines the numerical aperture of the collection optics. In all the simulations presented in the main text, M3 is located just above the dipole near-field zone (at a distance of $1\mu$m from the PEC), so as to avoid any contribution to $P_{out}$ from the evanescent components of the dipole field . At the same time, essentially all radiative components are included, except for those propagating along the plane of the GMS (which would not be normally accessible in luminescence measurements anyway). In the denominator of eqA.1, the ratio $\frac{\Gamma_{sp}}{\Gamma_{sp_0}}$ is the aforementioned Purcell enhancement factor computed using monitor M1. The remaining decay rate $\Gamma_{nr}$ accounts for non-radiative processes intrinsic to the emitter material, which do not involve purely electromagnetic interactions and as a result cannot be modeled in the FDTD simulations. The ratio $\frac{\Gamma_{nr}}{\Gamma_{sp_0}}$ is therefore included in the efficiency calculations as an input parameter, related to the dipole IQE:

$$IQE = \frac{1}{1 + \Gamma_{nr} \setminus \Gamma_{sp_0}} \tag{A.2}$$

In order to quantify the impact of the GMS on the dipole radiative efficiency, eq

A.1 is applied to the geometry of Fig. A·1 and to an otherwise identical dipole in free space. For a fair comparison with the reflective GMSs under study, in the latter case the output power $P_{out}$ is computed using two planar monitors, one above and the other below the dipole, both at the same distance from the dipole as monitor M3 in Fig. A·1. With this arrangement, we effectively simulate a dipole located above a perfect mirror in the presence of the same "collection optics" as in Fig. A·1, but without any modification in the spontaneous emission rate that may be caused by the dipole mirror image created by the PEC. Using this procedure, we can finally determine the efficiency ratio $\frac{\eta_{GMS}}{\eta_{mirr}}$, where the subscripts GMS and mirr refer to the same dipole near the GMS and above such a "perfect mirror", respectively. By combining Eq. A.1 for both $\eta_{GMS}$ and $\eta_{mirr}$ and Eq. A.2, this efficiency ratio can be written in terms of the dipole IQE and the FDTD simulation results as follows:

$$\frac{\eta_{GMS}}{\eta_{mirr}} = \frac{P_{out}^{GMS} \setminus P_{out}^{mirr}}{1 + \Big(FP - 1\Big)IQE} \tag{A.3}$$

It should be noted that, while both $P_{out}^{GMS}$ and $P_{out}^{mirr}$ decrease with increasing distance between monitor M3 and the dipole, their ratio in eqA.3 exhibits a much weaker dependence on this distance. Finally, the expected asymmetric excitation of surface waves at the GMS is verified using two additional monitors, M4 and M5. As shown in Fig. A·1, these are two planes perpendicular to the x direction, intersecting the GMS at a small distance (100nm) from, respectively, the left and right boundaries of the simulation domain. The optical power crossing each plane therefore consists of any surface wave excited by the dipole on the GMS, in addition to the light directly radiated by the dipole (or reflected by the GMS) at grazing angles with the x-axis. Exemplary power distribution plots computed on these monitors are shown in Fig. 3·8.

## A.2 Directional Coupler FDTD simulation

There are two types of directional photodetection FDTD simulations that were performed. The first one is a 1-dimensional directional responsivity calculation with incident angles varying in a single plane (x-z) normal to the grating and parallel to the grating coupling directions. In the second type of simulations we calculate the whole 2D grating responsivity varying with both radial and azimuthal angles through reciprocity. The 2D responsivity maps were used for the image reconstruction simuations of the compound eye cameras.

### A.2.1 2D Directional Coupling Simulation

A single metasurface unit cell based on the geometry described in section 4.2, is assembled within a 2D FDTD simulation region as shown in Fig. A·2. In this arrangement, the unit cell is enclosed between periodic boundaries in the x-dimension and perfectly matched layer (PML) boundaries in the in the z dimension, essentially simulating an infinitely long 1D metasurface grating. The source is a monochromatic plane wave whose incident angle is swept from $\pm 85^0$ on the x-z plane. A monitor in the active layer (also indicated in the figure) is used to record the transmission coefficient of the grating at each angle. This calculation was repeated for several devices designed for peak transmission at different angles and also repeatedly run to optimize the various parameters.

### A.2.2 Far Field 3D Reciprocal Directional Coupling Simulation

The full angular response pattern of each optimized device (as a function of both polar and azimuthal illumination angles) is calculated with a reciprocity-based method, because computing the metasurface transmission in a 3D structure for a sufficiently large number of incident directions would be prohibitively

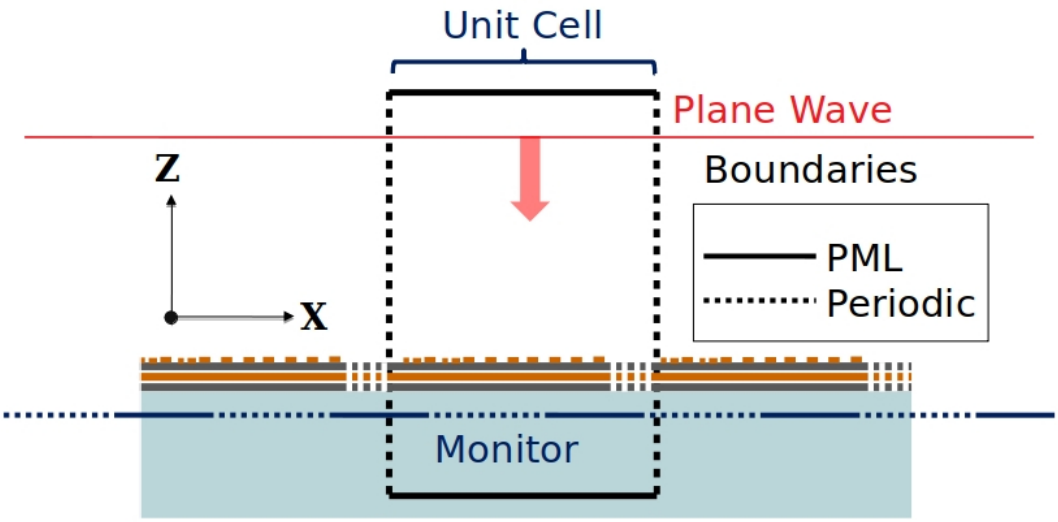


**Figure A·2:** Schematic cross-sectional view of the 2D (x-z) FDTD geometry used in calculating the 1D directional transmission through the GMS.

time consuming. In these simulations, illustrated schematically in Fig. A·3, the simulation which encloses three repeat unit cells contains an electric dipole source positioned on the monitor plane (below the slits) oscillating at the design wavelength $\lambda_0$. This simulation region has grating unit cells surrounded by PML boundaries rather than periodic boundary conditions to avoid periodic repetition of the dipole source leading to a nonphysical inaccurate simulation. This problem is not faced with plane wave sources since they are considered infinite in their extent. In this simulation, the dipole radiation pattern in the air above the metasurface is computed by a far-field transformation of the field distribution on a monitor plane immediately above the NPs. By reciprocity, this pattern is proportional to the local field intensity produced at the dipole location by an incident plane wave as a function of illumination angles. It should be noted that the results of these simulations are somewhat dependent on the specific location of the dipole source, and therefore in principle should be averaged over all possible

positions in the substrate (which again would be prohibitively time consuming). The maps presented in Fig. 4·10 were computed with a dipole located at the position where an incident plane wave along the direction of peak transmission produces the strongest local intensity. The line cuts along the x axis of the radiation patterns obtained with this procedure are in reasonably good agreement with the results of the 2D simulations just described.

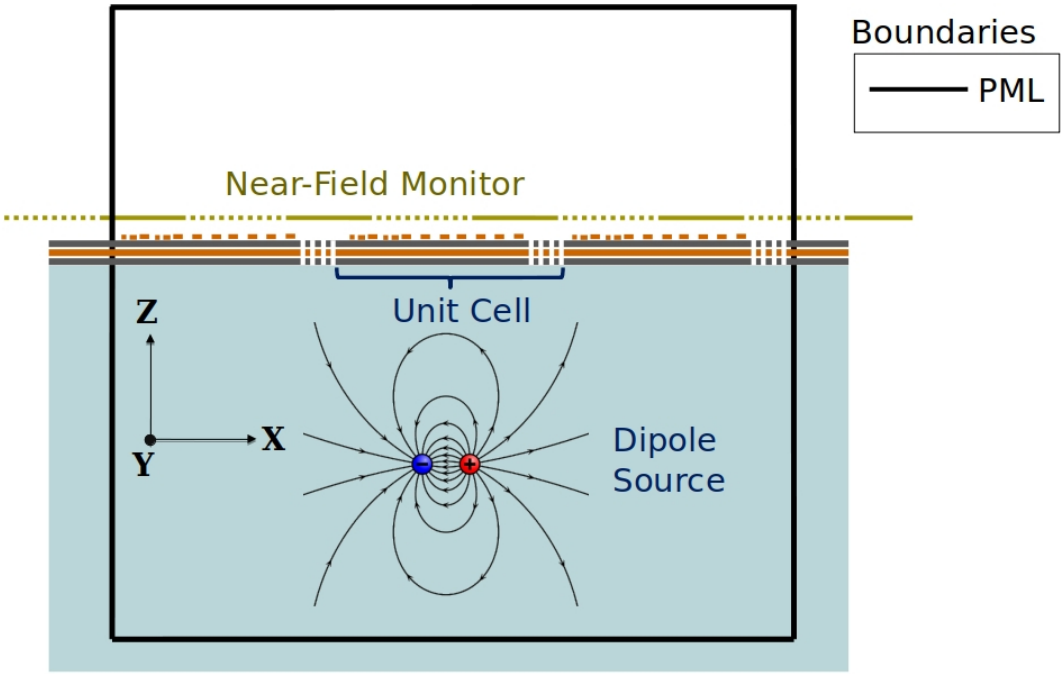


**Figure A·3:** Schematic cross-sectional view of the 3D (xyz) FDTD geometry used in calculating the 2D directional transmission through the GMS by reciprocity.

## A.3 X-Ray Crystallography Technique

In addition to FDTD simulations, we also theoretically investigated GSP metasurface diffraction properties using a general procedure based on well-established X-Ray Crystallography techniques (Kittel, 1986). In this framework, the diffraction patterns of X-rays scattered off a crystal lattice are used to

determine its structure. The idea is that incident X-Rays are scattered in all directions by each atom in a periodic crystal lattice, and these scattered waves interfere constructively in specific directions where their path length differences are equal to integral multiples of the wavelength. Additionally, in crystals with multiple atoms per unit cell, diffraction along some of these directions may vanish due to destructive interference among the contributions from the different atoms in the basis. Analyzing the diffraction pattern in the far field, one can therefore infer both the crystal structure and the structure factor of the unit cell. In our design, we consider the inverse situation where we have a desired far field pattern and accordingly engineer the periodic scattering elements. Here, the grating NP are analogous to the lattice atoms but with the additional property of having a local relative phase shift in the scattered light. With this framework, for a periodic 1D array of sub-wavelength NPs, the amplitude of each grating diffraction order is proportional to the structure factor:

$$S_q = \sum_m e^{i\left(\psi_m - g_q \chi_m\right)} \tag{A.4}$$

where $q$ is the diffraction order, $m$ an index labeling the different NPs in each unit cell, $\chi_m$ and $\psi_m$ are the position and reflection phase of the $m^{th}$ NP, and $g_q = \frac{2\pi q}{\Lambda}$. With this model, we can design and place our scattering elements in a periodic arrangement in such a way to suppress or enhance specific desired diffraction orders corresponding to specific beaming directions. For example, from this equation, forward diffraction can be suppressed in favor of back diffraction by selecting design parameters $\Theta_m$ and $\chi_m$ such that $S_{+q} = 0$ and $S_{-q} \neq 0$.

A Matlab script to solve this equation for different designs predicting the grating beaming properties(APPENDIX B) was used to simulate various designs, and its predictions were verified by rigorous FDTD numerical simulations as

shown in Fig. A·4.

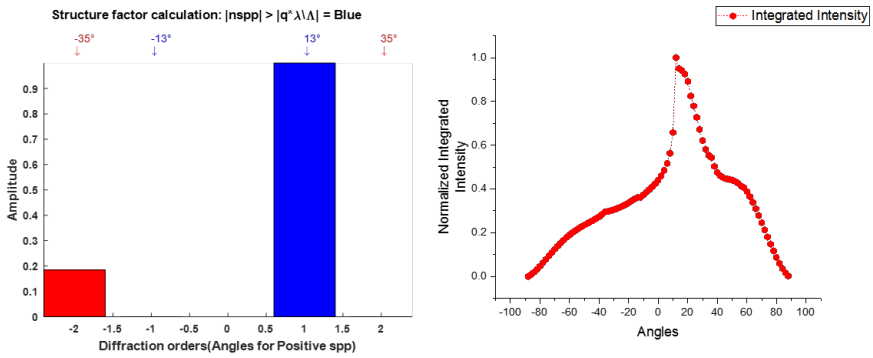


**Figure A·4:** Illustration of the agreement in beaming diffraction orders between the Matlab prediction and FDTD simulations. Left: structure factors associated with the radiative diffraction orders for a specific GMS design predicting peak emission at $13^0$. Right: FDTD simulation of the same structure showing a peak at around $13^0$ which matches well the Matlab results.

This Matlab script presented in Appendix B works in two main steps:

1. Given the positions of the constituent scatterers in a periodic unit cell of a GMS and their respective relative phase delays, we apply the structure factor equation A.4 to determine which diffraction orders are suppressed upon reflection. The orders with high structure factors are favored while those with small ones are proportionally suppressed.

2. Using the grating Bragg condition of Eq. 2.13 we then calculate the corresponding beaming or coupling directions associated with the various diffraction orders, matching them to the results of the previous step.

# Appendix B

# MATLAB Code for Phased Array Design Based on the X-Ray Crystallography method

**Listing B.1:** Function to calculate the structure factor of different grating orders based on the x-ray crystallography method when given the relative positions and relative phases of NPs within a period of a GMS

```
function [sfactor,ang_larg_R,ang_smll_R,dif_larg_R,dif__smll_R,diff0]=
    structurefactor(difforder,capLambda,phases,pos,lambda,nspp,savingpic)
% Function to calculate the structure factor for gratings based on
% xray Crystallography
% [sfactor,withinlightline,thetaneg,thetapos,diffsneg,difspos] =
% structurefactor(difforder,gamma,phases,pos,lambda,nspp)
% spos,sneg -> structure factors positive and negative for
% different orders
% difforder -> maximum diffraction order
% gamma -> grating periodicity(same units as lambda)
% Phases -> reflection phase in radians
% pos -> position of NPs relative to center of unit cell

%Useful variables
numNps=length(phases);
difforders=1:difforder; % Diffraction orders
allowed=difforders(abs(nspp-difforders.*lambda/capLambda)<=1);

% Calculate diffraction angles that would couple to SPP
dif_larg_R=allowed(nspp < (allowed.*lambda/capLambda));
dif__smll_R=allowed(nspp >= (allowed.*lambda/capLambda));
```

```
ang_smll_R=asind(abs(nspp-dif__smll_R.*lambda/capLambda));
ang_larg_R=asind(abs(nspp-dif_larg_R.*lambda/capLambda));

radiative=max([dif_larg_R,dif__smll_R]);
diff0=-radiative:radiative;
latticevec=diff0*2*pi/capLambda;
numdifforder=length(diff0);
sfactortemp=zeros(1,numdifforder);

for cts=1:numdifforder
    for ctnp=1:numNps
        sfactortemp(cts)= sfactortemp(cts)+...
                    exp(1i*(phases(ctnp)-latticevec(cts)*pos(ctnp)));
    end
end
sfactor=abs(sfactortemp/numNps).^2;

subplot(8,9,1:8)
title('Structure factor calculation: |nspp| > |q*\lambda\\\Lambda| = Blue')
axis off;

subplot(8,9,17:72)
hold on
bar(diff0(ismember(abs(diff0),dif__smll_R)),...
    sfactor(ismember(abs(diff0),dif__smll_R)),...
    0.4, 'b');

bar(diff0(ismember(abs(diff0),dif_larg_R)),...
    sfactor(ismember(abs(diff0),dif_larg_R)),...
    0.4, 'r');
axis([-inf inf 0 max(sfactor)])
xlabel('Diffraction orders(Angles for Positive spp)')
ylabel('Amplitude')
set(gca,'FontWeight','bold')
for ctr=1:length(ang_larg_R)
    text(dif_larg_R(ctr),...
        max(sfactor)+max(sfactor)/10,...
```

```
        [num2str(round(ang_larg_R(ctr))),char(176)],...
        'Color','r','FontSize',10);
   text(dif_larg_R(ctr),...
         max(sfactor)+max(sfactor)/18,...
        '\downarrow',...
        'Color','r','FontSize',10);
    text(-dif_larg_R(ctr),...
         max(sfactor)+max(sfactor)/10,...
        [num2str(-round(ang_larg_R(ctr))),char(176)],...
        'Color','r','FontSize',10);
    text(-dif_larg_R(ctr),...
         max(sfactor)+max(sfactor)/18,...
        '\downarrow',...
        'Color','r','FontSize',10);
end


for ctr=1:length(ang_smll_R)
    text(dif__smll_R(ctr),...
         max(sfactor)+max(sfactor)/10,...
        [num2str(round(ang_smll_R(ctr))),char(176)],...
        'Color','b','FontSize',10);
    text(dif__smll_R(ctr),...
         max(sfactor)+max(sfactor)/18,...
        '\downarrow',...
        'Color','b','FontSize',10);
    text(-dif__smll_R(ctr),...
        max(sfactor)+max(sfactor)/10,...
        [num2str(-round(ang_smll_R(ctr))),char(176)],...
        'Color','b','FontSize',10);
    text(-dif__smll_R(ctr),...
         max(sfactor)+max(sfactor)/18,...
        '\downarrow',...
        'Color','b','FontSize',10);
end
hold off
if savingpic
```

```
    name=strrep(date,'-','_');
saveas(gcf,[name,'_',num2str(numNps),'_',num2str(capLambda*1e9)],'jpg');
end

end
```

**Listing B.2:** Script to calculate the structure factor of different gratingorders for an example GMs geometry using the structure factor function

```
% Script to calculate the structure factor of different grating
% orders for an example GMs geometry using the structure factor
% function
clc;
clear;
close all hidden;

% Fixed constants
difforder=100;
capLambda=6000e-9; % Grating Periodicity
lambda=1500e-9; % Incident Wavelength
nspp=1550/1524; % Target SPP effective refractive index
periodic=0; % Use a periodic arrangement of nano-particles within
            % a unit cell or specify relative positions
            % and relative phase for each
savingpic=0; % Whether or not to save resulting picture

if (periodic)
    phases=([0:2]*360/3)*pi/180; %radians
    pos=flip([0:(length(phases)-1)]*capLambda/length(phases));
else
    phases=[-114,-24,66,156,-114,-42,30,102,174]*pi/180; %radians
    pos = [-7/8,-5/8,-3/8,-1/8,1/8,1/8+1/5,1/8+2/5,1/8+3/5,1/8+4/5]...
          *capLambda;
end
[sfactor,ang_larg_R,ang_smll_R,dif_larg_R,dif__smll_R,diff0]=...
structurefactor(difforder,capLambda,phases,pos,lambda,nspp,savingpic);
```

# Appendix C

# Knife Edge Method for Beam Quality Measurement

In order to obtain accurate directional detector measurements we need to ensure that the focused beam projected on the sample has a symmetric profile with known width. Any artifacts in the beam profile may distort the directional measurement results. Knowledge of the beam width is also useful during alignment. In order to achieve this, we have applied the knife edge method of measuring the beam profile. The measurement principle is as follows:

1. The beam is focused by a lens and its waist located.

2. The beam is then progressively covered by a blade (knife edge) translated perpendicularly across the beam, as the transmitted power is measured. In this arrangement, the measured beam power slowly decreases from its maximum value when the beam is completely unobstructed to zero when the beam is completely blocked, resulting in the profile shown in Fig. C·1(a).

3. The derivative of this curve is then computed to determine beam intensity profile, which we can fit to a Gaussian function to extract the beam width parameter $\sigma$. The Matlab code developed for this purpose is presented below and a representative fit is shown in Fig. C·1(b). In addition to the beam width, with this plot we can check whether the beam profile is symmetric and smooth as required.

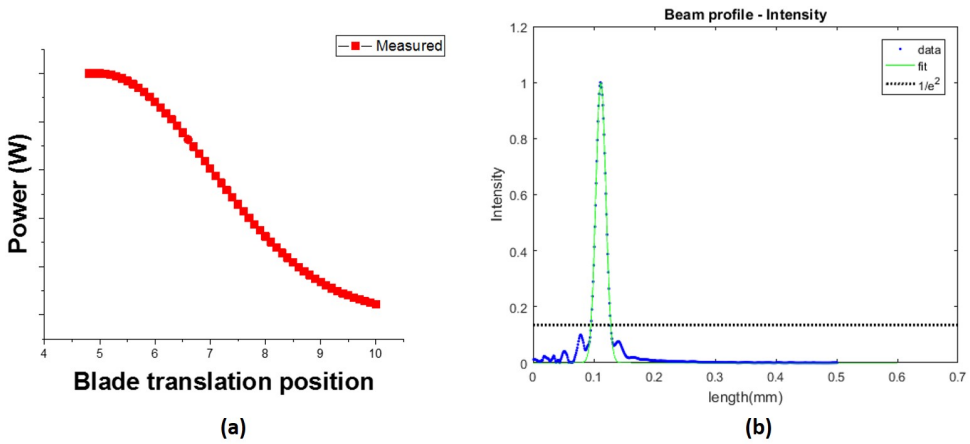


**Figure C·1:** (a) Typical curve obtained from the Knife Edge method measurement. (b) Sample experimental data showing the Gaussian fit to determine beam dimensions.

## C.1 MATLAB Code for the Knife Edge Beam Measurement

**Listing C.1:** Script to calculate the laser beam width based on the Knife edge method

```
clc
clear
close all hidden

%% Loading Processing Raw data

%Load Data
[pos,pow]=LoadKnifeEdge('filename.csv');
%Smoothing
pow=smooth(pos,pow,0.06,'loess');
%Calculate derivative
dbeam=abs(diff(pow)./diff(pos));
%normalize
dbeam=dbeam/max(dbeam);
%fit
f = fit(pos(2:end),dbeam,'gauss1');
```

```
%% Plot Raw Data Normalized:
figure(1)
plot(pos,pow/max(pow),'b.-')
%axis([.95,1.22,0,1])
xlabel('length(mm)')
ylabel('pow')
title('Beam profile - Raw Data')

%% Plot Beam Intensity Profile

figure(4)
plot(pos(2:end),dbeam,'b.')
hold on
plot(f,'g')
hline = refline([0 0.1353]);
hline.Color = 'k';
hline.LineStyle = ':';
hline.LineWidth=2;
%axis([.95,1.22,0,1])
xlabel('length(mm)')
ylabel('Intensity')
title('Beam profile - Intensity')
legend('data','fit','1/e^2')

%widths in mm
fprintf(' Fit width in um: %f\n',2.35482*f.c1*1000);
```

# Appendix D

# Sample Preparation Procedure and Fabrication Recipes

## D.1 Sample Solvent Cleaning

Sample solvent cleaning in this project was mainly carried out to remove any dust particles or remaining resist on the sample after each processing step. In this case, a simple solvent cleaning is sufficient. Each cleaning session takes approximately 5 minutes per sample. Here is the simple procedure:

1. Place the sample in Acetone at room temperature and sonicate in an ultrasonic bath for 2 min. This removes any particles on the surface of the sample and dissolves any resist residue on the surface.

2. Quickly transfer into a Isopropyl Alcohol (IPA) solution and sonicate for 1 min. Do not let the acetone dry out on the substrate surface. IPA dissolves Acetone and is soluble in Deionized (DI) Water and therefore serves as a buffer step.

3. Transfer the samples into DI water and sonicate for 1 min. At this point the samples should be completely clean. DI water is also particularly important for Germanium samples since it also dissolves away any native oxide on the sample surface (Onsia et al., 2005) which is important for good conductivity between the Au contacts and Germanium substrate.

4. Dry off using a nitrogen gas gun blowing for about 30seconds. The sample is now clean and ready for processing.

## D.2 Lithography

### D.2.1 Photo-Lithography Mask

For the Photo-Lithography steps the mask Computer Aided Design (CAD) is made in Autocad 2016 software and written on a 5x5 inch chrome plate in the Heidelberg MLA 150 Maskless Aligner. The blank mask consists of a soda lime Substrate with 5300 A of AZ1518 photo-resist and LRC thin film coating made by nanofilm. The exposed mask is developed in MF319 developer and the chrome etched in a Chrome Etch solution from Transene before removing the residue photo-resist in the photo-resist stripper 1165 solution. The Photo-lithography masks have several different design geometries, each for a specific layer of fabrication. For each design there are at least two copies made on each mask for redundancy.

### D.2.2 Photo-Lithography Process

Each photo-lithography step is done on the Karl Suss MA6 mask aligner. S1813 positive photo-resist from Shirpley and AZ524-E image reversal resist were used at different points of the design. The different resist types (positive vs image reversal) are selected depending on the specific mask patterns designed to allow for maximum visibility of the substrate under the mask for easy alignment during UV exposure. The two different resist lithography procedures are outlined below:

**Photoresist S1813 Recipe:**

1. Clean the sample according to the procedure outlined in a previous section.

2. Spin S1813 at 4000 rpm for 60 s with 1000 rpm/s ramp.
3. Bake at 115° for 60 s
4. Expose at 10 W power at 405 nm wavelength for 7 s.
5. Develop in MF319 for 45 s

**Photoresist AZ5214-E Recipe:**

1. Clean the sample according to the procedure outlined in a previous section.
2. Spin AZ5214-E at 5000 rpm for 60 s with 1000 rpm/s ramp.
3. Bake at 110° for 60 s
4. Expose at 10 W power at 405 nm wavelength for 4 s with the mask after appropriate alignment of the sample.
5. Bake at 120° for 120 s
6. Flood expose (with no mask) at 10 W power at 405 nm wavelength for 60 s.
7. Develop in AZ400K for 15 s

### D.2.3 Electron-Beam Lithography Process

All Electron Beam(E-Beam) Lithography steps are carried out in the Zeiss supra40 30KV E-Beam system.

**PMMA - HSQ bilayer slit definition**

For fabricating slits in the Gold film, PMMA (Polymethyl Methacrylate) A4 E-beam resist from MicroChem and HSQ (Hydrogen Silsesquioxane) XR-1541-6 E-beam resist from Dow Corning® are used in a bi-layer technique adapted from ref(Yang et al., 2008). Our procedure is outlined below.

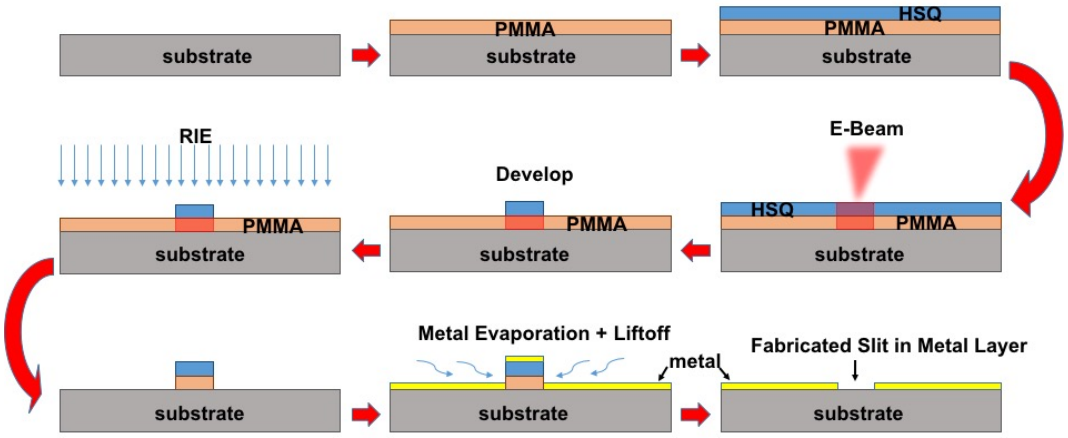


**Figure D·1:** PMMA - HSQ bilayer technique

1. The samples undergo a solvent clean according to the procedure outlined in D.1.

2. PMMA A4 is spun at 5000 rpm for 1 min with a 1000 rpm/s ramp.

3. The spun sample is baked at $180^0C$ on a hot plate for 1 min.

4. HSQ is then spun on at 5000 rpm for 1 min with a 1000 rpm/s ramp.

5. The spun sample is baked again at $180^0C$ on a hot plate for 2 min.

6. The substrate is then exposed to the electron beam in a Zeiss Supra40 SEM converted to Ebeam writer machine to define the slits. The exposure dosage depends on the number of slits in each group. For 5 slits per group the dosage is $195\frac{\mu C}{cm^2}$, while for 9 slits per group the dosage is $143\frac{\mu C}{cm^2}$.

7. The exposed substrate is then developed in MF319 developer for 3min. This removes the unexposed HSQ but does not affect the PMMA layer.

8. After development, the PMMA in all areas except those covered by the developed HSQ is etched in a Reactive Ion Etcher system with the following parameters:

(a) Gas: $O_2$

(b) Flow: 30 sccm

(c) Pressure: 50 mTorr

(d) Power: 100 W

(e) Time: 1 min

9. The Au film in which the slits are to be fabricated is then evaporated on the sample and lifted-off in acetone solution.

**PMMA E-beam procedure**

1. The samples undergo a solvent clean according to the procedure outlined in D.1.

2. PMMA A4 is spun at 4000 rpm for 1 min with a 1000 rpm/s ramp and baked in an oven for 20 min at $180^0C$

3. The spun sample is then exposed to the electron beam at $253\frac{\mu C}{cm^2}$.

4. The exposed substrate is then developed according to the following procedure:

   (a) Agitate in a MIBK (Methyl isobutyl ketone):IPA (Isopropanol) 1:3 mixture for 70 s.

   (b) Agitate in IPA for 20 s.

   (c) Rinse in DI (De-Ionized) water.

5. The material film to be patterned is then evaporated on the sample and lifted-off in acetone solution.

## D.3 Material Deposition

$SiO_2$ layers are sputtered in the Angstrom Engineering EVOVAC sputtering system with $SiO_2$ targets from Kurt Lesker. The Au films are evaporated in a high vacuum CHA Industries Solution Process Development System metal evaporator at 0.5 A/s rate and vacuum of at least $8 \times 10^7 mTorr$.

### D.3.1 SiO2 Sputtering

1. Load the RF target and pump down to at least $8x10^{-7} Torr$
2. Chamber preconditioning: 330W RF power for 10min followed by 300W RF power for 5min at 5mTorr pressure.
3. Process parameters: 300W RF power at 5mTorr pressure

## D.4 Wire Bonding

The finished directional sensor chips are wire bonded using the Kulicke & Soffa 4124 ball bonder.

# Appendix E

# Unsuccessful Approaches

## E.1 FIB Milling of a 50% duty cycle 400-nm periodic array of slits in 100-nm-thick Au film

**Motivation**

Using the Quanta 3D FEG Focused Ion Beam(FIB) system, we tried to etch a 400 nm grating of slits with a 50% duty cycle in a 100-nm-thick Gold film for the directional image sensors described in section 4.3. This would form our transmission slits. FIB milling was attractive for this purpose for two main reasons:

1. The slits would be etched in one step as opposed to the alternative two-step process (lithography and lift-off), reducing fabrication complexity.

2. Alignment of the slits between grating sections would be straightforward by utilizing the FIB system Scanning Electron Microscope (SEM) capabilities, eliminating the need for alignment markers or any other complicated alignment schemes.

**Obstacles**

There were two main problems encountered:

1. The resulting edge profile was sloped (with the slits getting narrower the deeper they went). This made it difficult to fabricate as there was always a trade off on how close the slits could be versus how deep we could etch them.

For our very small grating periodicity of 400 nm and film thickness of 100 nm, the slits would sometimes merge together if we tried to make them deep or would not be etched all the way through if we tried to keep them separate. It was also difficult to determine if the slits were etched all the way through the Au layer.

2. The FIB milling parameters were not fully reproducible, having high sensitivity to external factors like room temperature and humidity. Even opening the door to the FIB instrument room during milling could alter these parameters affecting fabrication quality. In addition, during milling, the FIB beam aperture would also change as its edges are eroded, further altering parameters like focus and power. Minor changes in these parameters would affect fabrication quality, thus requiring re-calibration dosage tests sometimes several times during a fabrication run. This resulted in a very low yield.

## E.2 Fabrication of a 50% duty cycle 400-nm periodic array of slits in 100-nm Au by a negative resist process.

**Motivation**

After unsuccessfully applying FIB milling for fabricating a 400 nm slit grating with 50% duty cycle in 100-nm-thick gold, we tried to do the same with a negative resist E-beam method. The main advantage of using a negative resist for this purpose is that we could write only the slits during exposure keeping fabrication time minimal, as opposed to exposing the inverse area with a typical positive E-beam procedure which would take much longer. The resist chosen was HSQ.

**Obstacles**

However it was found that this selected E-beam resist would stick very strongly to the Gold film after metal evaporation rendering lift-off impossible.
After several runs of unsuccessful slit grating fabrications, this approach was finally abandoned in favor of the PMMA-HSQ bi-layer E-beam method outlined in appendix D.2.3.

## E.3 Deposition of a smooth $MgF_2$ film by Thermal Evaporation

**Motivation**

Owing to its superior E-beam evaporation properties (it evaporates cleanly and completely, without out-gassing or spitting,leaving a hard, uniform coating on the substrate),relatively low refractive index, and better adhesion to Gold compared to the alternative $SiO_2$, $MgF_2$ was viewed as a good material for the dielectric spacer in our directional detectors described in section 4.3.

**Obstacles**

However we also discovered that if $MgF_2$ penetrates into the metal evaporation system cryo-pump, it can permanently coat the condensing array damaging it. This is further exacerbated by $MgF_2$'s low vapor pressure resulting in out-gassing even at room temperature during pump down. While a nitrogen trap in the evaporation system would help mitigate this issue by condensing $MgF_2$ particles before they got to the cryo-pump, the only material evaporation system in our cleanroom with a nitrogen trap is an Edwards thermal evaporator. However, we were unable to consistently get optically smooth films appropriate for our devices with thermal evaporation, finally opting for sputtered $SiO_2$ instead.

## E.4 Combining Ebeam-lithography and Photo-lithography lift-off to a single step.

### Motivation

We had an idea to combine some of the Photo-lithography and Ebeam lithography steps into one lift-off procedure. This was to be done by first carrying out photo-lithography including development, then Ebeam lithogaphy similarly before finally doing the lift-off of both layers at once by dipping the sample in Acetone. The E-beam resist was PMMA and the Photo-resist was AZ5214E from MicroChemicals. This procedure was possible for the layers where there was no overlap in the areas covered by the Photo and Ebeam resists after development. The main advantage of this process would be time saving and reduced fabrication complexity by reducing the number of steps.

### Obstacles

However it was found that the hard bake used in the E-beam lithography step would harden the Photo-resist from the Photo-lithography step making it impossible to lift-off. We tried the inverse process of doing the Ebeam lithography first but similarly the extra baking hindered lift-off.

# References


Aieta, F., Genevet, P., Kats, M. A., Yu, N., Blanchard, R., Gaburro, Z., and Capasso, F. (2012). Aberration-free ultrathin flat lenses and axicons at telecom wavelengths based on plasmonic metasurfaces. *Nano Letters*, 12(9):4932–4936.

Amos, R. M. and Barnes, W. L. (1997). Modification of the spontaneous emission rate of $eu^{3+}$ ions close to a thin metal mirror. *Physical Review B*, 55:7249–7254.

Barnes, W. L. (1998). Fluorescence near interfaces: The role of photonic mode density. *Journal of Modern Optics*, 45(4):661–699.

Boroditsky, M., Krauss, T., Coccioli, R., Vrijen, R., Bhat, R., and Yablonovitch, E. (1999). Light extraction from optically pumped light-emitting diode by thin-slab photonic crystals. *Applied Physics Letters*, 75(8):1036–1038.

Cesario, J., Gonzalez, M. U., Cheylan, S., Barnes, W. L., Enoch, S., and Quidant, R. (2007). Coupling localized and extended plasmons to improve the light extraction through metal films. *Optics express*, 15(17):10533–10539.

Chu, Y. and Crozier, K. B. (2009). Experimental study of the interaction between localized and propagating surface plasmons. *Optics letters*, 34(3):244–246.

Chuang, S. L. (2009). *Physics of Photonic Devices*. Wiley Publishing, 2 edition.

Deng, Z., Chen, F., Yang, Q., Bian, H., Du, G., Yong, J., Shan, C., and Hou, X. (2016). Dragonfly-eye-inspired artificial compound eyes with sophisticated imaging. *Advanced Functional Materials*, 26(12):1995–2001.

DiMaria, J., Dimakis, E., Moustakas, T. D., and Paiella, R. (2013). Plasmonic off-axis unidirectional beaming of quantum-well luminescence. *Applied Physics Letters*, 103(25):251108.

Drexhage, K. H. (1974). Iv interaction of light with monomolecular dye layers. volume 12 of *Progress in Optics*, pages 163 – 232. Elsevier.

Duparré, J., Dannberg, P., Schreiber, P., Bräuer, A., and Tünnermann, A. (2005). Thin compound-eye camera. *Applied Optics*, 44(15):2949–2956.

Ebbesen, T. W., Lezec, H. J., Ghaemi, H., Thio, T., and Wolff, P. (1998). Extraordinary optical transmission through sub-wavelength hole arrays. *Nature*, 391(6668):667.

Erchak, A. A., Ripin, D. J., Fan, S., Rakich, P., Joannopoulos, J. D., Ippen, E. P., Petrich, G. S., and Kolodziejski, L. A. (2001). Enhanced coupling to vertical radiation using a two-dimensional photonic crystal in a semiconductor light-emitting diode. *Applied Physics Letters*, 78(5):563–565.

Fatemi, R., Abiri, B., Khachaturian, A., and Hajimiri, A. (2018). High sensitivity active flat optics optical phased array receiver with a two-dimensional aperture. *Optics Express*, 26(23):29983–29999.

Floreano, D., Pericet-Camara, R., Viollet, S., Ruffier, F., Brückner, A., Leitel, R., Buss, W., Menouni, M., Expert, F., Juston, R., Dobrzynski, M. K., L'Eplattenier, G., Recktenwald, F., Mallot, H. A., and Franceschini, N. (2013). Miniature curved artificial compound eyes. *Proceedings of the National Academy of Sciences*, 110(23):9267–9272.

Ford, G. and Weber, W. (1984). Electromagnetic interactions of molecules with metal surfaces. *Physics Reports*, 113(4):195 – 287.

Genevet, P., Yu, N., Aieta, F., Lin, J., Kats, M. A., Blanchard, R., Scully, M. O., Gaburro, Z., and Capasso, F. (2012). Ultra-thin plasmonic optical vortex plate based on phase discontinuities. *Applied Physics Letters*, 100(1):013101.

Gérard, J. M., Sermage, B., Gayral, B., Legrand, B., Costard, E., and Thierry-Mieg, V. (1998). Enhanced spontaneous emission by quantum boxes in a monolithic optical microcavity. *Physical Review Letters*, 81:1110–1113.

Ghoshal, A., Divliansky, I., and Kik, P. G. (2009). Experimental observation of mode-selective anticrossing in surface-plasmon-coupled metal nanoparticle arrays. *Applied Physics Letters*, 94(17):171108.

Gill, P. R., Lee, C., Lee, D.-G., Wang, A., and Molnar, A. (2011). A microscale camera using direct fourier-domain scene capture. *Optics Letters*, 36(15):2949–2951.

Gontijo, I., Boroditsky, M., Yablonovitch, E., Keller, S., Mishra, U. K., and DenBaars, S. P. (1999). Coupling of ingan quantum-well photoluminescence to silver surface plasmons. *Physical Review B*, 60:11564–11567.

Greffet, J.-J., Carminati, R., Joulain, K., Mulet, J.-P., Mainguy, S., and Chen, Y. (2002). Coherent emission of light by thermal sources. *Nature*, 416(6876):61.

Healy, D. and Brady, D. J. (2008). Compression at the physical interface. *IEEE signal processing Magazine*, 25(2):67–71.

Jeong, K.-H., Kim, J., and Lee, L. P. (2006). Biologically inspired artificial compound eyes. *Science*, 312(5773):557–561.

Karimi, E., Schulz, S. A., De Leon, I., Qassim, H., Upham, J., and Boyd, R. W. (2014). Generating optical orbital angular momentum at visible wavelengths using a plasmonic metasurface. *Light: Science and Applications*, 3(5):e167.

Keum, D., Jang, K.-W., Jeon, D. S., Hwang, C. S. H., Buschbeck, E. K., Kim, M. H., and Jeong, K.-H. (2018). Xenos peckii vision inspires an ultrathin digital camera. *Light: Science and Applications*, 7(1):80.

Kittel, C. (1986). *Introduction to solid state physics*. Wiley.

Krishnamoorthy, H. N. S., Jacob, Z., Narimanov, E., Kretzschmar, I., and Menon, V. M. (2012). Topological transitions in metamaterials. *Science*, 336(6078):205–209.

Kurosaka, Y., Iwahashi, S., Liang, Y., Sakai, K., Miyai, E., Kunishi, W., Ohnishi, D., and Noda, S. (2010). On-chip beam-steering photonic-crystal lasers. *Nature Photonics*, 4(7):447.

Land, M. F. and Nilsson, D.-E. (2002). *Animal eyes*. Oxford University Press.

Lin, D., Fan, P., Hasman, E., and Brongersma, M. L. (2014). Dielectric gradient metasurface optical elements. *Science*, 345(6194):298–302.

Lin, J., Mueller, J. B., Wang, Q., Yuan, G., Antoniou, N., Yuan, X.-C., and Capasso, F. (2013). Polarization-controlled tunable directional coupling of surface plasmon polaritons. *Science*, 340(6130):331–334.

Lin, L., Goh, X. M., McGuinness, L. P., and Roberts, A. (2010). Plasmonic lenses formed by two-dimensional nanometric cross-shaped aperture arrays for fresnel-region focusing. *Nano letters*, 10(5):1936–1940.

López-Tejeira, F., Rodrigo, S. G., Martín-Moreno, L., García-Vidal, F. J., Devaux, E., Ebbesen, T. W., Krenn, J. R., Radko, I., Bozhevolnyi, S. I., González, M. U., et al. (2007). Efficient unidirectional nanoslit couplers for surface plasmons. *Nature Physics*, 3(5):324.

Maier, S. (2010). *Plasmonics: Fundamentals and Applications*. Springer US.

Mertens, H., Biteen, J. S., Atwater, H. A., and Polman, A. (2006). Polarization-selective plasmon-enhanced silicon quantum-dot luminescence. *Nano Letters*, 6(11):2622–2625.

Nayar, S. K. (2006). Computational cameras: Redefining the image. *Computer*, 39(8):30–38.

Neifeld, M. A. and Shankar, P. (2003). Feature-specific imaging. *Applied Optics*, 42(17):3379–3389.

Ni, X., Emani, N. K., Kildishev, A. V., Boltasseva, A., and Shalaev, V. M. (2012). Broadband light bending with plasmonic nanoantennas. *Science*, 335(6067):427–427.

Noda, S., Fujita, M., and Asano, T. (2007). Spontaneous-emission control by photonic crystals and nanocavities. *Nature photonics*, 1(8):449.

Novotny, L. and Van Hulst, N. (2011). Antennas for light. *Nature photonics*, 5(2):83.

Okamoto, K., Niki, I., Shvartser, A., Narukawa, Y., Mukai, T., and Scherer, A. (2004). Surface-plasmon-enhanced light emitters based on ingan quantum wells. *Nature materials*, 3(9):601.

Onsia, B., Conard, T., De Gendt, S., Heyns, M. M., Hoflijk, I., Mertens, P. W., Meuris, M., Raskin, G., Sioncke, S., Teerlinck, I., Theuwis, A., Van Steenbergen, J., and Vinckier, C. (2005). A study of the influence of typical wet chemical treatments on the germanium wafer surface. In *Ultra Clean Processing of Silicon Surfaces VII*, volume 103 of *Solid State Phenomena*, pages 27–30. Trans Tech Publications.

Paiella, R. (2005). Tunable surface plasmons in coupled metallo-dielectric multiple layers for light-emission efficiency enhancement. *Applied Physics Letters*, 87(11):111104.

Pors, A., Nielsen, M. G., Bernardin, T., Weeber, J.-C., and Bozhevolnyi, S. I. (2014). Efficient unidirectional polarization-controlled excitation of surface plasmon polaritons. *Light: Science and Applications*, 3(8):e197.

Pors, A., Nielsen, M. G., Della Valle, G., Willatzen, M., Albrektsen, O., and Bozhevolnyi, S. I. (2011). Plasmonic metamaterial wave retarders in reflection by orthogonally oriented detuned electrical dipoles. *Optics letters*, 36(9):1626–1628.

Porto, J. A., García-Vidal, F. J., and Pendry, J. B. (1999). Transmission resonances on metallic gratings with very narrow slits. *Physical Review Letters*, 83:2845–2848.

Potton, R. J. (2004). Reciprocity in optics. *Reports on Progress in Physics*, 67(5):717.

Pozar, D. M., Targonski, S. D., and Syrigos, H. (1997). Design of millimeter wave microstrip reflectarrays. *IEEE transactions on antennas and propagation*, 45(2):287–296.

Purcell, E. M. (1946). Spontaneous emission probabilities at radio frequencies. volume 69, pages 681+.

Raskar, R. (2009). Computational photography: Epsilon to coded photography. In *Emerging Trends in Visual Computing*, pages 238–253. Springer.

Rattier, M., Benisty, H., Schwoob, E., Weisbuch, C., Krauss, T., Smith, C., Houdre, R., and Oesterle, U. (2003). Omnidirectional and compact guided light extraction from archimedean photonic lattices. *Applied physics letters*, 83(7):1283–1285.

Roberts, A. and Lin, L. (2012). Plasmonic quarter-wave plate. *Optics letters*, 37(11):1820–1822.

Shi, C., Wang, Y., Liu, C., Wang, T., Zhang, H., Liao, W., Xu, Z., and Yu, W. (2017). Scecam: a spherical compound eye camera for fast location and recognition of objects at a large field of view. *Optics Express*, 25(26):32333–32345.

Shimizu, K. T., Woo, W. K., Fisher, B. R., Eisler, H. J., and Bawendi, M. G. (2002). Surface-enhanced emission from single semiconductor nanocrystals. *Physical Review Letters*, 89:117401.

Song, J.-H., Atay, T., Shi, S., Urabe, H., and Nurmikko, A. V. (2005). Large enhancement of fluorescence efficiency from cdse/zns quantum dots induced by resonant coupling to spatially controlled surface plasmons. *Nano Letters*, 5(8):1557–1561. PMID: 16089488.

Song, Y. M., Xie, Y., Malyarchuk, V., Xiao, J., Jung, I., Choi, K.-J., Liu, Z., Park, H., Lu, C., Kim, R.-H., et al. (2013). Digital cameras with designs inspired by the arthropod eye. *Nature*, 497(7447):95.

Sun, G., Khurgin, J. B., and Soref, R. A. (2007). Practicable enhancement of spontaneous emission using surface plasmons. *Applied Physics Letters*, 90(11):111107.

Sun, S., He, Q., Xiao, S., Xu, Q., Li, X., and Zhou, L. (2012a). Gradient-index meta-surfaces as a bridge linking propagating waves and surface waves. *Nature materials*, 11(5):426.

Sun, S., Yang, K.-Y., Wang, C.-M., Juan, T.-K., Chen, W. T., Liao, C. Y., He, Q., Xiao, S., Kung, W.-T., Guo, G.-Y., Zhou, L., and Tsai, D. P. (2012b). High-efficiency broadband anomalous reflection by gradient meta-surfaces. *Nano Letters*, 12(12):6223–6229. PMID: 23189928.

Tanida, J., Kumagai, T., Yamada, K., Miyatake, S., Ishida, K., Morimoto, T., Kondou, N., Miyazaki, D., and Ichioka, Y. (2001). Thin observation module by bound optics (tombo): concept and experimentalverification. *Applied Optics*, 40(11):1806–1813.

van Beijnum, F., Rétif, C., Smiet, C. B., Liu, H., Lalanne, P., and van Exter, M. P. (2012). Quasi-cylindrical wave contribution in experiments on extraordinary optical transmission. *Nature*, 492(7429):411.

Wierer Jr, J. J., David, A., and Megens, M. M. (2009). Iii-nitride photonic-crystal light-emitting diodes with high extraction efficiency. *Nature Photonics*, 3(3):163.

Willets, K. A. and Van Duyne, R. P. (2007). Localized surface plasmon resonance spectroscopy and sensing. *Annual Review of Physical Chemistry*, 58(1):267–297. PMID: 17067281.

Xu, Y., Gu, C., Hou, B., Lai, Y., Li, J., and Chen, H. (2013). Broadband asymmetric waveguiding of light without polarization limitations. *Nature communications*, 4:2561.

Yablonovitch, E. (1987). Inhibited spontaneous emission in solid-state physics and electronics. *Physical Review Letters*, 58:2059–2062.

Yang, H., Jin, A., Luo, Q., Li, J., Gu, C., and Cui, Z. (2008). Electron beam lithography of hsq/pmma bilayer resists for negative tone lift-off process. *Microelectronic Engineering*, 85(5):814 – 817. Proceedings of the Micro- and Nano-Engineering 2007 Conference.

Yin, L., Vlasko-Vlasov, V., Rydh, A., Pearson, J., Welp, U., Chang, S.-H., Gray, S., Schatz, G., Brown, D., and Kimball, C. W. (2004). Surface plasmons at single nanoholes in au films. *Applied physics letters*, 85(3):467–469.

Yin, X., Ye, Z., Rho, J., Wang, Y., and Zhang, X. (2013). Photonic spin hall effect at metasurfaces. *Science*, 339(6126):1405–1407.

Yu, N., Genevet, P., Kats, M. A., Aieta, F., Tetienne, J.-P., Capasso, F., and Gaburro, Z. (2011). Light propagation with phase discontinuities: Generalized laws of reflection and refraction. *Science*, 334(6054):333–337.

Zhang, K., Jung, Y. H., Mikael, S., Seo, J.-H., Kim, M., Mi, H., Zhou, H., Xia, Z., Zhou, W., Gong, S., and Ma, Z. (2017). Origami silicon optoelectronics for hemispherical electronic eye systems. *Nature Communications*, 8(1):1782.

Zhao, Y. and Alù, A. (2011). Manipulating light polarization with ultrathin plasmonic metasurfaces. *Physical Review B*, 84(20):205428.

# CURRICULUM VITAE